

AD-A207 332

DTIC FILE COPY

(2)

AFWAL-TR-83-2047

ADVANCED MOTOR AND MOTOR CONTROL DEVELOPMENT

Kenneth L. Wuertz  
Edward D. Beauchamp

ALLIED-SIGNAL AEROSPACE COMPANY  
AIRESEARCH LOS ANGELES DIVISION  
2525 W. 190TH STREET  
TORRANCE, CALIFORNIA 90509

August 1988

FINAL REPORT FOR PERIOD DECEMBER 1982 - DECEMBER 1987

Approved for public release; distribution unlimited

AEROPROPULSION LABORATORY  
AIR FORCE WRIGHT AERONAUTICAL LABORATORIES  
AIR FORCE SYSTEMS COMMAND  
WRIGHT-PATTERSON AIR FORCE BASE, OHIO 45433-6563



DTIC  
ELECTE  
APR 24 1989  
S H D

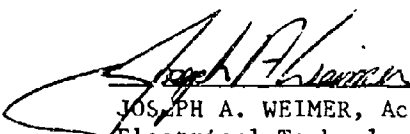
089 4 24 171

NOTICE

When Government drawings, specifications, or other data are used for any purpose other than in connection with a definitely Government-related procurement, the United States Government incurs no responsibility or any obligation whatsoever. The fact that the Government may have formulated or in any way supplied the said drawings, specifications, or other data, is not to be regarded by implication, or otherwise in any manner construed, as licensing the holder, or any other person or corporation; or as conveying any rights or permission to manufacture, use, or sell any patented invention that may in any way be related thereto.

This report has been reviewed by the Office of Public Affairs (ASD/PA) and is releasable to the National Technical Information Service (NTIS). At NTIS, it will be available to the general public, including foreign nations.

This technical report has been reviewed and is approved for publication.



JOSPH A. WEIMER, Acting TAM  
Electrical Technology Group  
Aerospace Power Division  
Aero Propulsion and Power Laboratory



Lowell D. MASSIE, Acting Chief  
Power Components Branch  
Aerospace Power Division  
Aero Propulsion and Power Laboratory

FOR THE COMMANDER



WILLIAM U. BORGER  
Chief, Aerospace Power Division  
Aero Propulsion & Power Laboratory

If your address has changed, if you wish to be removed from our mailing list, or if the addressee is no longer employed by your organization please notify AFWAL/POOC, Wright-Patterson AFB, OH 45433-6563 to help us maintain a current mailing list.

Copies of this report should not be returned unless return is required by security considerations, contractual obligations, or notice on a specific document.

Unclassified  
SECURITY CLASSIFICATION OF THIS PAGE

REPORT DOCUMENTATION PAGE					
1a. REPORT SECURITY CLASSIFICATION Unclassified			1b. RESTRICTIVE MARKINGS N/A		
2a. SECURITY CLASSIFICATION AUTHORITY N/A			3. DISTRIBUTION/AVAILABILITY OF REPORT Approved for Public Release: Distribution Unlimited		
2b. DECLASSIFICATION/DOWNGRADING SCHEDULE N/A			5. MONITORING ORGANIZATION REPORT NUMBER(S) AFWAL-TR-88-2047		
4. PERFORMING ORGANIZATION REPORT NUMBER(S) 88-61112			6a. NAME OF PERFORMING ORGANIZATION Allied-Signal Aerospace Company AiResearch Los Angeles Division		
6b. OFFICE SYMBOL (If applicable) AFWAL/POOC-1			7a. NAME OF MONITORING ORGANIZATION Aeropropulsion Laboratory (AFWAL/POOC) Air Force Wright Aeronautical Laboratories		
6c. ADDRESS (City, State, and Zip Code) 2525 W. 190th Street Torrance, California 90509			7b. ADDRESS (City, State, and ZIP Code) Wright-Patterson AFB, OH 45433-6563		
8a. NAME OF FUNDING/SPONSORING ORGANIZATION Aeropropulsion Laboratory			8b. OFFICE SYMBOL (If applicable) AFWAL/POOC-1		
9. PROCUREMENT INSTRUMENT IDENTIFICATION NUMBER F33615-82-C-2233			10. SOURCE OF FUNDING NUMBERS		
8c. ADDRESS (City, State, and ZIP Code) Air Force Wright Aeronautical Laboratories Wright-Patterson Air Force Base, OH 45433-6563			PROGRAM ELEMENT NO.	PROJECT NO.	TASK NO.
			62203F	3145	29
					70
11. TITLE (Include Security Classification) Advanced Motor and Motor Control Development					
12. PERSONAL AUTHORISI Kenneth L. Huertz, Edward D. Beauchamp					
13a. TYPE OF REPORT Final		13b. TIME COVERED FROM 12/82 TO 12/87		14. DATE OF REPORT (Year, Month, Day) 1988, August	15. PAGE COUNT 100
16. SUPPLEMENTARY NOTATION					
17. COSATI CODES			18. SUBJECT TERMS (Continue on reverse if necessary and identify by block number) Advanced Motor; Permanent Magnet; Brushless Motor Control; Electronic Fuel Pump		
FIELD	GROUP	SUB-GROUP			
09	05				
19. ABSTRACT (Continue on reverse if necessary and identify by block number) <p>The capability of operating a high-speed permanent-magnet brushless dc motor with electronic controller over a wide load and speed range was demonstrated. A centrifugal pump was used as the loading mechanism and hydraulic fluid was pumped in simulation of an aircraft engine fuel pump requirement. A motor speed of 45,000 rpm was reached and a maximum output of 68.5 hp was demonstrated. The response of the system to step commands for speed change was established. Reduction of size and weight of electronic control was established as primary future goal. Program system concept with minor rotating machine improvements is viable for high-speed drive applications up to 100-hp level.</p> <p>Joseph A. Weimer</p>					
20. DISTRIBUTION/AVAILABILITY OF ABSTRACT UNCLASSIFIED/UNLIMITED X SAME AS RPT. DTIC USERS			21. ABSTRACT SECURITY CLASSIFICATION Unclassified		
22a. NAME OF RESPONSIBLE INDIVIDUAL Joseph A. Weimer			22b. TELEPHONE (Include Area Code) (513)255-6235		22c. OFFICE SYMBOL AFWAL/POOC-1

## PREFACE

This final report was prepared by Allied-Signal Aerospace Company, AiResearch Los Angeles Division, for the Air Force Wright Aeronautical Laboratories, Wright-Patterson Air Force Base, under Contract F33615-82-C-2233. The technical effort was performed from December 1982 to December 1987 by the AiResearch electrical power systems product line group with Mr. Kenneth Wuertz as program manager. Mr. Joseph A. Weimer, the Air Force project engineer for the program, provided direction, technical support, and invaluable help and encouragement in guiding this program to a successful performance demonstration.

Many individuals made significant contributions to the organization and content of this report. It is difficult to single out specific people for special recognition; however, major contributions were made by Joseph Denk in motor design, Roy Brown in pump design, Edward Beauchamp and Colin Huggett in control design and development, Paul Gassen in laboratory engineering, and Al Thurman in hardware development and system test.

This program was an exploratory development effort to design, develop, and test a permanent-magnet brushless dc motor and associated motor control system for loads requiring precision speed control over a wide horsepower and speed range. The objective of the program was to develop the technology by demonstrating improved efficiency and performance in comparison with existing systems that may or may not use electric motor drives. The technology was demonstrated in an electric fuel pump concept, but is generally adaptable to many other applications requiring similar power and performance capability.



Accession For	
NTIS GRA&I	<input checked="" type="checkbox"/>
DTIC TAB	<input type="checkbox"/>
Unpublished	<input type="checkbox"/>
Justification	
By	
Distribution/	
Availability Codes	
Avail And/or	
Dist	Special
A-1	

## CONTENTS

<u>Section</u>	<u>Page</u>
1. SUMMARY	1-1
1.1 System Features	1-1
1.2 System Performance	1-1
2. INTRODUCTION	2-1
3. DESIGN	3-1
3.1 Motor Design	3-1
3.2 Pump Design	3-9
3.3 Motor Controller Design	3-15
3.3.1 Fundamental Requirements	3-15
3.3.1.1 Inverter-PMM Relationships	3-15
3.3.1.2 Inverter-PMM Control	3-18
3.3.2 Initial Design Considerations	3-18
3.3.2.1 Optimum Controller Topology	3-18
4. HARDWARE FABRICATION	4-1
4.1 Motor Assembly	4-1
4.2 Pump Hardware	4-1
4.3 Selected Motor Controller	4-5
4.3.1 Control Panel	4-14
4.3.2 Motor Controller Bench Testing	4-16
5. MOTOR TESTING	5-1
5.1 Motor Loss Breakdown	5-1
5.2 Motor Voltage and Inductance	5-2
6. SYSTEM TESTING	6-1
6.1 Test Concept	6-1
6.2 Test Results	6-7
7. CONCLUSIONS AND RECOMMENDATIONS	7-1
7.1 System	7-1
7.2 Motor Controller	7-2
7.2.1 Topology	7-2
7.2.2 Power Semiconductors	7-5
7.2.3 Improved Source/Controller/PMM System	7-5

## 1. SUMMARY

This final report presents the results of the design, development, and test of a brushless dc permanent-magnet motor (PMM) assembly and the associated motor controller. The program included the development of a centrifugal pump to load the motor and demonstrate feasibility of this type of system for fuel pump applications.

### 1.1 SYSTEM FEATURES

The motor incorporated state-of-the-art samarium-cobalt permanent magnets in a four-pole rotor. The magnets were supported and contained in an Inconel sleeve. Rotor cooling and bearing lubrication were achieved by passing a small quantity of the pumped fluid through the center of the shaft and pumping it into the bearing cavities.

The stator assembly was a conventional 3-phase design using a Class 220°C insulation system. Stator cooling was accomplished by bypassing a small quantity of the pump output through a heat exchanger in the stator housing.

The pump was a shrouded centrifugal design, using a brazed construction suitable for efficient operation at the high motor speeds.

The motor controller was designed to provide a startup capability from a 115/200-V, 400-Hz source, then transition to operation at the high-speed conditions from a 9-phase permanent-magnet generator providing a high-voltage, high-frequency power source. The motor controller was designed to phase-delay rectify from either source, thus providing a controlled dc link voltage. The dc link fed a 3-phase full-wave inverter, which powered the motor. Startup of the motor was accomplished by an increasing voltage and frequency ramp from the motor controller to the motor until a minimum speed was reached. Above that speed, the motor controller used the backvoltage to establish stator-to-rotor position logic. Hardware problems precluded final development and demonstration of this system. A substitute controller was used that incorporated the same 400-Hz and startup operation, but substituted a 3-phase, 480-V, 60-Hz source in place of the 9-phase generator.

The motor and pump assembly is shown in Figure 1-1, and the motor controller assembly is shown in Figure 1-2.

### 1.2 SYSTEM PERFORMANCE

The motor, pump, and motor controller were tested as a system to establish the overall performance and to permit the evaluation of each of the major components. Testing included steady-state operation at five different speed points with load valves set to restrict flow. In addition, three steady-state speed points were recorded with the load valves set to provide a "high flow" pump output. Testing was able to verify the system steady-state performance goals except for the high-power, high-flow point. The safe commutating margin for the motor controller was reached at approximately 81 percent of the peak power goal.

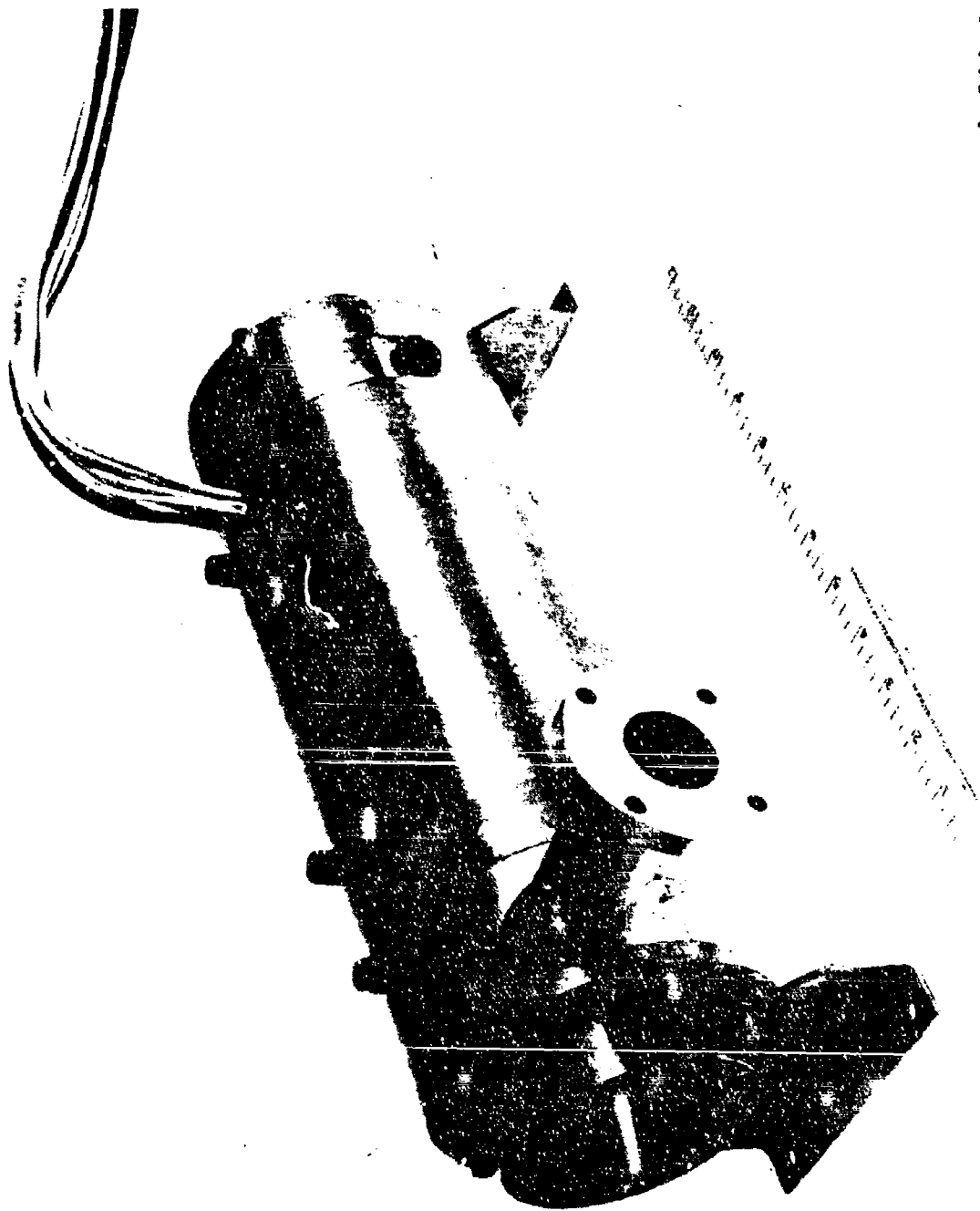
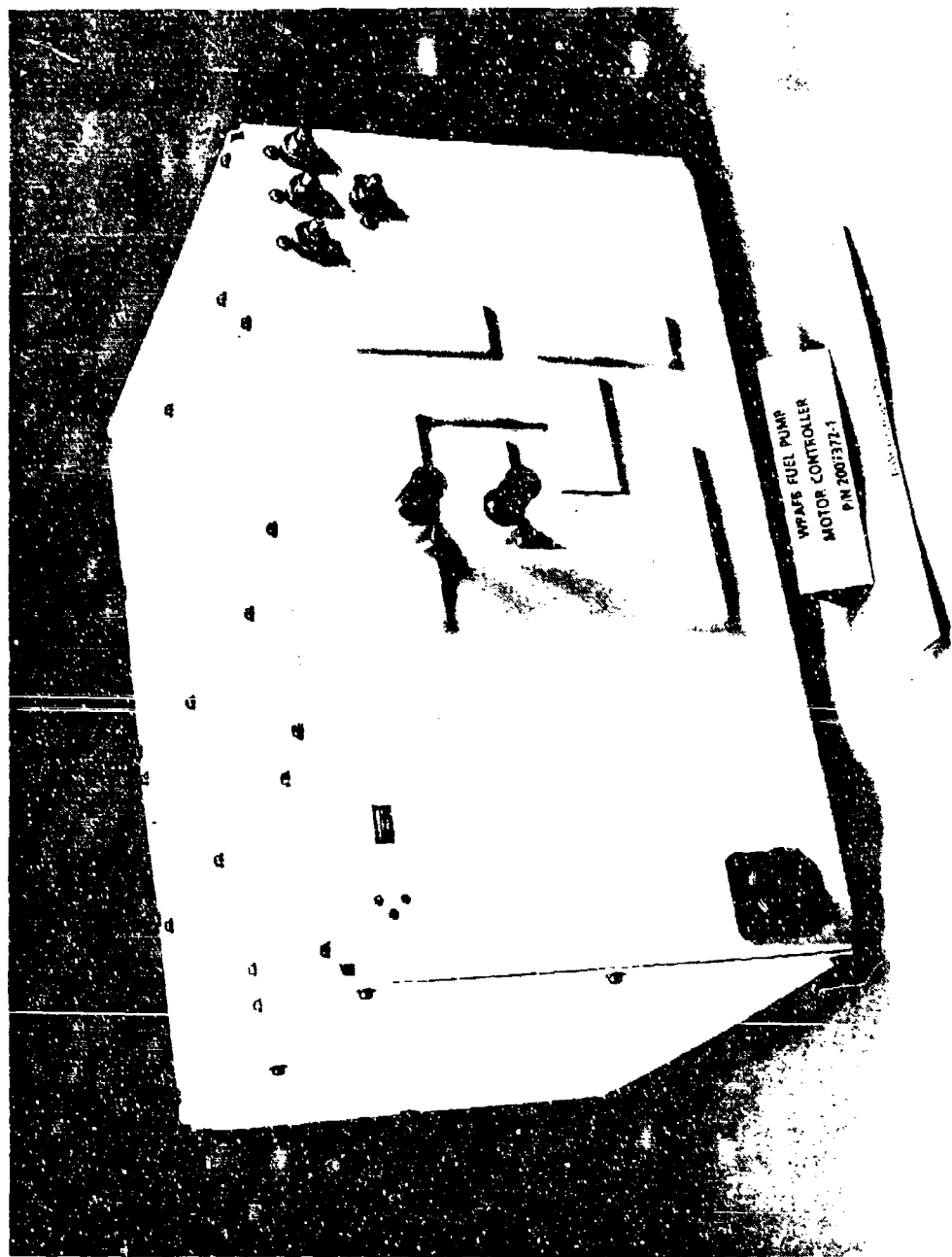


Figure 1-1. Motor and Pump Assembly

91790-2



95672-1

Figure 1-2. Motor Controller Assembly

The response of the system to step commands was determined. In the low-flow mode, three of the four step command goals were achieved, and the fourth was missed by approximately 0.25 second. The step command at 45,000 rpm from low-flow to high-flow mode could not be tested due to flow control valve problems.

Table 1-1 summarizes the system test performance.

TABLE 1-1. System Test Result Summary

Test	Goal	Result	Comment
Low-flow performance	10 to 45 krpm 0.2 to 45 hp 1 to 35 gpm 2 to 25% eff Continuous duty	10 to 45 krpm 11 to 62 hp 10 to 57 gpm 14 to 37% eff Continuous duty to 45 hp	Higher output at speeds achieved due to use of MIL-H-83282 in place of MIL-C-7024
High-flow performance	45 krpm 85 hp 145 gpm 54% eff. 1 min. duty	37.1 krpm 68.5 hp 128 gpm 47% eff. 1 min. duty	System power limit reached due to limit on command margin
Step command response	15 to 24 krpm 2.5 4 to 10 hp sec	14 to 24 krpm 1.4 4 to 13 hp sec	Step commands vary slightly from goal due to use of substitute controller. Considerable margin on all but one point where hydraulic braking load was insufficient
	24 to 15 krpm 1.5 10 to 4 hp sec	24 to 14 krpm 1.75 13 to 4 hp sec	
	24 to 45 krpm 5.5 10 to 45 hp sec	24 to 40 krpm 2.4 13 to 46 hp sec	
	45 to 24 krpm 3.5 45 to 10 hp sec	40 to 24 krpm 2.1 46 to 13 hp sec	
	45 krpm 45 to 85 hp 85 to 40 hp	unable to test	Test valve problem precluded testing to high-flow valve setting

## 2. INTRODUCTION

This report documents the design, development, and test of an electronically controlled, permanent-magnet, brushless dc motor and pump.

The selected design concept centered on a high-energy samarium-cobalt permanent-magnet motor using pump fluid for rotor and stator cooling. The motor controller uses half-wave phase-delay rectification on each of two alternate power inputs and a 3-phase full-wave thyristor inverter. A centrifugal pump was designed to provide shaft loading and hydraulic output consistent with specification goals.

The system performance goals were to demonstrate stable, precise operation over a motor shaft power range of 1 to 85 hp with a concurrent speed range of 10,000 to 45,000 rpm. The following specific power and speed points were selected to demonstrate performance at typical engine operating conditions:

- (a) Ground start
- (b) Ground idle
- (c) Cruise
- (d) Maximum dry
- (e) Maximum afterburner

The specification also required certain motor and motor controller instrumentation and control features. These include protection against thermal and electrical overloads, a power source select switch, and a motor shaft speed directly proportional to an analog dc-voltage speed command signal.

The major technical challenges addressed in the program are listed below for the motor, motor controller, and pump.

### Motor

Optimizing the electromagnetic design consistent with thermal, stress, and critical speed constraints

Selecting the suitable startup operational mode

Sealing motor cavities against high pump outlet pressure

Minimizing weight and package size

Providing maximum efficiency

Accurately determining motor losses to permit component evaluation during system testing

Motor Controller

Minimizing weight and size in the dual converter with the capability of operating from two input sources

Providing maximum efficiency

Selecting power semiconductors to provide the best commutation match for the motor current

Pump

Designing for best efficiency over a wide operating range

Ensuring that the design is consistent with shaft dynamics, bearing lubrication, and motor cooling

The following sections of this report describe the activities in each of the major phases of the program. These are (1) design analysis and optimization, (2) hardware fabrication, (3) component level testing, and (4) system testing.

### 3. DESIGN

The overall design of the motor, pump, and motor controller changed early in the program from that defined in the proposal. A number of these changes were implemented to simplify the system and reduce weight, while others were directed toward improving system performance. In addition, Mr. George Coffinberry of General Electric provided insight into the potential use of this type of system on engines. This resulted in a change to the pump design approach. Mr. Coffinberry also recommended a change to a higher power system. This would have required an increase from 85 to 99 hp and an operating speed of 52,000 rpm instead of 45,000 rpm. The higher power approach was not used because of the significant impact it would have had on the program scope and cost.

#### 3.1 MOTOR DESIGN

The motor design changed from the proposed unit because the motor controller optimization favored a change from the voltage-source, transistor-inverter drive to a current-source, thyristor-inverter approach. The motor required only a winding change to provide the lower backvoltage needed for the current source thyristor-inverter approach.

The motor electromagnetic design was performed on the AiResearch permanent-magnet machine computer design program, BIGMAG. This program has the capability of optimizing a design based on selected key parameters. The primary goals in this design were to achieve a maximum efficiency while maintaining a competitive motor weight. Table 3-1 presents the most significant motor dimensional and performance parameters.

TABLE 3-1. Calculated Motor Design

Parameter	Value
Dimensions	
Stack OD	4.266 in.
Stack ID	2.457 in.
Stack length	6.058 in.
Rotor OD	2.421 in.
Coil extension	1.148 in.
Magnets	
Material	Samarium Cobalt (Sm <sub>2</sub> Co <sub>17</sub> )
Energy product	27 MGoe
Weight	
Motor, electromagnetic	17.36 lb
Magnets	2.018 lb

TABLE 3-1 (Continued)

Parameter	Value
Flux Densities	
Stator core	50 k1/sq in.
Stator teeth	105.3 k1/sq in.
Air gap	30.5 k1/sq in.
Magnet	39.8 k1/sq in.
Rotor core	90 k1/sq in.
Losses at 85 hp, 45,000 rpm	
Stator core	571 W
Stator teeth	479 W
Copper I <sup>2</sup> R (350°F)	1201 W
Rotor	170 W
Losses at 45 hp, 45,000 rpm	
Stator core	664 W
Stator teeth	557 W
Copper I <sup>2</sup> R (350°F)	387 W
Rotor	114 W
Efficiency (electromagnetic)	
85 hp at 45,000 rpm	96.32*
45 hp at 45,000 rpm	95.12*
Winding Data	
Turns per coil	5
Wire	20 strands, 26 AWG
Parallel circuits	4
Span	5/6
Resistance (20°C)	0.0085 ohm/phase
Interface Data	
Commutating inductance	24 $\mu$ h/phase
Induced volts per phase (at 45,000 rpm, 85 hp)	157 V/phase
Fundamental rms current (at 45,000 rpm, 85 hp)	173 amp/phase

\*Electromagnetic efficiencies do not include windage and friction or harmonic and stray losses.

The losses were calculated and a thermal analysis for the motor was performed. The analysis indicated that a coolant flow of 3 gpm is required in both the stator cooling heat exchanger and the rotor-shaft-bearing cooling circuit. The stator is cooled by passing the coolant from a pump output tap through channels machined in the stator housing. The rotor is cooled by directing a small quantity of pump inlet oil down a hole in the rotor shaft, then pumping oil into each bearing cavity. The worst-case temperatures predicted, using 200°F coolant, are a 342°F winding and a 292°F magnet temperature after continuous operation at 45 hp and 45,000 rpm. If the maximum afterburner load was applied for 1 minute with the motor initially at these steady-state maximum temperatures, the stator assembly hot spot would rise to 453°F and the magnet temperature would reach 300°F. These temperatures are well within the short term operating limits of the insulation system and the magnets. Figure 3-1 presents the thermal model network, and Figure 3-2 shows the temperatures at the 45-hp load. Figure 3-3 gives the maximum temperatures reached after the 85-hp load is applied for 1 minute.

Motor rotor stress and shaft dynamic analyses were conducted. The rotor assembly design was evaluated to ensure that no lifting of the sleeve occurred due to centrifugal and thermal loads, and that the interference fits were specified. The worst-case stress condition was calculated in the rotor sleeve to be 106 ksi at 45,000 rpm. This provided a safety margin of 0.42 with respect to the yield strength of Inconel 718 sleeve material. Calculation results were obtained from finite element analysis of the model representing 1/8 of the rotor cross section, as shown on Figure 3-4.

Rotor dynamic analysis using ball bearings was also performed. The rotating machine was modeled using a 772 lb/in. magnetic spring rate and 600,000 lb/in. ball bearing spring rate. The following critical speed results were obtained:

- (a) First critical speed (cylindrical mode with moderate bending) is 58,480 rpm.
- (b) Second critical speed is 122,708 rpm

The use of resilient bearing mounts was investigated in case it proved necessary to increase the first critical speed. Utilizing resilient mounts will bring the first two rigid-body-mode critical speeds down and at the same time will increase the bending critical speed. In order to achieve the desired critical speeds, each resilient mount was designed to have stiffness equal to 3500 lb/in. This would cause the two rigid body modes to occur at  $N_1 = 5132.4$  rpm and  $N_2 = 8869.1$  rpm, which is below 10,000 rpm. At the same time, bending mode would occur at the speed of  $N_3 = 124,951$  rpm, which would provide 1.78 margin of safety with respect to the operating speed of 45,000 rpm.

Assuming 3-percent damping with respect to the first critical speed for each resilient mount, and considering 0.2 gr-in. total unbalanced mass divided equally between stations 7 and 13 (see Figure 3-5 for all station locations),

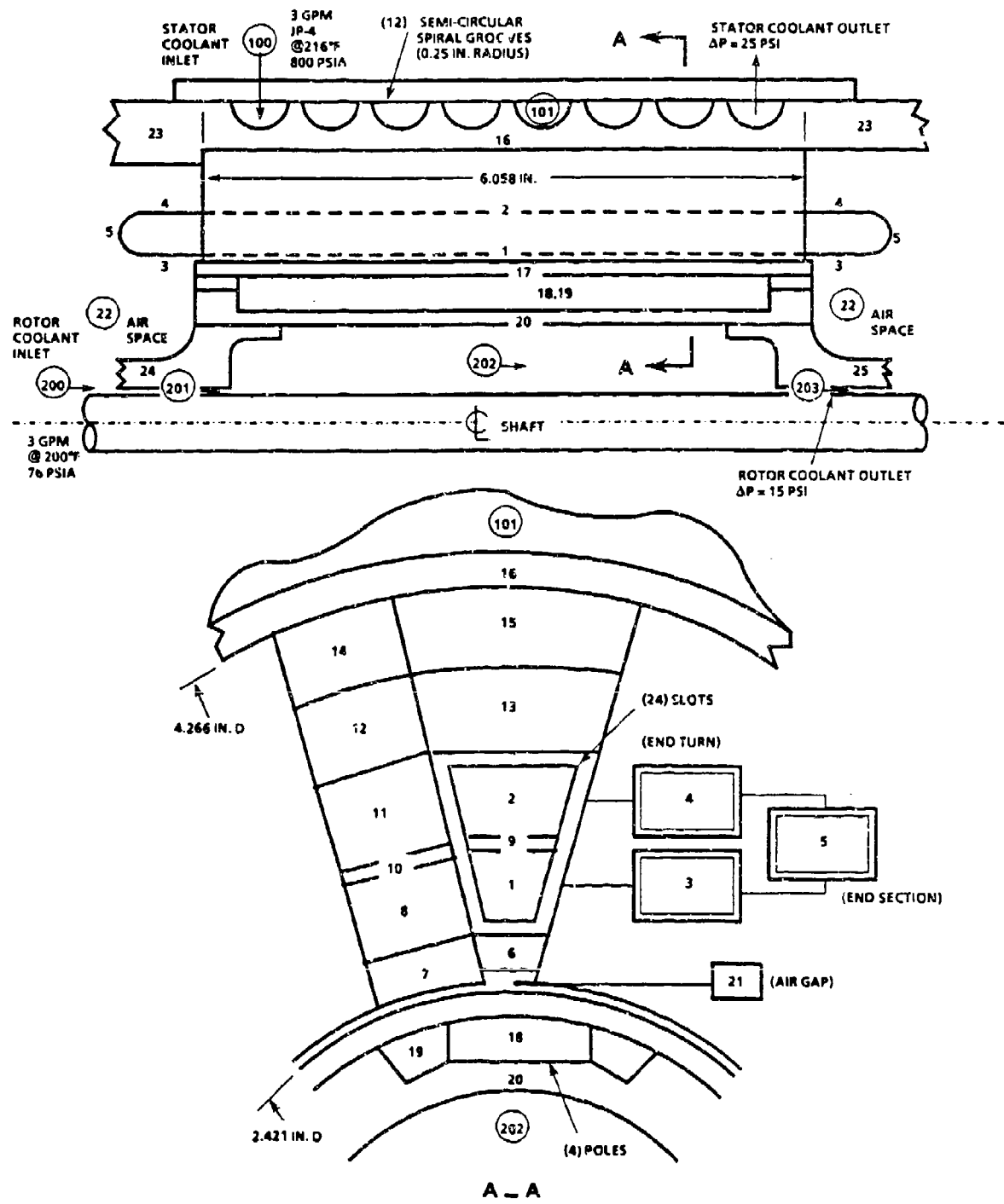


Figure 3-1. Thermal Model Network WPAFB Fuel Pump Motor

WPAFB 85-HP FUEL PUMP MOTOR REDESIGNED 7-19-83  
 STEADY STATE TEMPERATURE DISTRIBUTION  
 NO. OF ITER.= 3 DTEMP= .1333 DEG.F ACCEL. FACTOR= 1.0000

NODE NO.	TEMPERATURE (DEG.F)	TEMPERATURE (DEG.C)	HEAT IN (WATTS/F)	WEIGHT (LBS)	SP. HEAT (B/LB-FT)	CONDUCTIVITY (B/MR-FT-F)
1	327.88	164.37	122.942	.924	.100	200.000
2	303.53	150.89	118.779	.924	.100	200.000
3	302.15	172.29	52.619	.388	.100	200.000
4	333.88	167.70	52.021	.388	.100	200.000
5	339.86	171.02	26.817	.198	.100	200.000
6	318.31	159.05	.000	.000	.220	.120
7	309.55	154.18	.000	.517	.120	11.875
8	308.06	153.35	278.500	.834	.120	11.875
9	314.48	156.92	.000	.000	.220	.120
10	298.67	148.13	.000	.040	.120	11.875
11	290.69	143.71	278.500	.700	.120	11.875
12	255.94	124.40	76.728	1.077	.120	11.875
13	252.99	122.73	255.771	3.622	.120	11.875
14	239.31	115.16	67.530	1.077	.120	11.875
15	230.91	114.94	264.970	4.226	.120	11.875
16	230.33	110.17	.000	2.429	.210	100.000
17	295.56	146.42	.000	1.055	.110	0.000
18	291.71	144.27	95.000	2.136	.120	4.450
19	290.92	143.83	19.000	.159	.210	100.000
20	282.01	138.86	.000	1.353	.110	24.000
21	315.74	157.62	195.130	.000	.240	.016
22	290.21	143.44	.000	.000	.240	.016
23	233.24	111.79	.000	1.667	.210	100.000
24	203.18	95.09	.000	.408	.110	24.000
25	204.62	95.89	.000	.408	.110	24.000

TOTAL WEIGHT OF THERMAL MODEL ELEMENTS= 29.469 LBS.

FLUID CAPACITY RATE ELEMENTS

STREAM NO.= 1		NODE NO.= 100		INLET TEMP.= 216.00 F ( 102.21 C)		
SECTION NO.	NODE NO.	OUTLET TEMP. (DEG.F)	OUTLET TEMP. (DEG.C)	FLOW RATE (LBS/SEC)	DENSITY (LBS/FT <sup>3</sup> )	HEAT IN (WATTS)
1	101	225.41	107.44	.30000	45.846	.000

STREAM NO.= 2		NODE NO.= 200		INLET TEMP.= 200.00 F ( 93.32 C)		
SECTION NO.	NODE NO.	OUTLET TEMP. (DEG.F)	OUTLET TEMP. (DEG.C)	FLOW RATE (LBS/SEC)	DENSITY (LBS/FT <sup>3</sup> )	HEAT IN (WATTS)
1	201	200.07	93.36	.30000	46.344	.000

STREAM NO.= 3 NODE NO.= 201 INLET TEMP.= 200.07 F ( 93.36 C)

Figure 3-2. Motor Thermal Analysis at 45,000 rpm and 45 hp

4PAFB 85-HP FUEL PUMP MOTOR REDESIGNED 7-19-83

TRANSIENT STATE TEMPERATURE DISTRIBUTION  
TIME= 60.000 SEC DTHTET= .05056 SEC (CONTROLLED BY NODE 101)

NODE NO.	TEMPERATURE (DEG.F)	TEMPERATURE (DEG.C)	HEAT IN (WATTS)	WEIGHT (LBS)	SP. HEAT (B/LB-F)	HEAT CONDUCTIVITY (B/HR-FT-F)
1	399.74	204.29	419.977	.924	.100	200.000
2	363.02	184.33	400.698	.924	.100	200.000
3	453.06	233.91	185.120	.388	.100	200.000
4	440.04	226.68	185.204	.388	.100	200.000
5	451.90	233.27	96.139	.198	.100	200.000
6	359.39	181.87	.000	.000	.220	.120
7	331.70	163.49	.000	.517	.120	11.875
8	331.29	166.26	239.500	.834	.120	11.875
9	379.26	192.91	.000	.000	.220	.120
10	318.92	159.39	.000	.040	.120	11.875
11	308.35	153.52	239.500	.700	.120	11.875
12	262.68	128.14	65.880	1.077	.120	11.875
13	258.91	126.05	219.620	3.622	.120	11.875
14	242.09	116.70	57.980	1.077	.120	11.875
15	281.62	116.43	227.520	4.226	.120	11.875
16	231.97	111.08	.000	2.429	.210	200.000
17	304.98	151.64	.060	1.055	.110	8.000
18	299.82	148.78	191.700	2.136	.120	4.850
19	299.36	148.52	26.300	.159	.210	100.000
20	288.66	142.58	.000	1.353	.110	24.000
21	332.53	166.95	192.827	.000	.240	.016
22	349.62	176.44	.000	.000	.240	.016
23	236.39	113.54	.000	1.607	.210	100.000
24	203.37	95.19	.000	.408	.110	24.000
25	204.90	96.05	.000	.408	.110	24.000

TOTAL WEIGHT OF THERMAL MODEL ELEMENTS= 24.969 LBS.

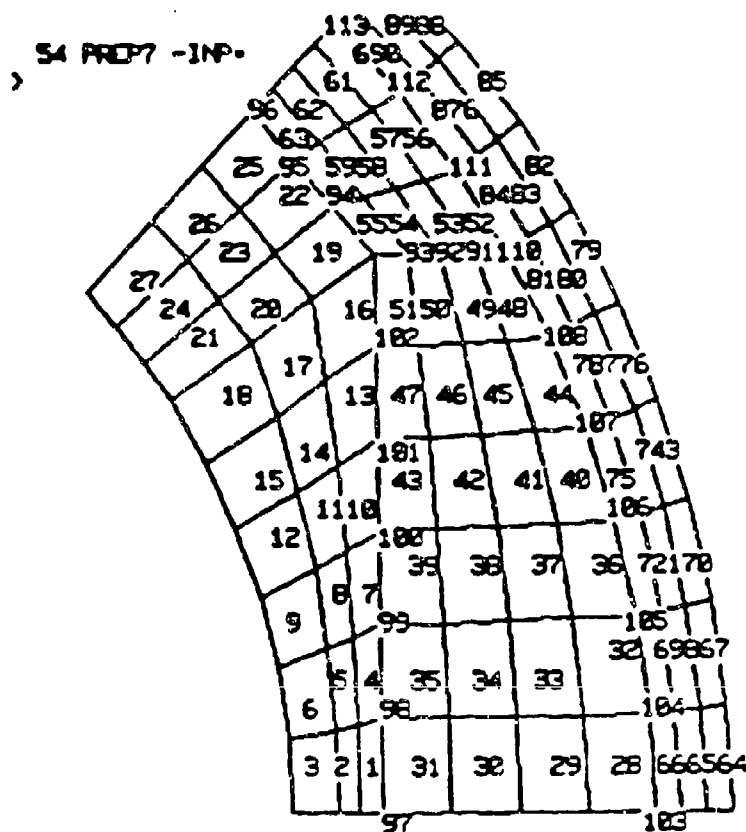
FLUID CAPACITY RATE ELEMENTS

STREAM NO.= 1 NODE NO.= 100 INLET TEMP.= 216.00 F ( 102.21 C)					
SECTION NO.	NODE NO.	OUTLET TEMP. (DEG.F)	FLOW RATE (LBS/SEC)	DENSITY (LBS/FT <sup>3</sup> )	HEAT IN (WATTS)
1	101	226.49	100.04	.30000	45.432 .000

STREAM NO.= 2 NODE NO.= 200 INLET TEMP.= 200.00 F ( 93.32 C)					
SECTION NO.	NODE NO.	OUTLET TEMP. (DEG.F)	FLOW RATE (LBS/SEC)	DENSITY (LBS/FT <sup>3</sup> )	HEAT IN (WATTS)
1	201	200.07	93.36	.30000	46.344 .000

STREAM NO.= 3 NODE NO.= 201 INLET TEMP.= 200.07 F ( 93.36 C)

Figure 3-3. Motor Thermal Analysis at 45,000 rpm and 85 hp for 1 min



4/21 03:19  
Z-X

ZV=1  
DLM=1

EP ANSYS 12 S

ESS ANALYSIS FOR FUEL PUMP DRIVE MOTOR ROTOR

PRODUCE ELEMENT PLOT TERMINAL BAUD=1200 PLOTTER TYPE= 0  
21 PREP7 -INP.

>

PLOT ELEMENT TYPES= 1  
22 PREP7 -INP.

>

PRODUCE ELEMENT PLOT

Figure 3-4. Finite Element Analysis of 1/8 Rotor Segment

C.G. OF SHAFT OF ROTOR..... = 6.2075+000  
 TOTAL MASS..... = 2.0979-002  
 TOTAL I<sub>P</sub>..... = 1.5112-002  
 TOTAL I<sub>D(C6)</sub>..... = 1.6883-001  
 I<sub>D(C6)/IP</sub>..... = 1.1172+001

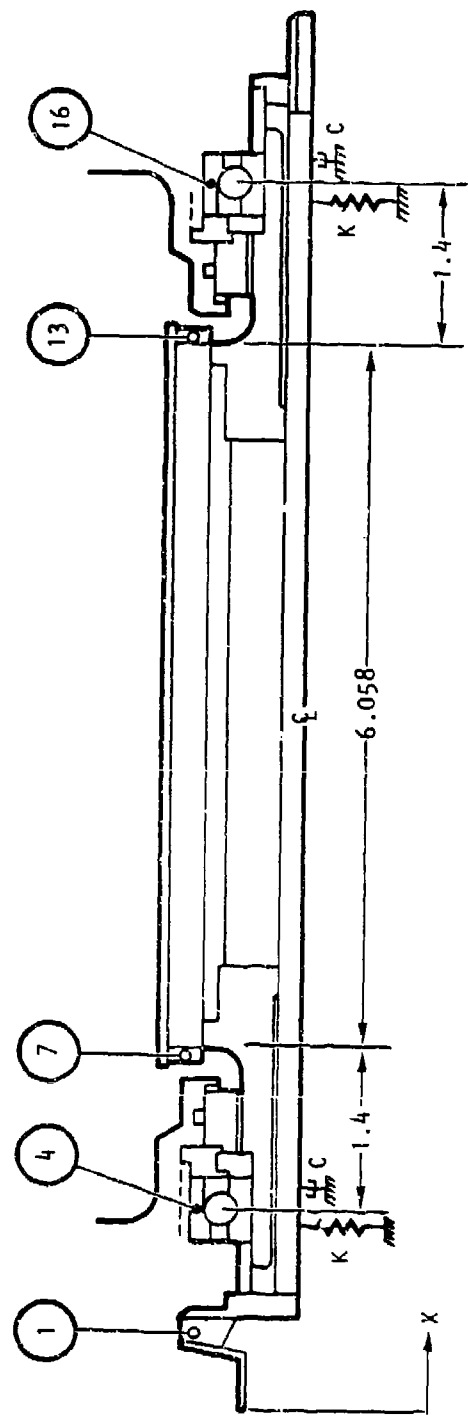


Figure 3-5. Rotor Assembly with Analysis Stations Identified

the maximum amplitude at either (or both) rigid body modes for the following two cases was obtained as follows:

Case 1--Unbalance Masses in Phase

Amplitude = 0.0009 in. At station 1 and at first critical speed

Case 2--Unbalanced Masses Out of Phase

Amplitude = 0.00125 in. At station 1 and at second critical speed

Mode shapes and displacement curves as a function of frequency for station 1 for zero damping were calculated. Displacement vs frequency for stations 1, 4, 7, and 16 was also determined for Cases 1 and 2.

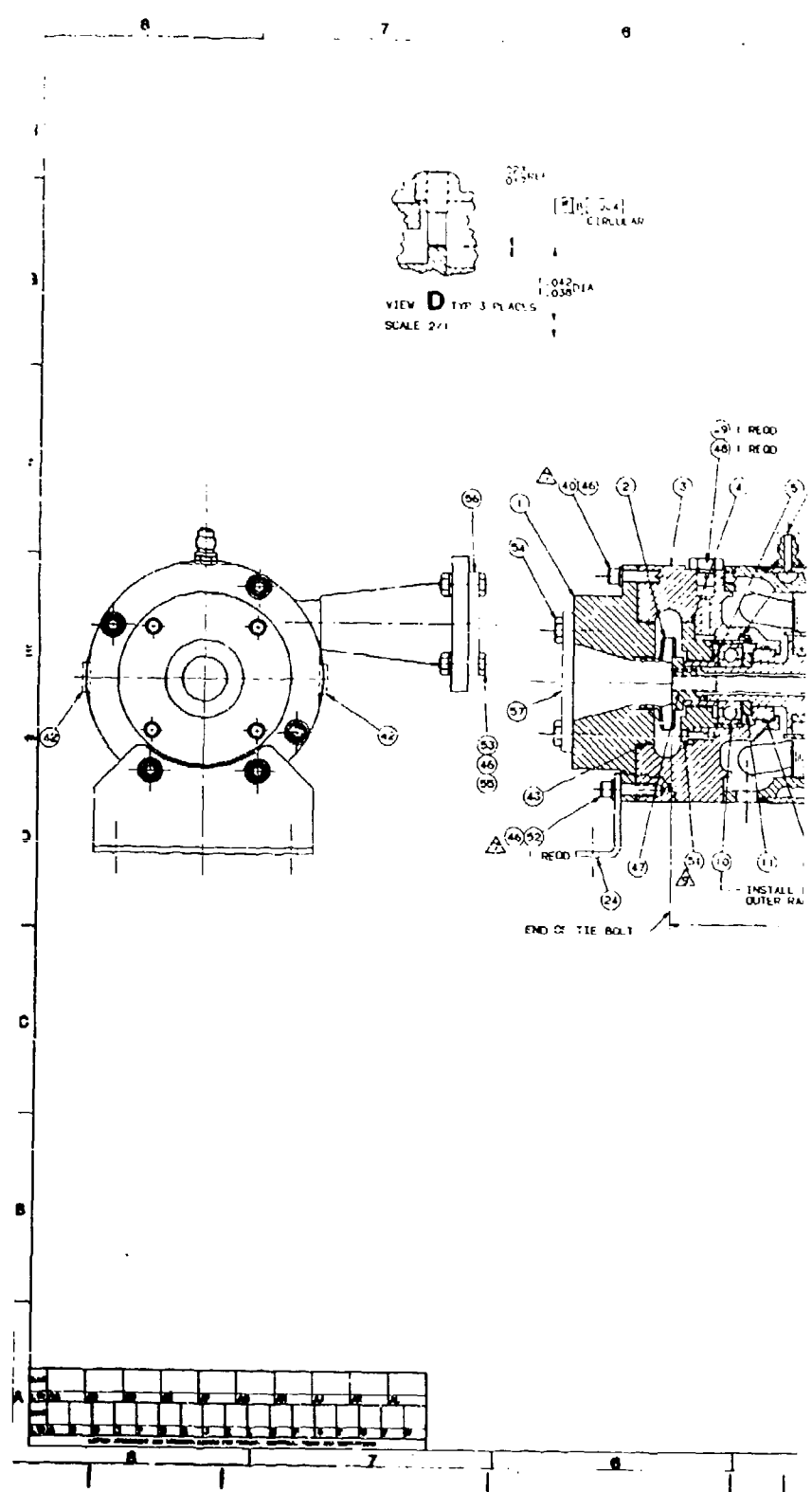
The motor-pump assembly drawing (Figure 3-6) displays the location of the cooling circuits, bearings, seals, and pump impeller. The rotating assembly details are clamped with a stressed tie bolt through the center of the shaft. The bearing cavities are designed to provide an axial thrust balance due to hydraulic pressure in the cavities. This prevents relief of the bearing preload at any operation condition.

The stator assembly and rotor assembly are shown in Figures 3-7 and 3-8, respectively.

### 3.2 PUMP DESIGN

The program kickoff meeting was held in February 1983. Mr. George Coffinberry of General Electric recommended that the F101 engine not be used as a model for the application goals, but that an advanced engine be considered. The main impact of this on the pump design was to change from the proposed approach, which used two impellers, one at each end of the shaft, to a single impeller. The two-impeller approach used the second impeller only to support the high-flow full afterburner condition. The two-impeller design was proposed originally because the F101 engine required a different pressure for the afterburner operating condition. AiResearch calculated the pump loads and efficiencies with the single impeller approach. These values are given in Table 3-2. This concept was agreed on and the pump hydraulic design proceeded. The analysis indicated the inherent advantages of the single impeller concept: less development time and cost risk, and higher efficiency. The program pump efficiency goals at the low load levels were not achievable in any case.

The impeller assembly is shown in Figure 3-9. It includes labyrinth seals to keep the high-pressure pump outlet from feeding back into the inlet and to keep leakage out of the front bearing cavity. Due to the small clearances necessary in the labyrinth seals, the decision was made to use the non-resilient mount design approach for the bearings. This provides less critical speed margin but assures seal clearance. Testing of the rotating motor-pump assembly at a speed of 50,000 rpm was done to verify the suitability of this approach. No significant vibration or dynamic loads were detected and the resilient mounts were not used in the test program.



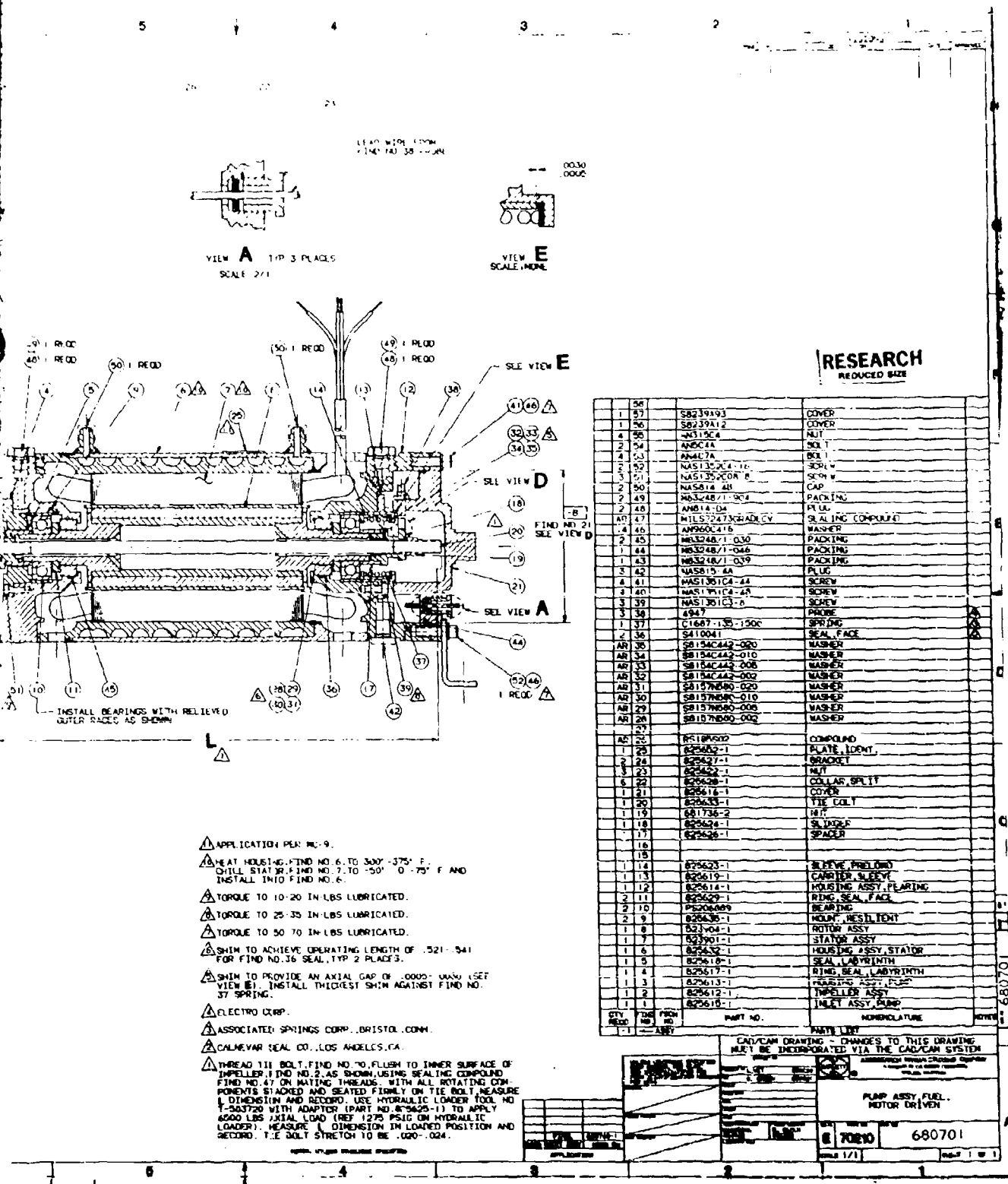
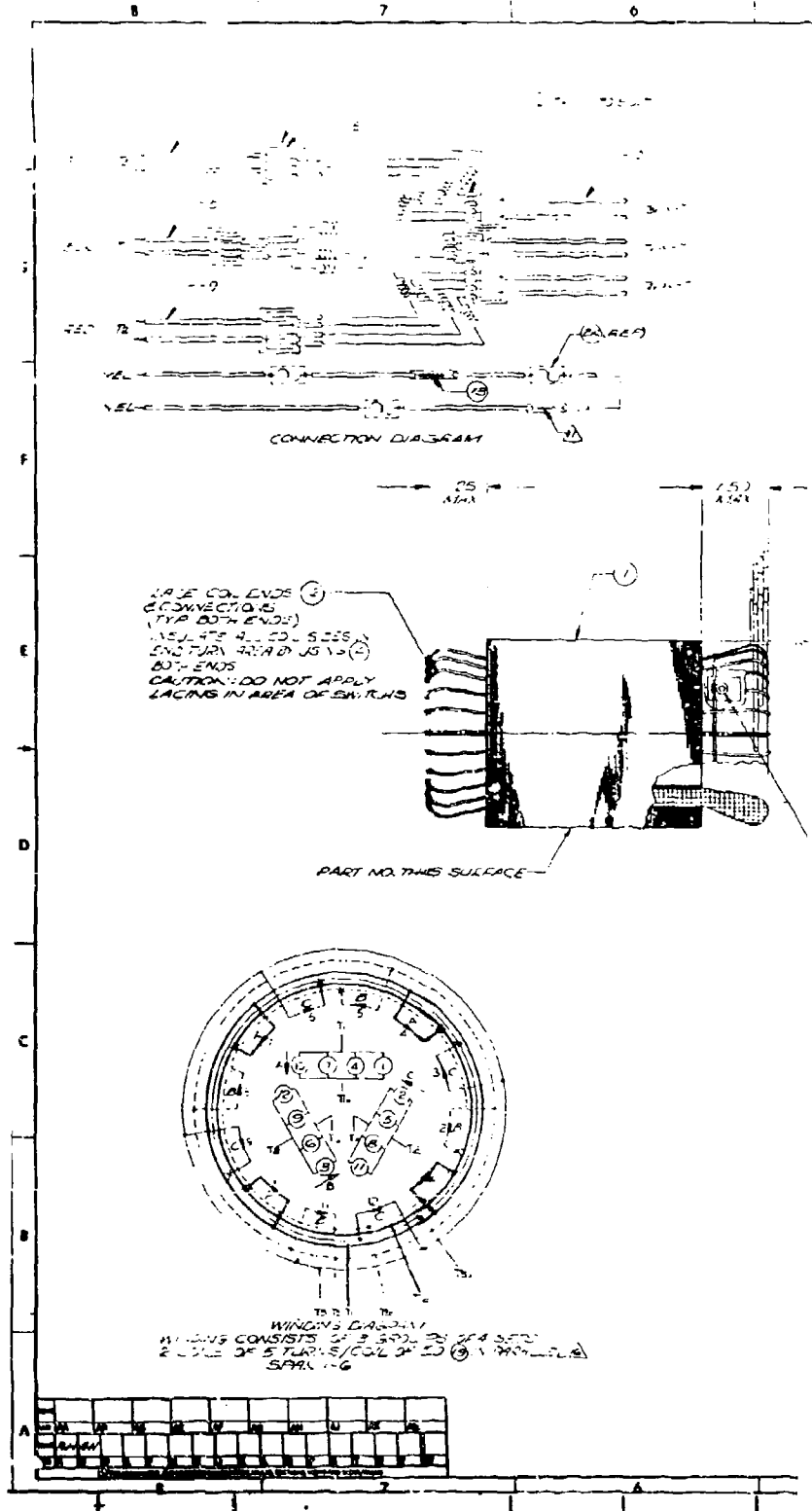
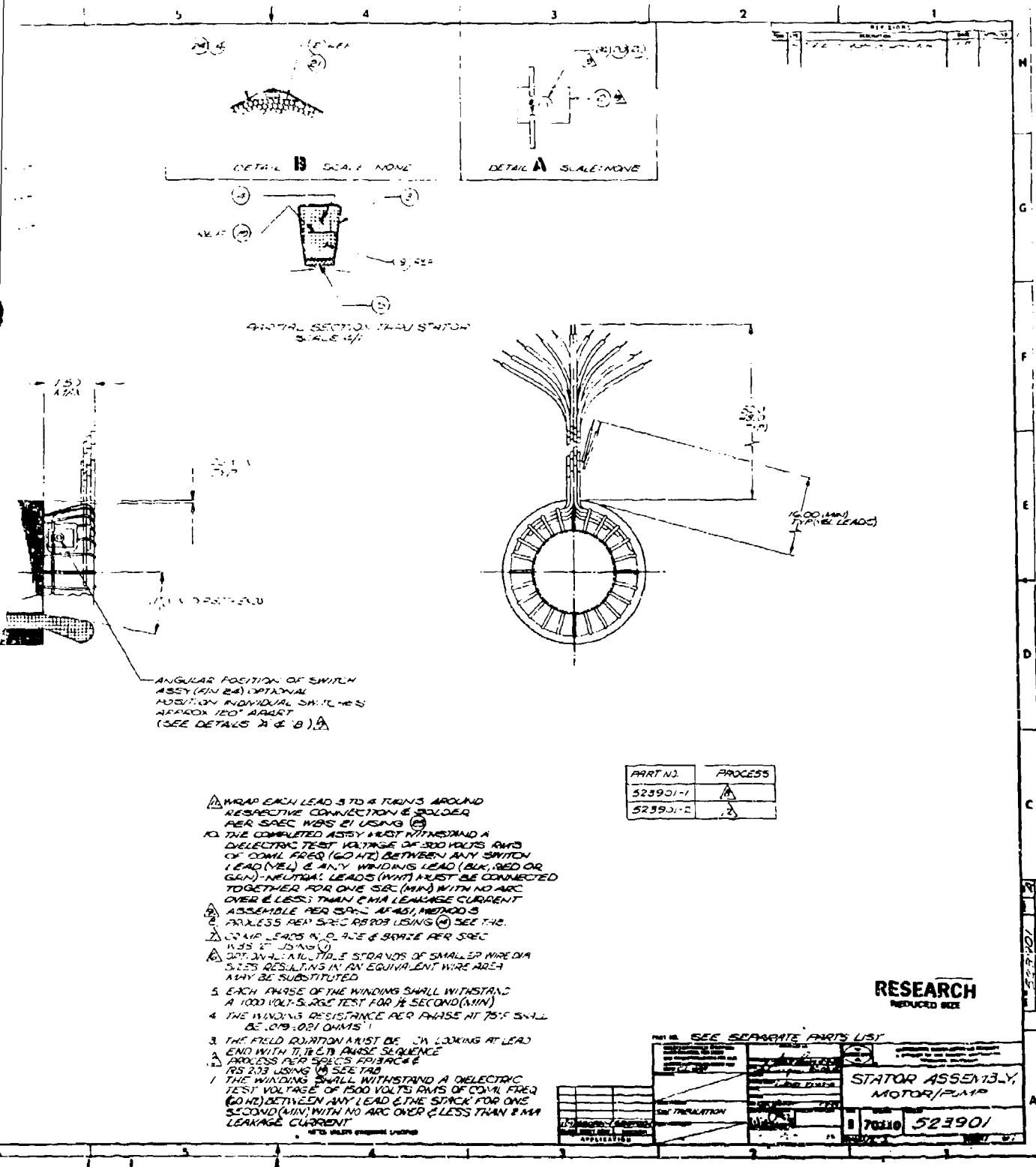
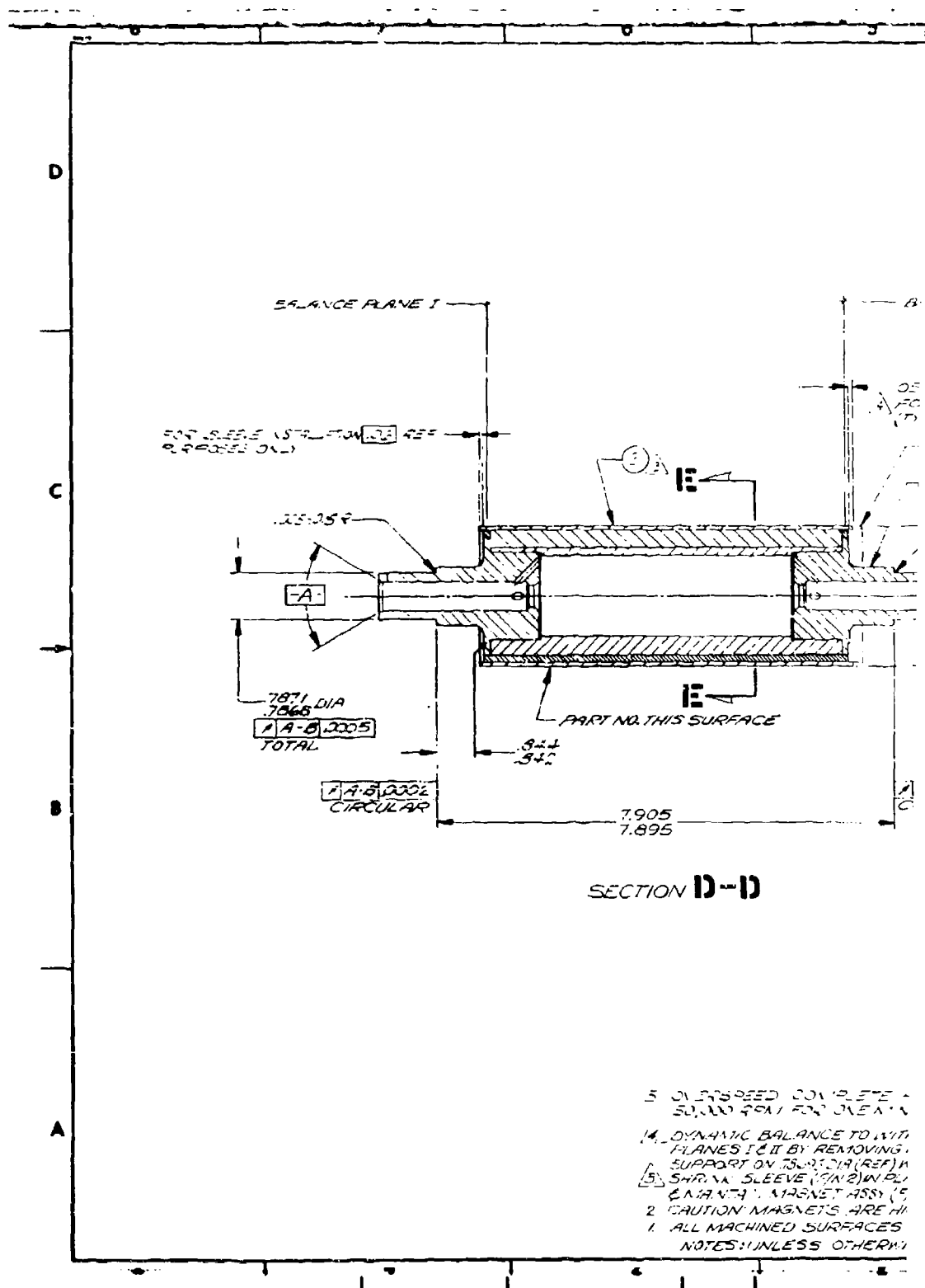


Figure 3-6. Motor and Pump Assembly



Figure 3-7. Stator Assembly



5. OVERSPEED COMPLETE -  
SU AND FOR AREA 1  
14. DYNAMIC BALANCE TO WITH  
PLANES 1&2 BY REMOVING  
SUPPORT ON BLADE 2 (REF 14)  
15. SHRIVA SLEEVE (5"2) IN PLI  
CAHNTA. MAGNET ASSY (5)  
2. CAUTION MAGNETS ARE HI  
1. ALL MACHINED SURFACES  
NOTES!!UNLESS OTHERWISE

83-61112

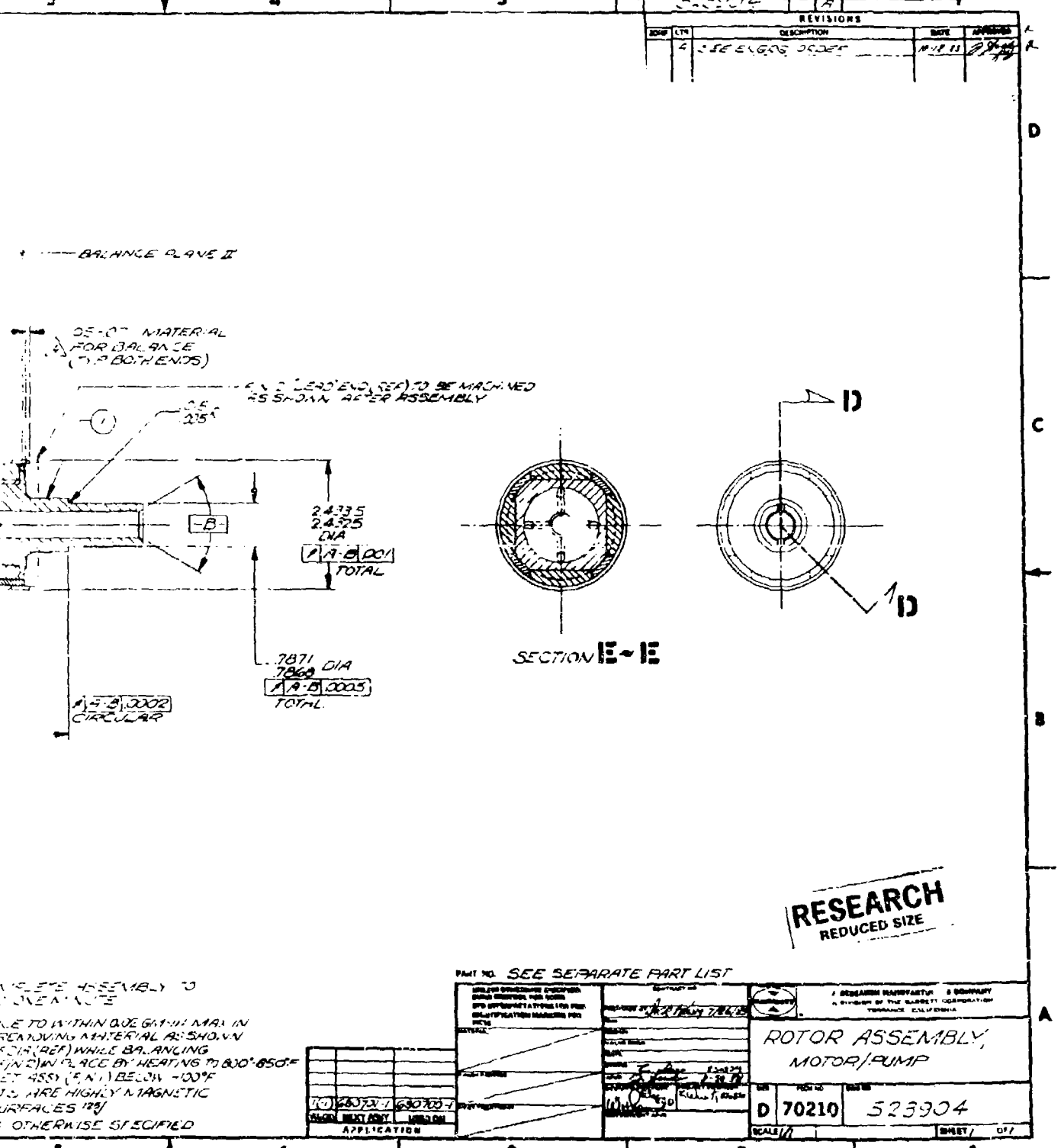
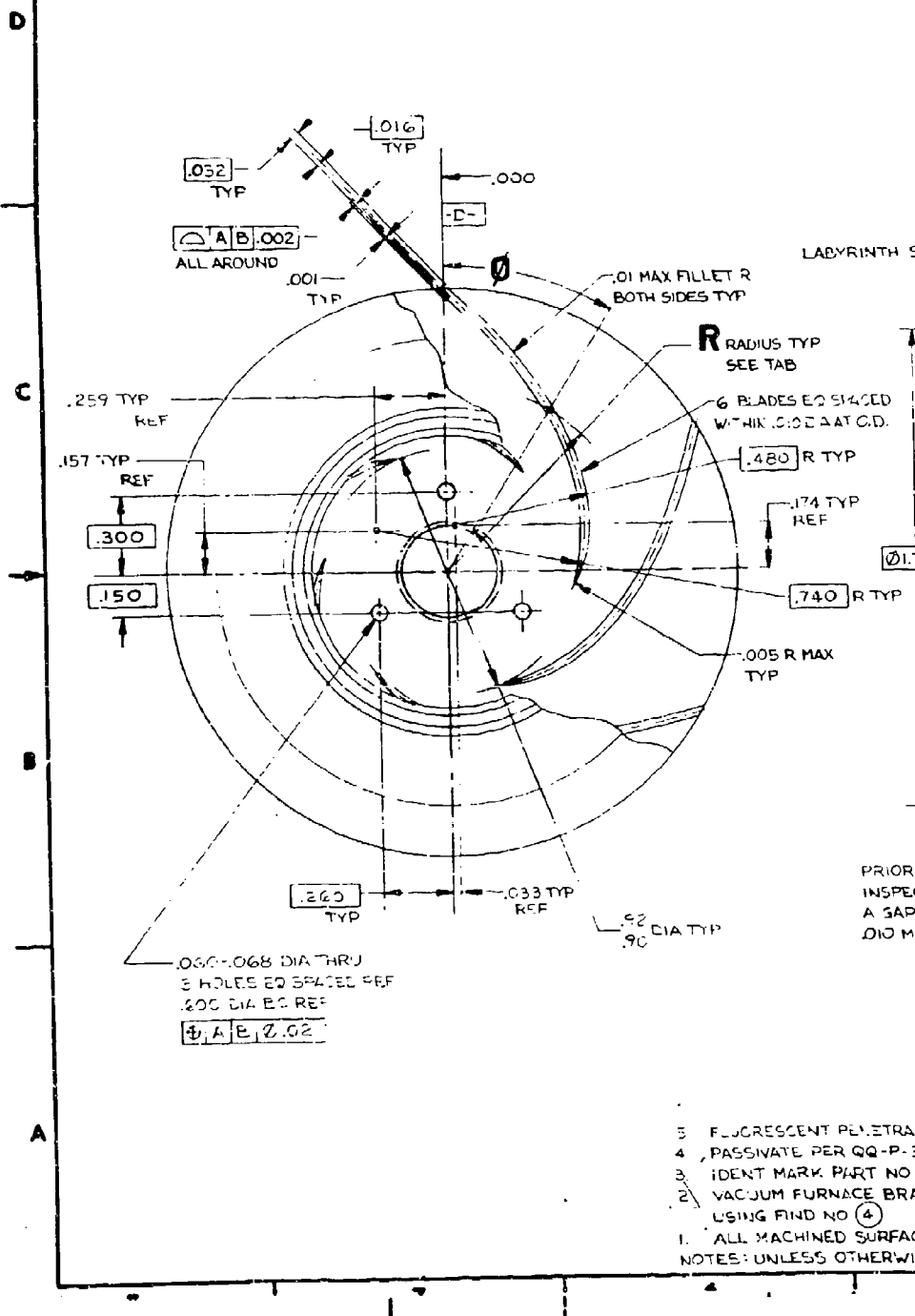


Figure 3-8. Rotor Assembly

TABLE 3-2. Single Impeller WPAFB Pump Operating Conditions (1.93 Impeller Diameter)

Point	Condition	Engine Speed, percent	Pump Flow, gpm	Pump ΔP, psi	Speed, rpm	Motor HP	Operating Time	Efficiency, percent
1	Maximum A/B	101.8	145	725	45,000	85.0	1 min	72
2	Maximum dry	101.8	35	815	45,000	45.0	Continuous	37
3	Cruise	89.2	8	232	24,000	10.0	Continuous	11
4	Ground idle	62	3	91	15,000	4.0	Continuous	4
5	Ground start	10	1	40	10,000	2.0	Continuous	1.3

0 ANGLE IN DEGREES	0	15	30	45	60	75	90	105	120	135	150
R RADIUS	1.00	1.07	1.05	1.00	0.95	0.87	0.71	0.57	0.43	0.31	0.23



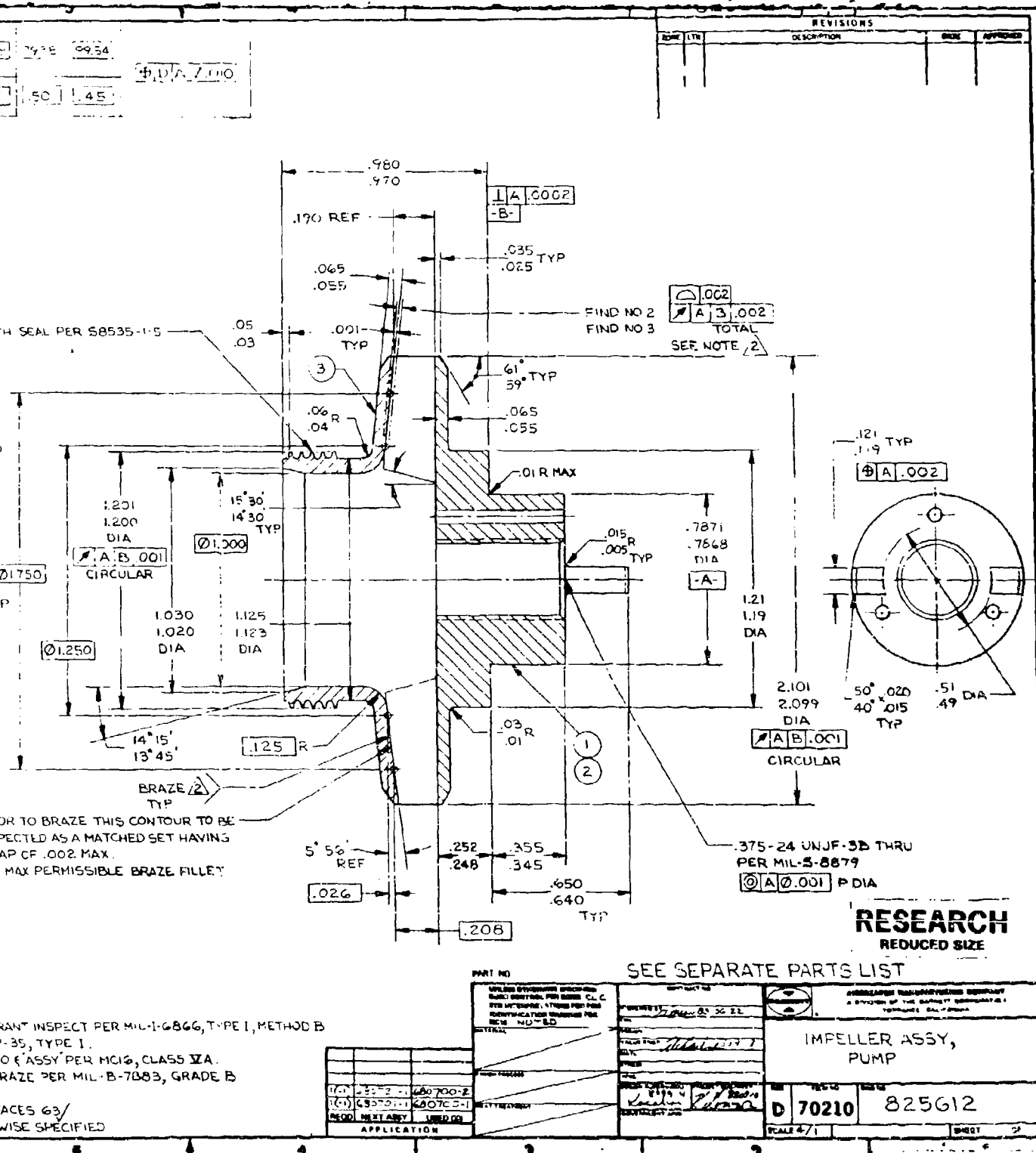


Figure 3-9. Impeller Assembly

### 3.3 MOTOR CONTROLLER DESIGN

The function of the motor controller is to provide variable power synchronous with the voltage and frequency of the pump motor, thereby allowing it to operate as a variable speed machine.

The motor controller design concept was most significantly affected by the initial program assessment to establish the optimum system configuration. Two major changes from the control concept proposed were recommended. These were the change from a voltage source to a current source inverter, and the change from an air-cooled design to a liquid-cooled approach.

The advantages for the current source design are listed below:

- (a) Provides for a simpler control.
- (b) Permits use of a programmable startup concept that eliminates the need for an encoder.
- (c) Is more adaptable to wide load and speed control requirements.

The only negative aspect to the current source inverter is the slightly higher motor losses due to the harmonics in the stator current and the possible need for additional EMI shielding. The change to liquid cooling was recommended to reduce the controller weight and size. Both of these design changes were accepted by the Air Force and were incorporated into the program.

#### 3.3.1 Fundamental Requirements

For proper operation, the permanent-magnet motor (PMM) must be electrically energized from a 3-phase power source which can (1) control the magnitude of current in the stator winding, (2) electrically commutate, i.e., transfer the current between each set of stator windings in a fixed sequence, and (3) control the current so that it is aligned, i.e., synchronous with the flux field established by the permanent magnets within the motor. As indicated in Figure 3-10, maximum mechanical torque is achieved when the rotor flux (due to the permanent magnets) and the stator mmf (due to the winding current) are at right angles. Further, the magnitude of the torque is proportional to the angle ( $\theta$ ) between the flux and mmf (vectors).

##### 3.3.1.1 Inverter-PMM Relationships

Relating the above to a physical 3-phase PMM, the six possible mmf vectors associated with current flow through the three stator windings are as shown in Figure 3-11.

To maintain the maximum average torque, the stator mmf is changed each time the torque angle ( $\theta$ ) is at 60 and 120 electrical degrees. This can be accomplished by supplying the PMM current from a 3-phase inverter. As shown in Figure 3-12, the mmf can be rotated by sequentially closing and opening the switches every 60 electrical degrees to produce a 3-phase rectangular current in each of the stator windings.

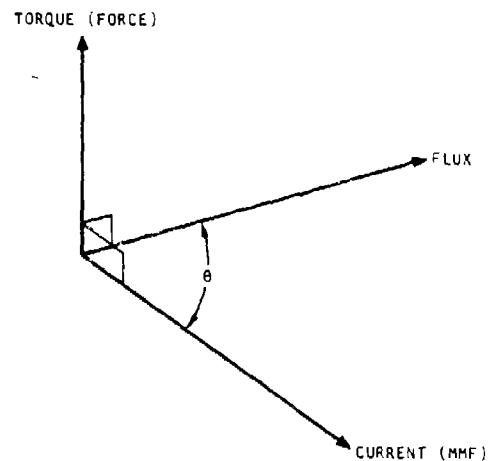


Figure 3-10. Fundamental PMM Electromagnetic Relationship

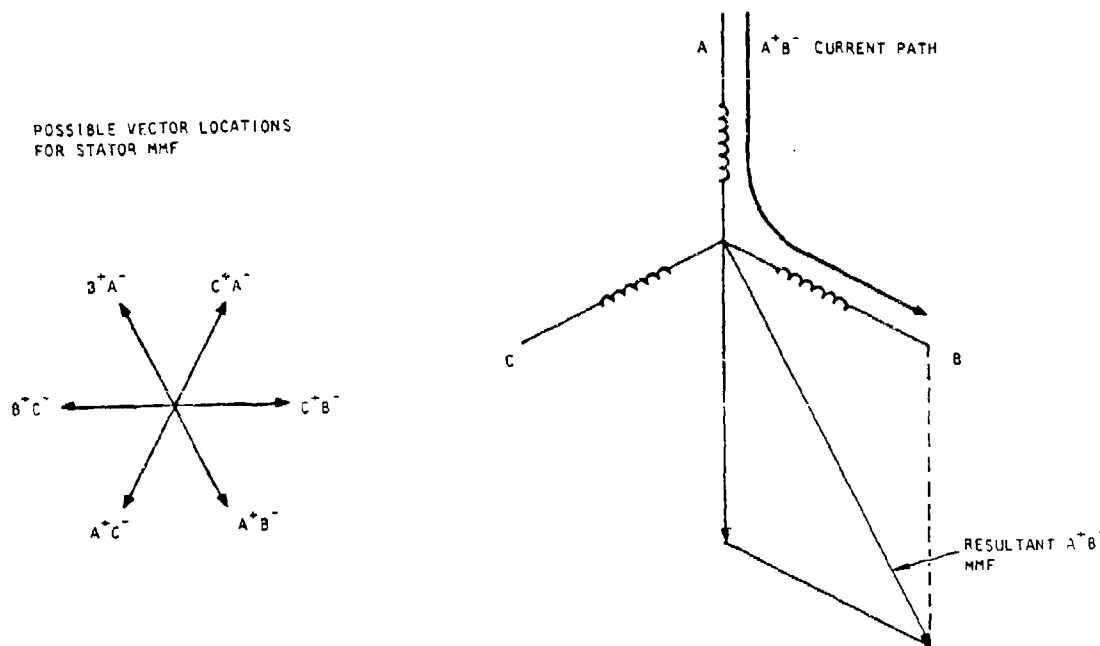


Figure 3-11. Possible MMF Vectors for Stator Winding

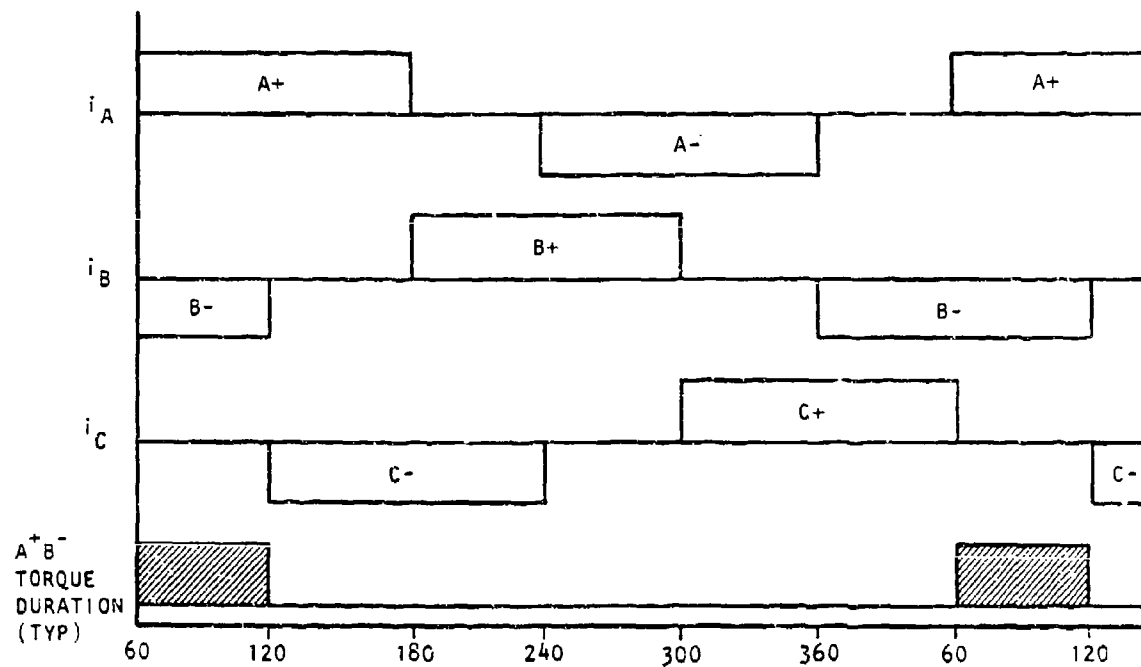
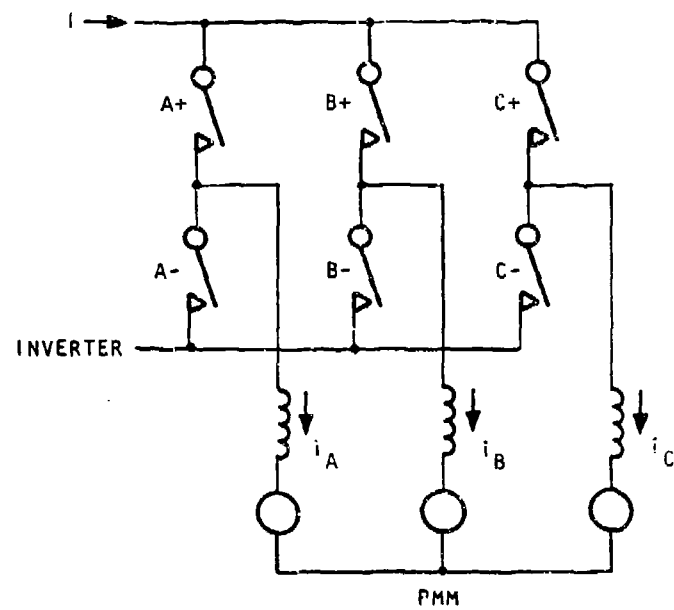


Figure 3-12. Inverter Switching Schematic and Current Wave Form

### 3.3.1.2 Inverter-PMM Control

To achieve the desired relationship between the stator mmf and the rotor flux, some form of control is required. One method is to use a PMM rotor (shaft) position sensor to "mechanically detect" when each of the six stator mmf vectors are at 60 and 120 electrical degrees relative to the rotor flux vector. An alternate method is to monitor the PMM terminal voltage during the times that phase current is zero, i.e., 180 to 240 and 360 to 60 electrical degrees as shown in Figure 3-12 for the A-phase current. However, since the magnitude of the PMM terminal voltage is proportional to its rotor speed (rpm), voltage monitoring cannot be used for initial startup of the PMM.

To resolve this limitation, shaft position sensors can be used until sufficient PMM terminal voltage is generated for electrical monitoring purposes, or a third method can be used. This third method is termed inverter frequency "ramp start." The inverter is preprogrammed to produce a given current magnitude in, for example, PMM phase A+ and B- windings. The current magnitude is sufficient to produce a mechanical torque that aligns the rotor flux vector at right angles to the resultant current or mmf vector. Once aligned, the inverter output current frequency slowly increases from zero (dc) at a predetermined rate (ramp). As the current is commutated from winding to winding, a torque is produced to cause the PMM rotor to advance and keep in "sync" with the now electrically rotating mmf vector. The frequency of commutation is increased linearly with time in this implementation.

At approximately 10 percent of the PMM rated speed, PMM terminal voltage is at a sufficient level to allow for reliable monitoring. Above 10 percent of rated speed, voltage monitoring is used to provide the necessary synchronous control.

As the PMM rotor accelerates towards rated speed, the inverter control logic must change from closed loop current-open loop position control to closed loop speed-closed loop position control at the aforementioned 10 percent of rated PMM speed.

During the ramp mode, the inverter determines the frequency or rpm of the PMM. In the voltage mode, the PMM determines the frequency output of the inverter.

### 3.3.2 Initial Design Considerations

The basic functions of the motor controller are shown in Figure 3-13 and are identified as (1) rectification and control of the 400-Hz source for startup, (2) rectification and control of the 9-phase generator after startup, (3) inversion of the rectified voltage/current for synchronous power transfer to the PMM, and (4) commutation, i.e., turnoff of the power semiconductors used within the inversion process.

#### 3.3.2.1 Optimum Motor Controller Topology

To achieve the minimum weight configuration, a comparison of candidate motor controller topologies was made.

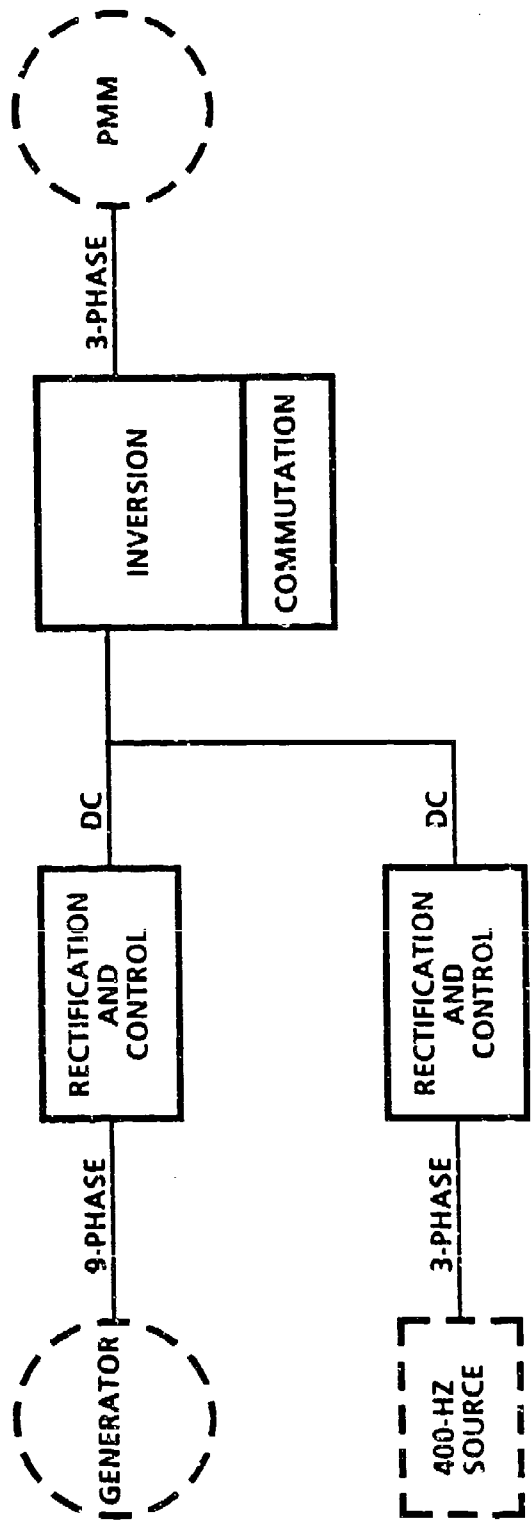


Figure 3-13. Basic Motor Controller Functions

The six configurations analyzed the basic power circuit topologies described below.

Option 1--Diode rectification - transistor boost chopper -transistor buck chopper - transistor inverter

Option 2--Diode rectification - transistor buck chopper - transistor inverter

Option 3--Diode rectification - transistor buck chopper - thyristor inverter

Option 4--Thyristor rectification (phase-delay rectifier, PDR) - thyristor inverter

Option 5--Thyristor cycloconverter

Option 6--Thyristor rectification (PDR) - transistor inverter

The bases for the tradeoff study were the input 9-phase wild-frequency, wild-voltage (WFVW) characteristics, the motor controller output power requirements for the PMM, and the controller-to-PMM power factor interface shown in Figures 3-14, 3-15, and 3-16, respectively.

Each of six candidate motor controllers was graded on the following bases:

- (a) Size
- (b) Weight
- (c) Reliability or complexity
- (d) Effect on permanent-magnet motor interface
- (e) Effect on source interface
- (f) Power semiconductor limitations--thyristor vs transistor

The thyristor rectifier with thyristor inverter control (Option 4) provided the best overall approach. The trade study comparisons are shown in Table 3-3. The key size and weight parameter comparisons are shown in Figure 3-17. It appeared that the program goal of 50 pounds maximum for the control was not achievable even with the selected optimum configuration.

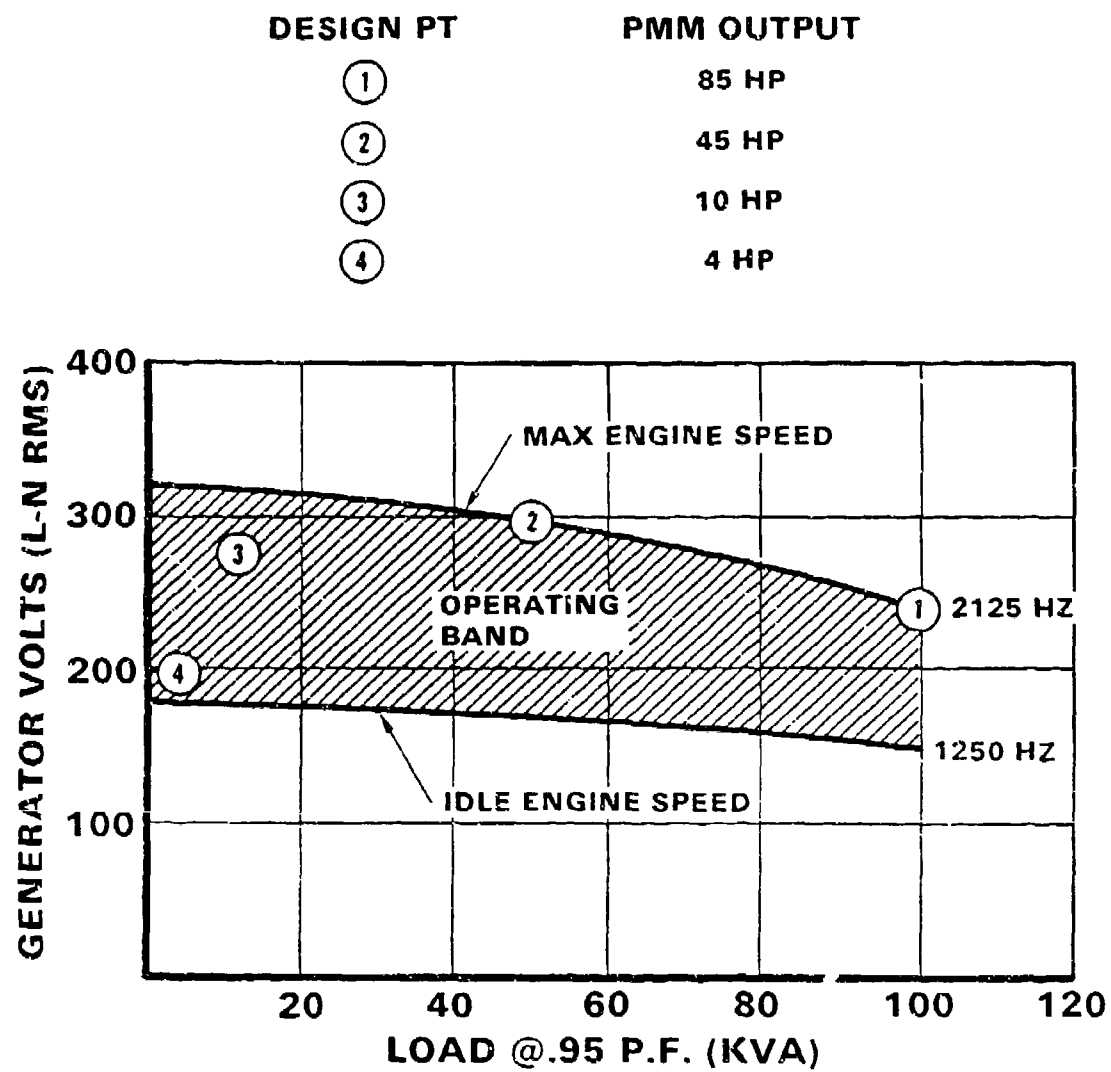


Figure 3-14. WFWV Characteristics

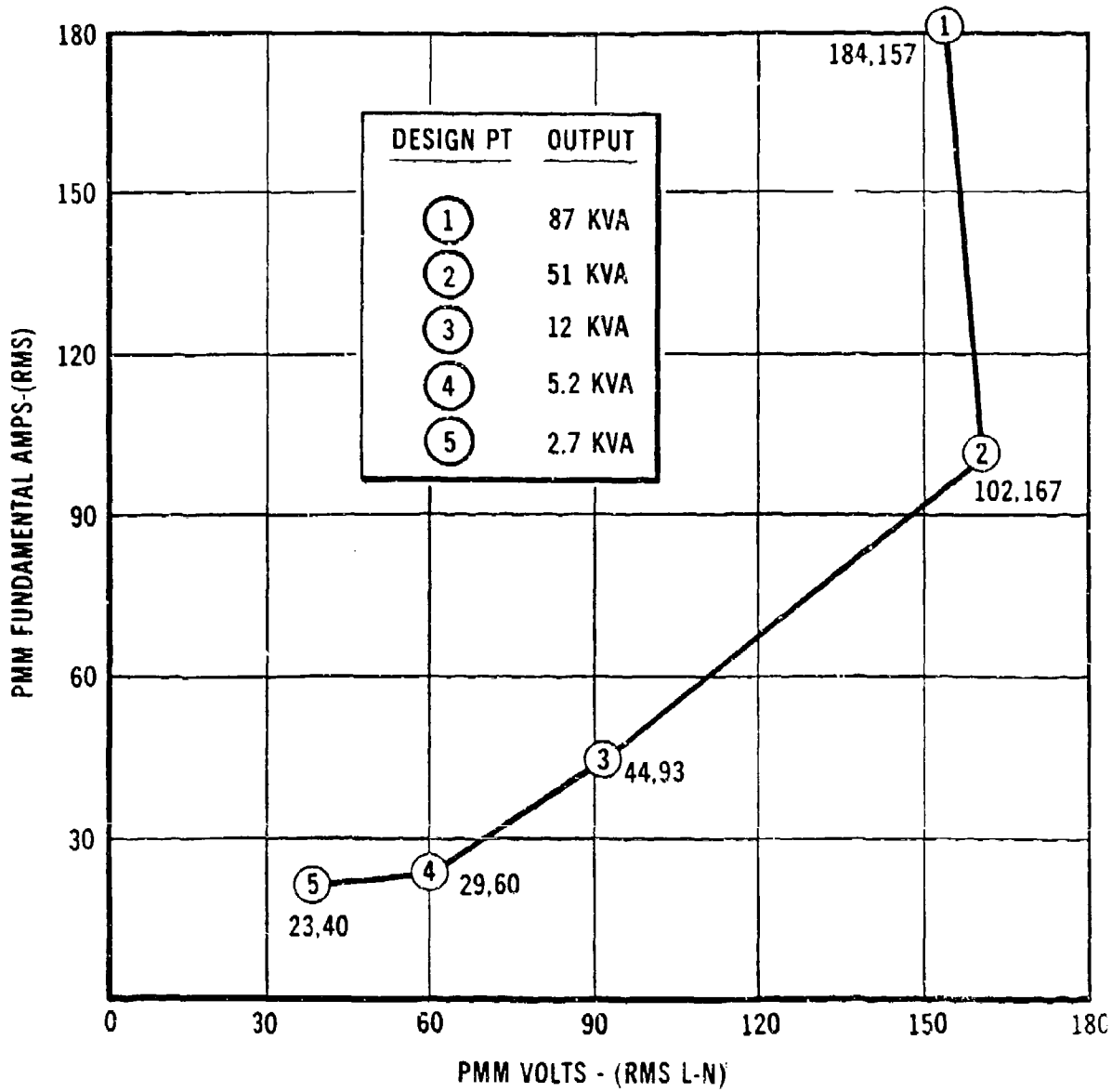


Figure 3-15. Motor Controller Output Profile

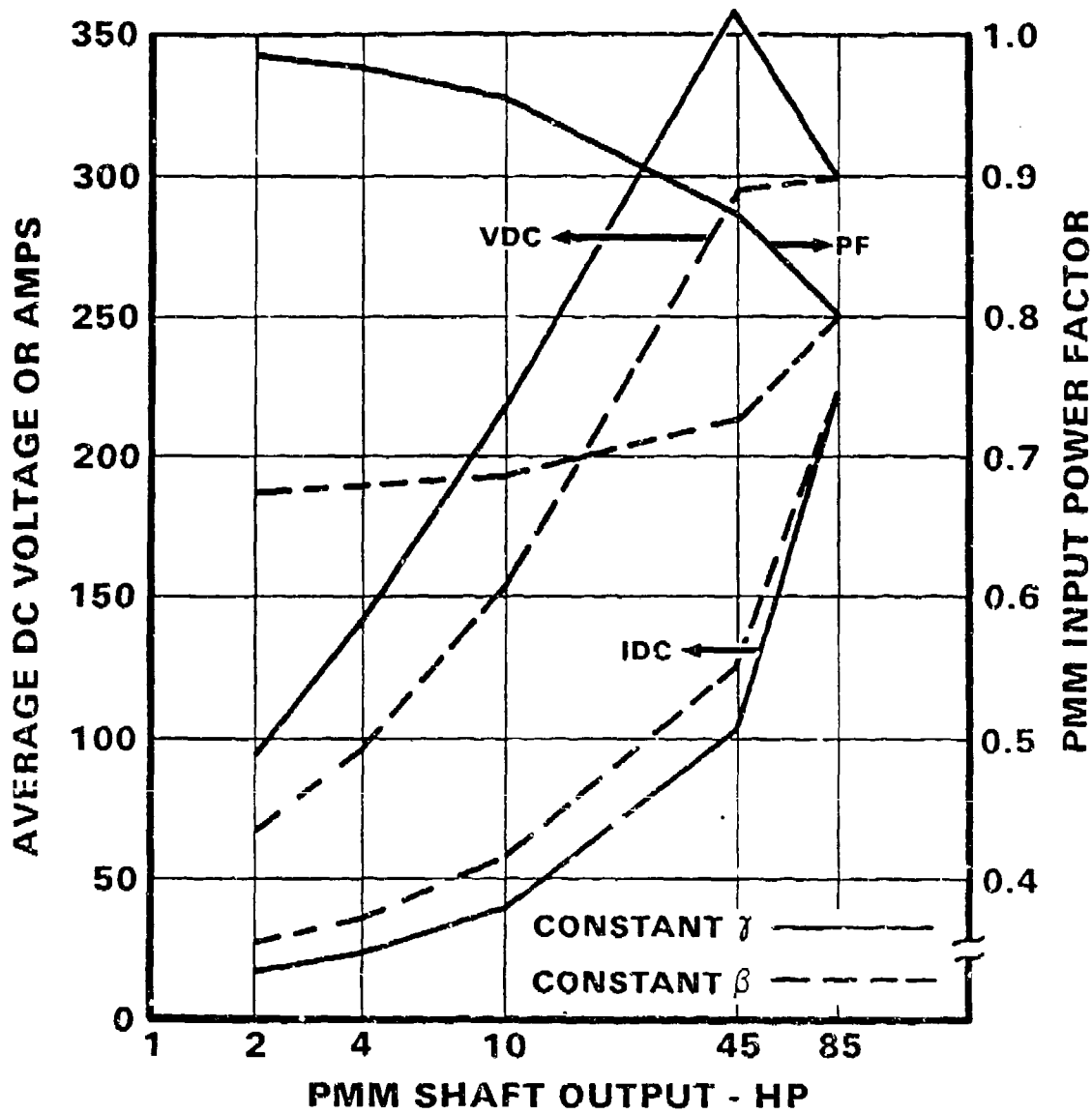


Figure 3-16. Motor Controller Interface

TABLE 3-3. Tradeoff Matrix

<u>OPTION</u>	<u>1</u>	<u>2</u>	<u>3</u>	<u>4</u>	<u>5</u>	<u>6</u>
INVERTER TYPE	1	1	1	1	V	1
POWER STAGES	4	3	3	2	1	2
# POWER DEVICES	25	32	25	17	54	21
# ACTIVE DEVICES	12	17	10	17	54	21
MAGNETIC WT (LB)	21	16	14	9	24	9
AL ELECT CAP	YES	YES	YES	NO	NO	NO
SIZE (FT <sup>3</sup> )	3.1	2.8	2.3	1.8	3.0	3.0
WEIGHT (LB)	152	116	92	73	149	77
INPUT PF @ 45 HP	0.66	0.66	0.66	0.58	0.8	0.58
OUTPUT PF @ 45 HP	1.0	1.0	0.8	0.8	1.0	1.0
PMM RATING (KVA)	37.7	37.7	47.1	47.1	41.9	37.7
POSITION SENSOR	NO	NO	YES	NO	YES	NO
LOGIC CARDS	6	6	5	7	14	7
SENSORS	4	2	2	5	4	4
RELATIVE SCORE	1.34	1.20	1.13	1.00	1.73	1.03

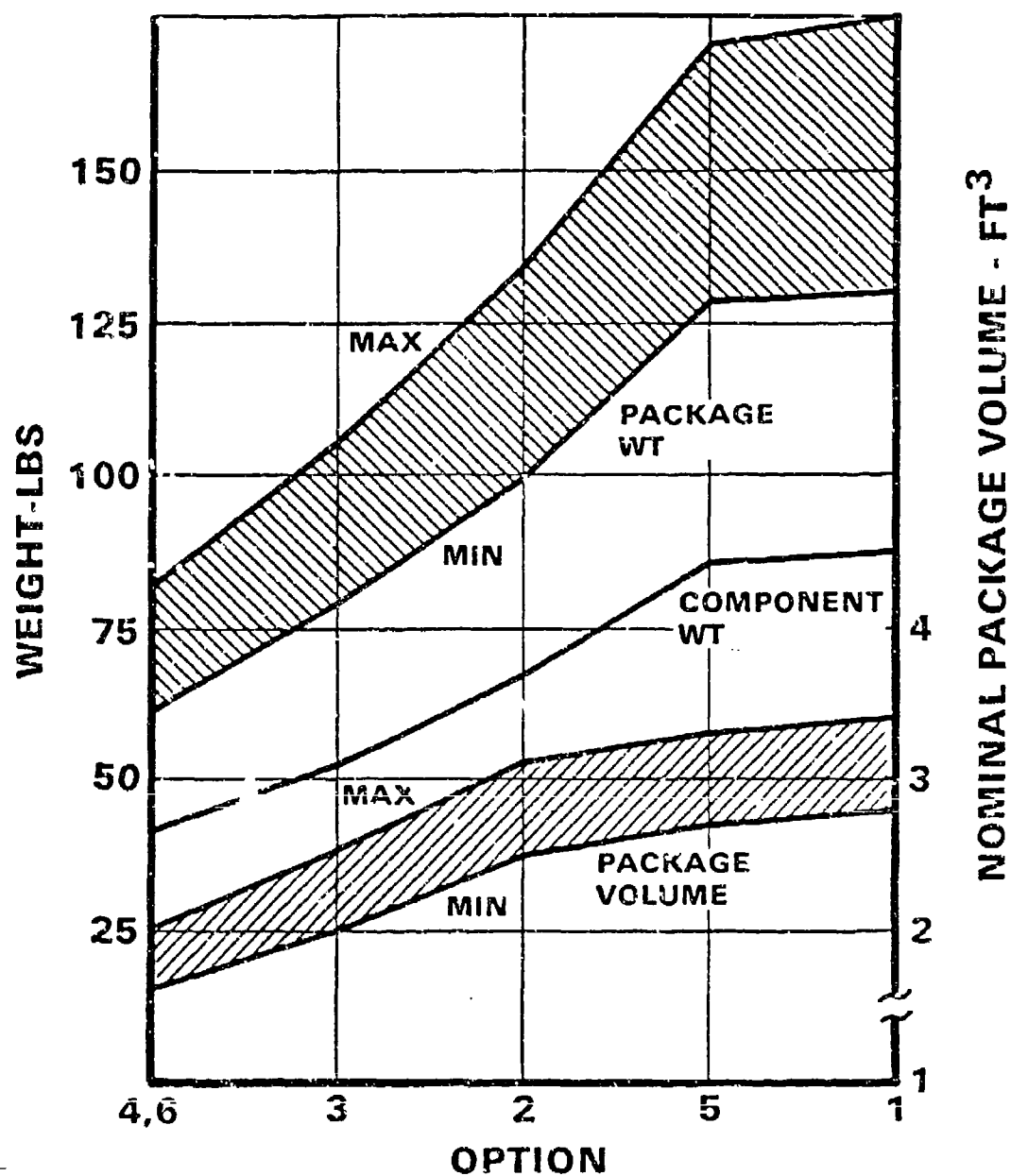


Figure 3-17. Motor Controller Option Parameters

#### 4. HARDWARE FABRICATION

The main component fabrication activities are described in this section. In-process photographs and exploded views are used to help define the assembly procedures.

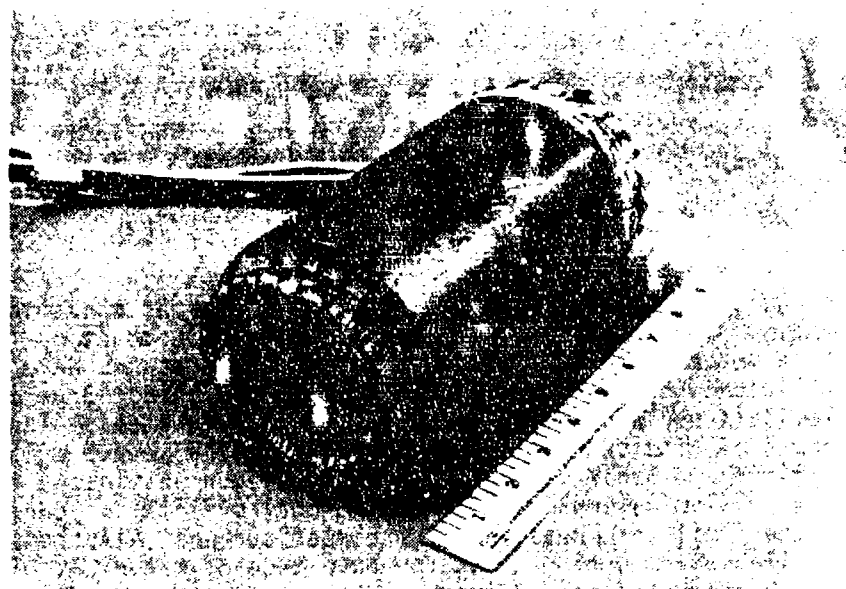
##### 4.1 MOTOR ASSEMBLY

The motor has two basic electromagnetic parts, the stator assembly and the rotor assembly. The stator assembly is similar in construction to a 3-phase induction motor stator. Two different laminated stacks were built to evaluate the efficiency benefit which could be achieved using 48-percent nickel-steel laminations in place of conventional silicon-steel. The nickel laminations were 4 mils thick and the silicon laminations were 5 mils thick. The thin laminations are beneficial in limiting eddy current losses in the iron. Silicon steel laminations without directional orientation cannot be procured below the 5-mil thickness; so, the comparison was valid considering the thinnest available lamination stock for each type of material. The laminations were punched and bonded into a stack, and the outer diameter was ground to a precision diameter for shrink-fitting into the housing. The stack was then wound using polyimide-coated magnet wire and Nomex and Kapton insulators to provide a full 220°C system. A photo of a wound stator assembly is shown in Figure 4-1.

The permanent magnet rotor assembly shown in Figure 4-2 is more unique. Figure 4-3 shows the rotor assembly parts except for the magnets. Stator laminations are also shown in the foreground of this photo. The rotor shaft has four milled flats to provide a base for the magnets. Figure 4-3 shows the round disks at each end of the flats to provide full magnet support and containment. An aluminum cage slips over the shaft and provides pockets for mounting the rectangular block magnets and, functionally, acts as a damper cage around each magnet pole. The Inconel 718 sleeves pictured are shrunk over the shaft/magnet assembly after the magnets have been installed and precision ground. Figure 4-4 shows the process of "loading" a magnetized magnet into the damper pocket. This process requires delicate control, because the magnet tends to pull toward the shaft. Any impact on assembly could result in cracked or chipped magnets. Figure 4-5 is a photograph of the sleeve installation process. The sleeve is heated inside the insulator at the bottom of the press while the finished ground shaft/magnet assembly is cooled in liquid nitrogen. When proper temperatures are reached, the shaft/magnet assembly is attached to the pneumatic press and quickly forced down into the hot sleeve. The sleeve immediately contracts onto the cold magnet assembly and the rotor assembly is then withdrawn from the induction heating coil and quenched. The quench is done to minimize heat encroachment into the magnets, thus preventing irreversible loss of magnet flux.

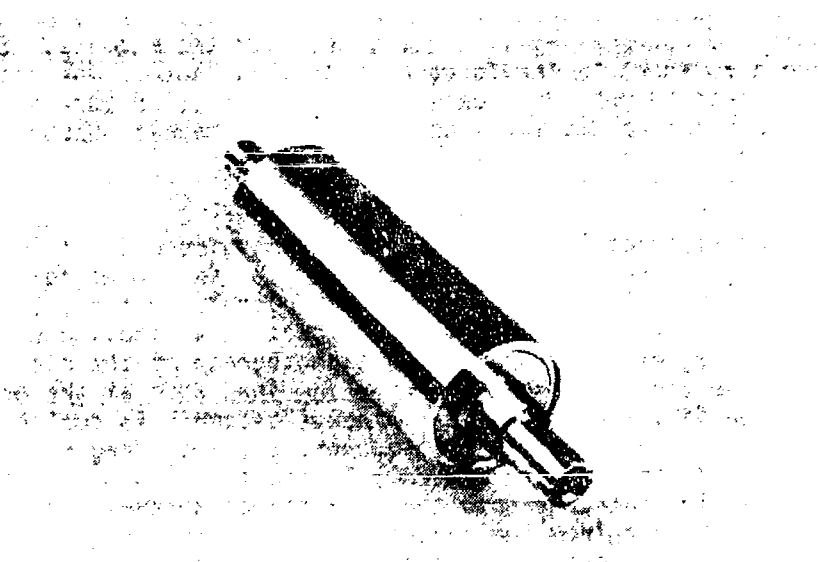
##### 4.2 PUMP HARDWARE

The pump details consist of an inlet assembly, a pump housing, the impeller, and associated ring and labyrinth seal hardware. All these details



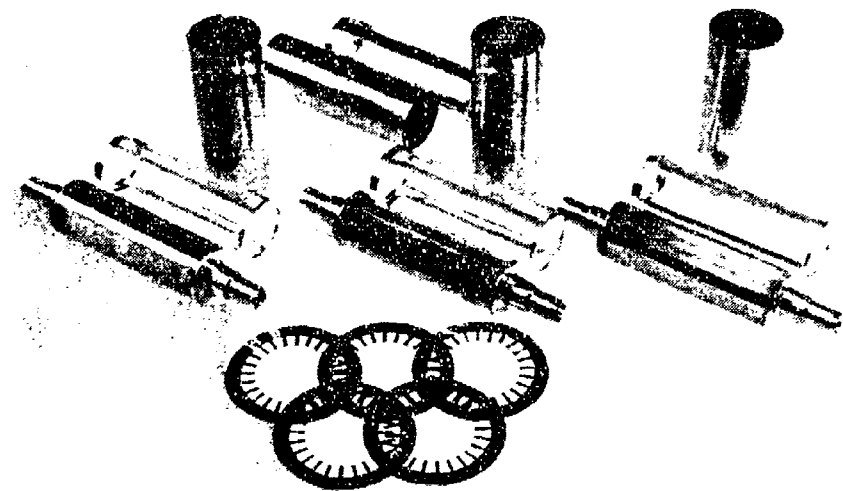
90680-2

Figure 4-1. Completed Stator Assembly



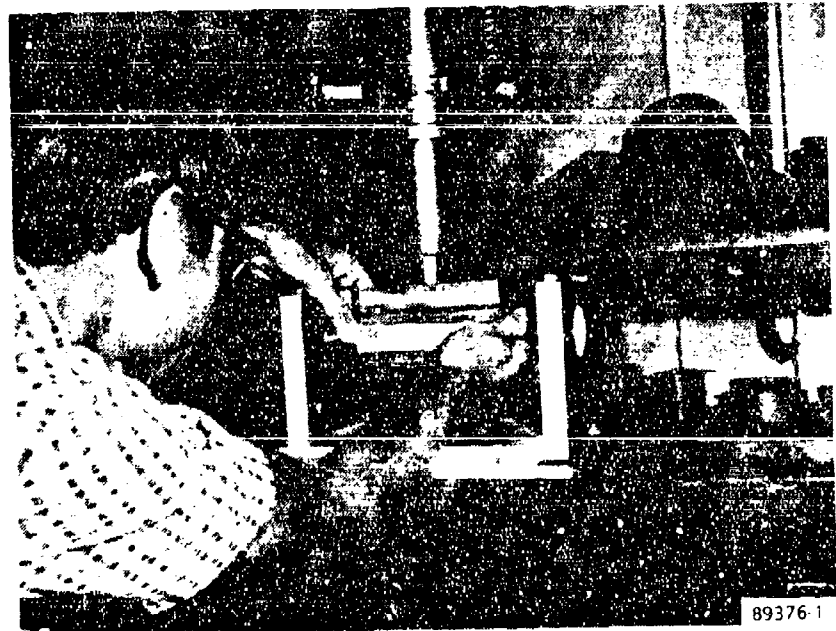
90680-3

Figure 4-2. Completed Rotor Assembly



89206-1

Figure 4-3. Rotor Assembly Details and Stator Laminations



89376-1

Figure 4-4. Installation of Magnets

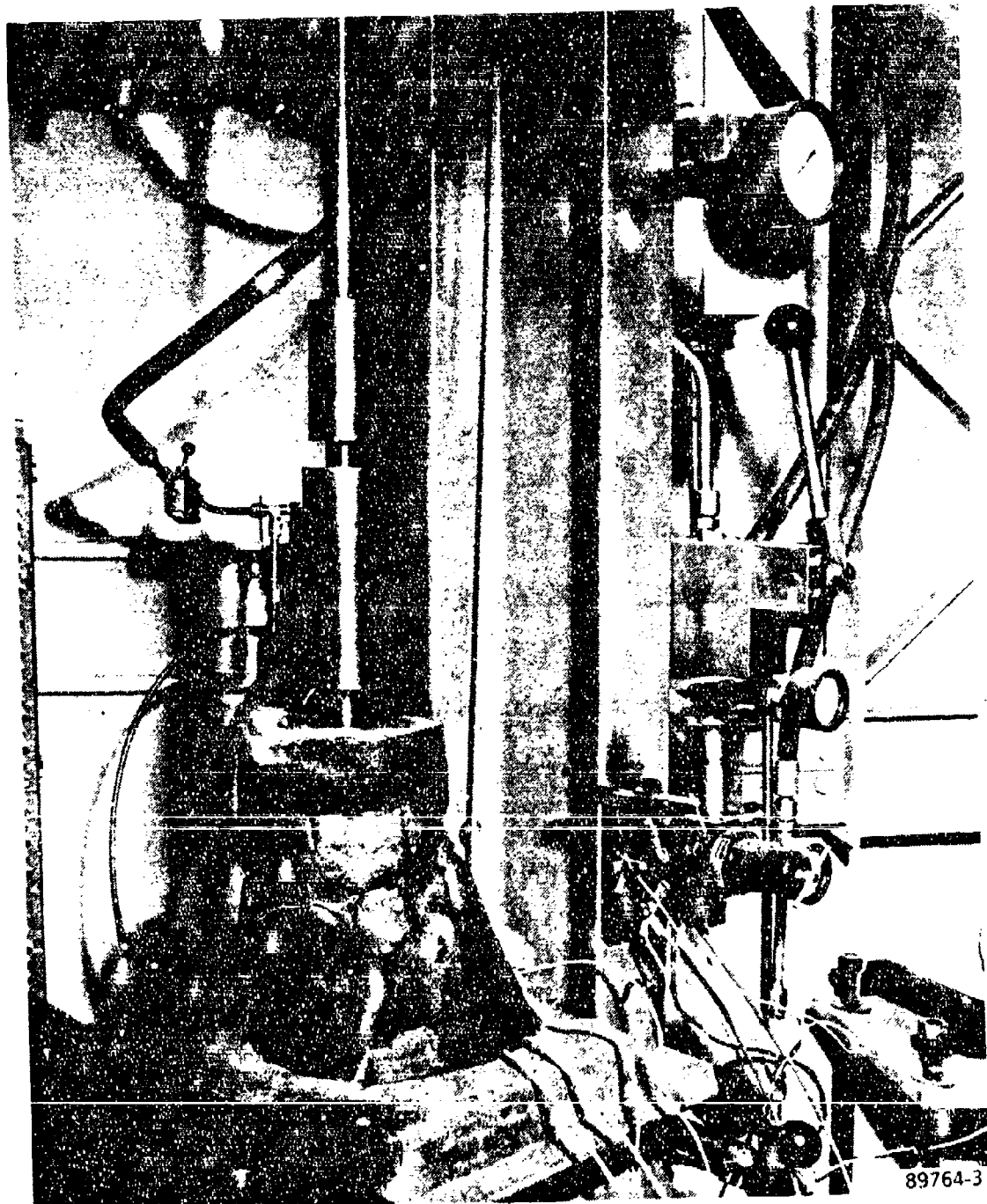


Figure 4-5. Rotor Assembly Being Withdrawn from Induction  
Heater with Sleeve Installed

are machined or machined and welded, except for the pump impeller. The impeller consists of two pieces, one being a disk with a shaft stub. The impeller blades are milled into the face of the disk. The second piece provides the closing plate for the milled side of the impeller disk. These two mating surfaces require a precision fit and are brazed together to make the impeller assembly. A labyrinth seal is machined on the closing disk to preclude high-pressure pump output flow leaking directly back to the pump inlet. A second labyrinth ring seal is shrunk onto the impeller hub to protect against flow into the front bearing cavity. Figures 4-6 and 4-7 provide a plan view and an isometric view, respectively of the impeller assembly.

All the details used in the motor and pump assembly are shown in Figure 4-8, which is an exploded view of the complete unit. The top row shows the inlet assembly, pump housing assembly, the rear bearing housing assembly, the stator housing assembly, and the back cover. In the center of the picture is the tie bolt. The bottom row has the main rotating members and some seal parts. Proceeding left to right, the impeller and labyrinth ring seal are first. The rotor assembly is flanked by bearings, carbon face seals, and face seal rings. The bearing preload spring and support hardware follow with the proximity probe disk at the end of the assembly. The motor-driven pump installation dimensions are shown in Figure 4-9.

#### 4.3 SELECTED MOTOR CONTROLLER

A block diagram of the motor controller selected for the program is shown in Figure 4-10, and a schematic diagram of the power stages is given in Figure 4-11.

Physically, the motor controller layout consists of a modular array as shown in Figure 4-12, wherein the various semiconductors are mounted on integral mechanical, thermal, and electrical oil-cooled heat sinks.

The nine wild-frequency, wild-voltage (WFWV) semiconductors and six inverter thyristor semiconductors are assembled in a similar manner by "stacking" them in a configuration that allows for double-sided cooling of the disc or "hockey-puck" semiconductor.

Each side of the semiconductor is in contact with an aluminum heat sink that also serves as an electrical interconnection. Figure 4-13 shows the arrangement for the 3-phase inverter thyristor assembly. Details of the cast-aluminum heat sink are shown in Figure 4-14.

The 400-Hz and inverter commutation semiconductors, thyristor gate drivers, controller voltage sensors, and thyristor voltage suppression networks are mounted to a separate oil-cooled heat sink.

The fourth depicted subassembly houses the control logic cards consisting of:

- (a) PMM position sensor
- (b) Inverter firing

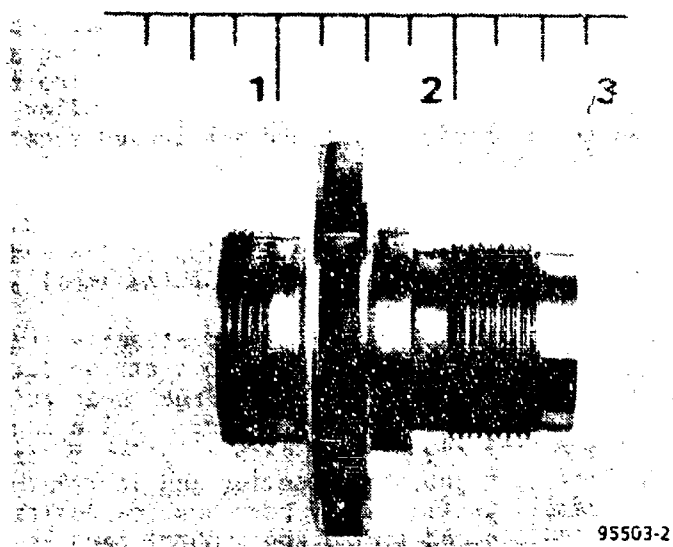


Figure 4-6. Plan View of Impeller Assembly

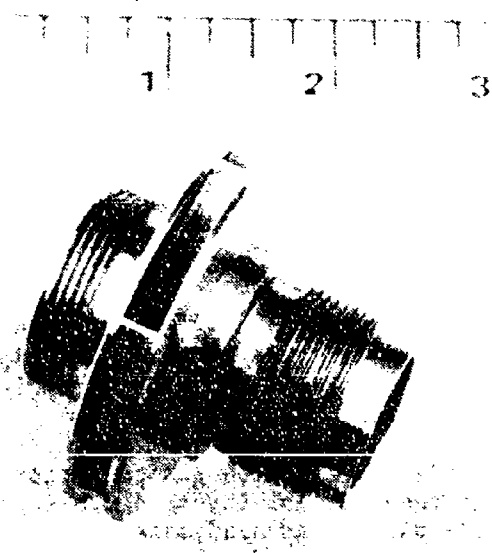


Figure 4-7. Isometric View of Impeller Assembly

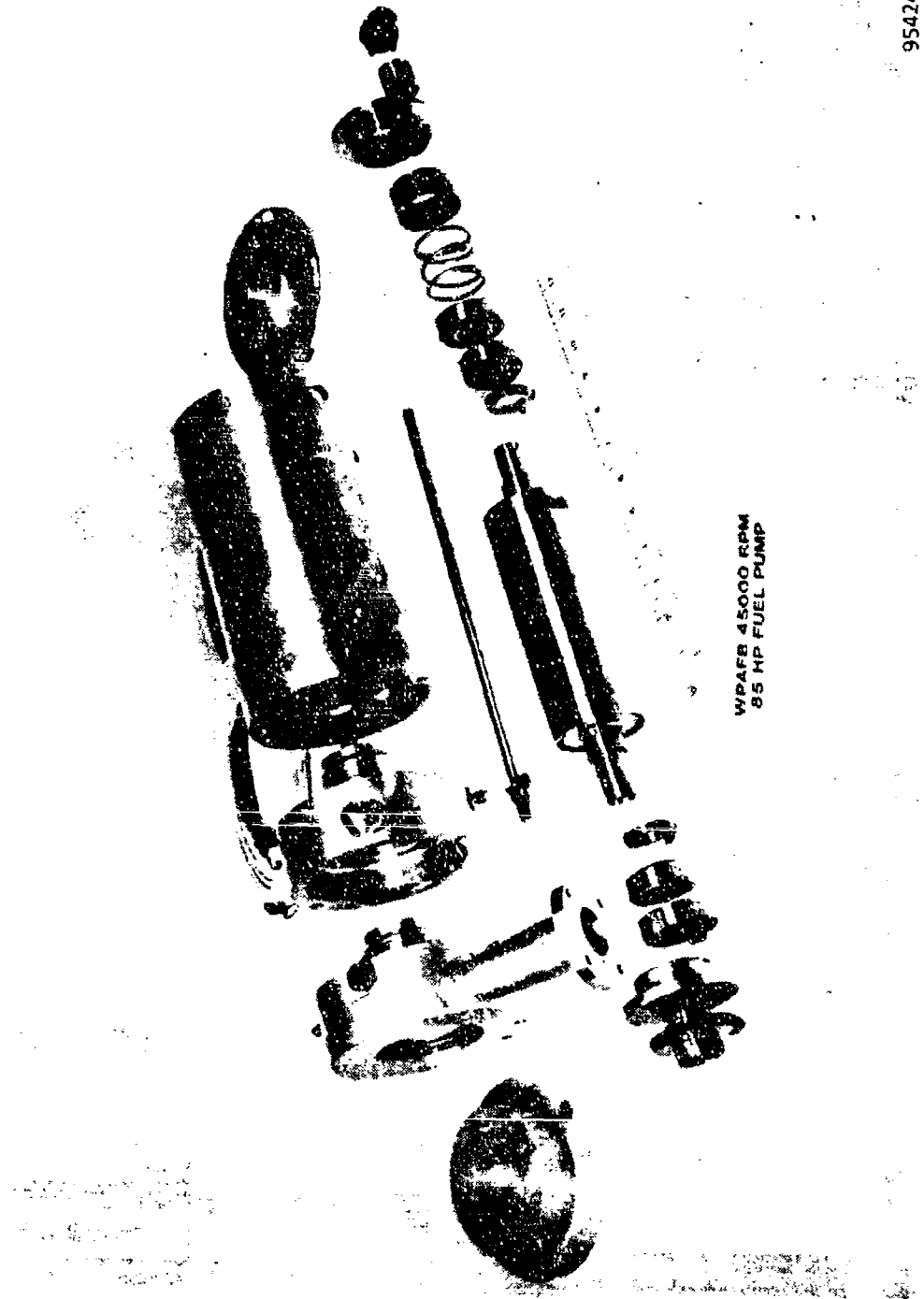
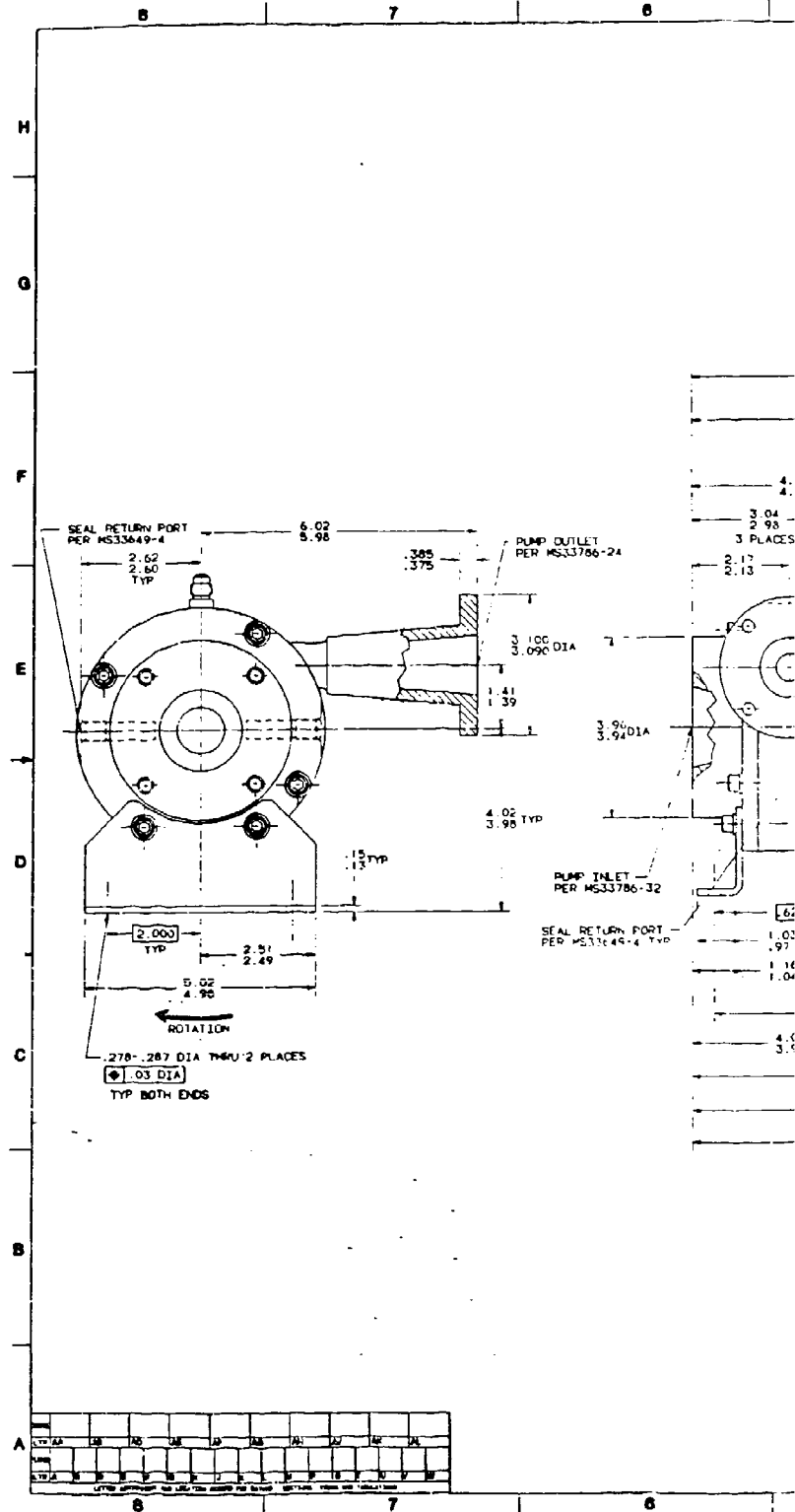


Figure 4-8. Exploded View of Motor and Pump Unit



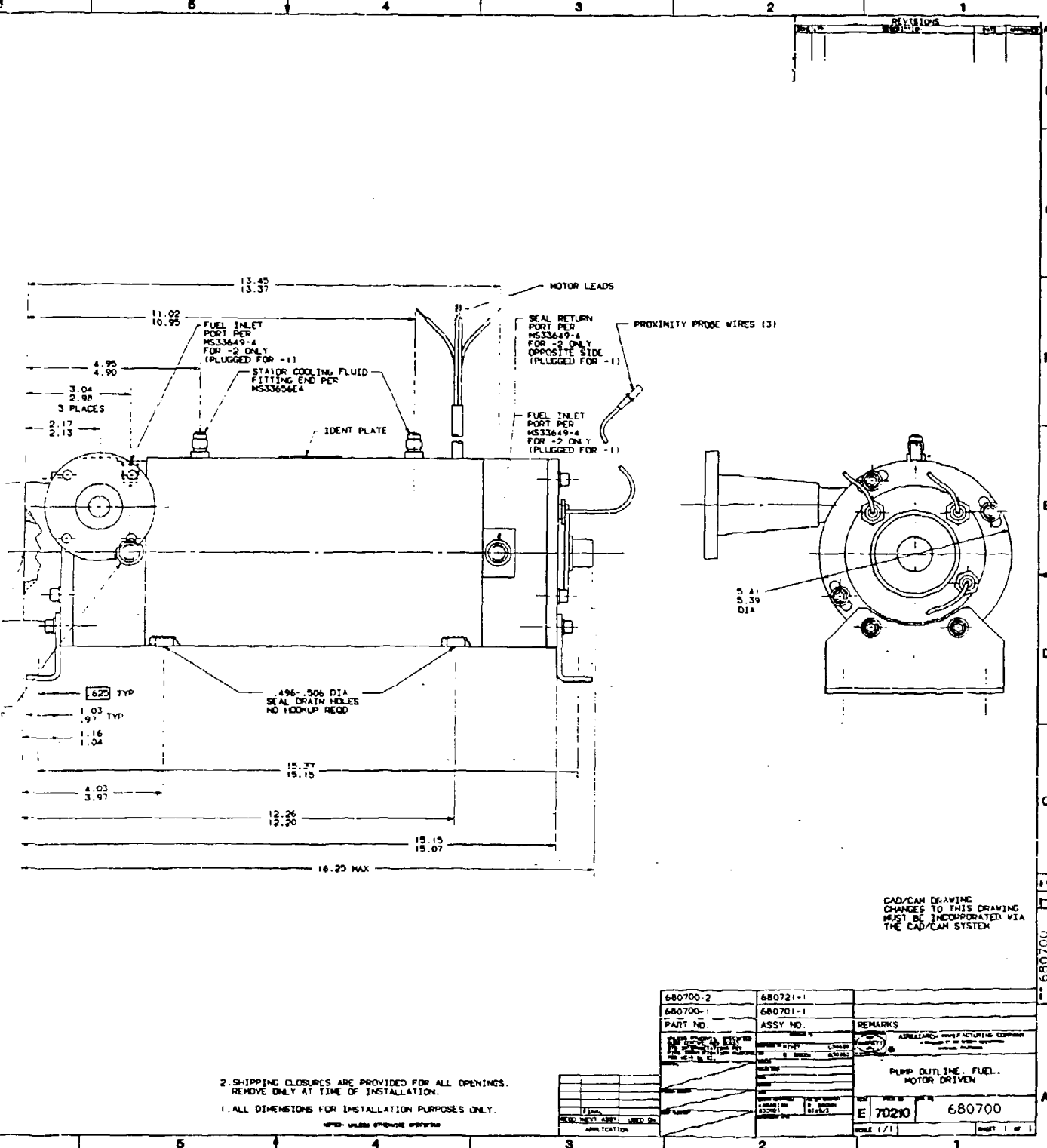


Figure 4-9. Pump Outline

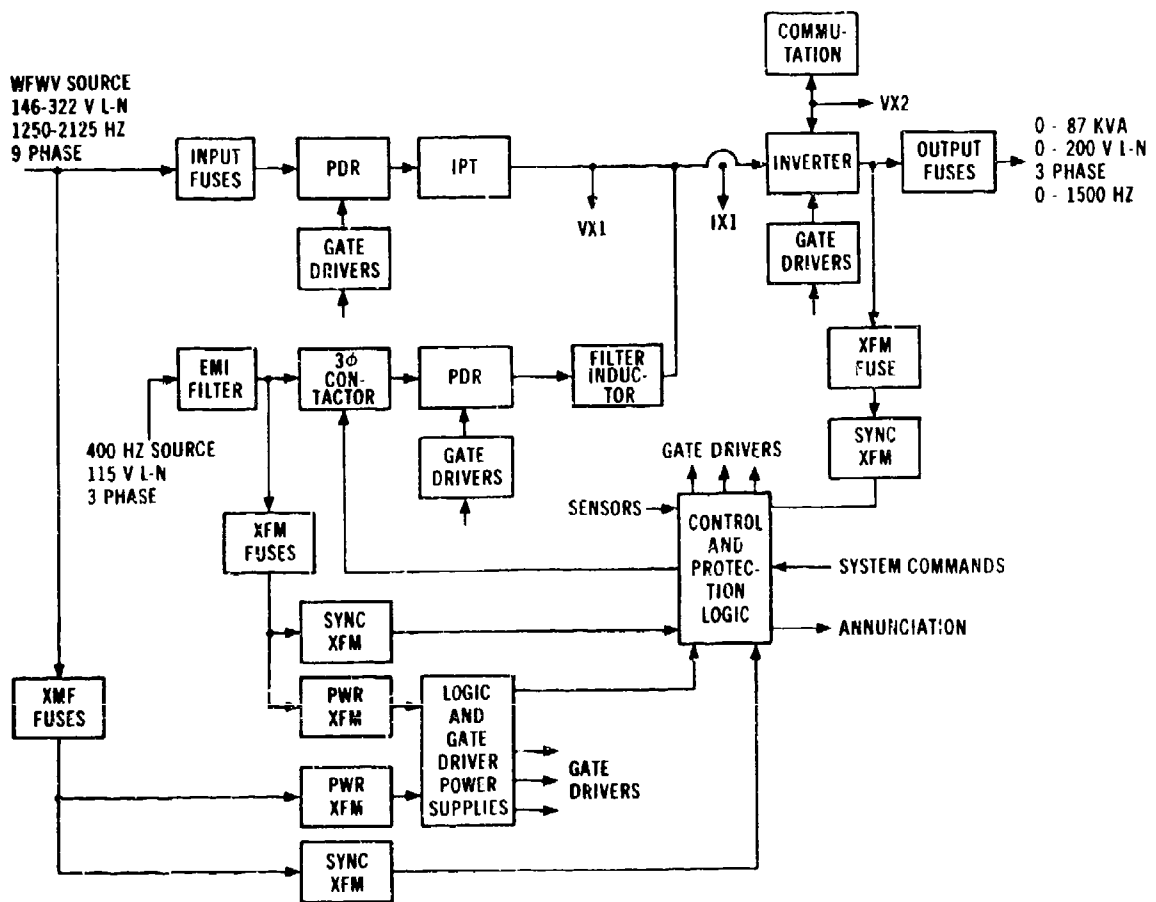
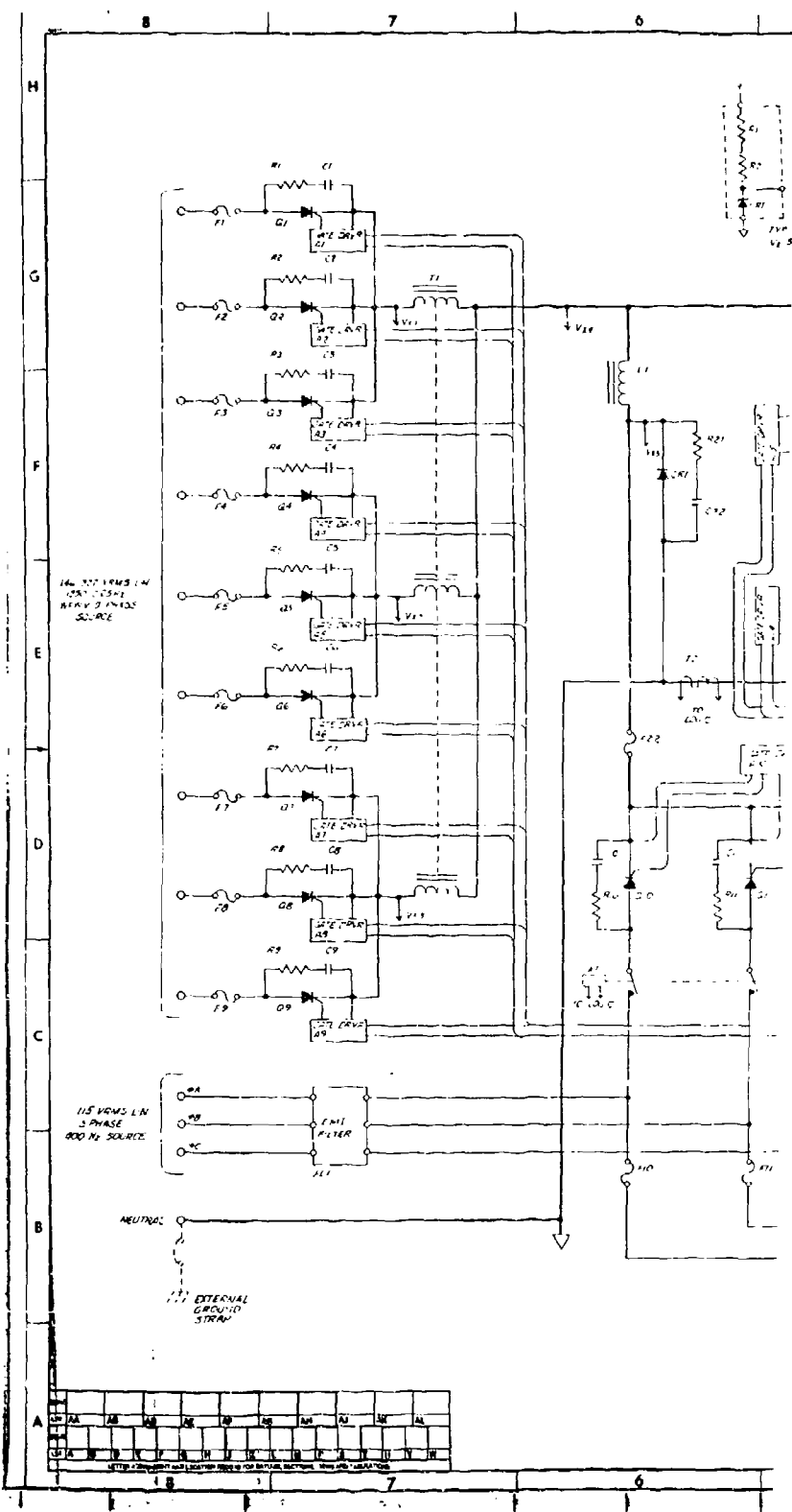


Figure 4-10. Fuel Pump Motor Controller Block Diagram



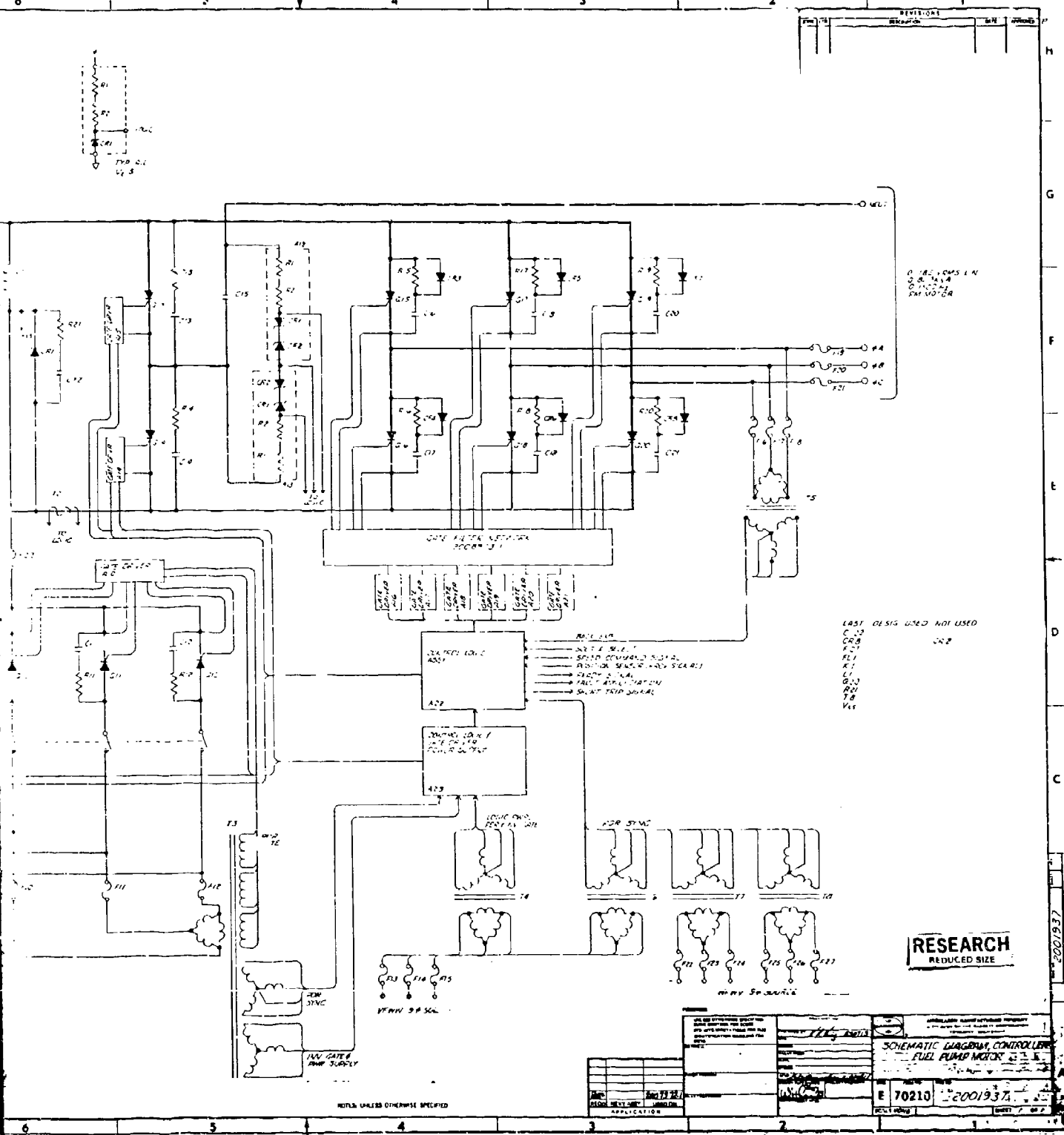


Figure 4-11. Motor Controller Schematic

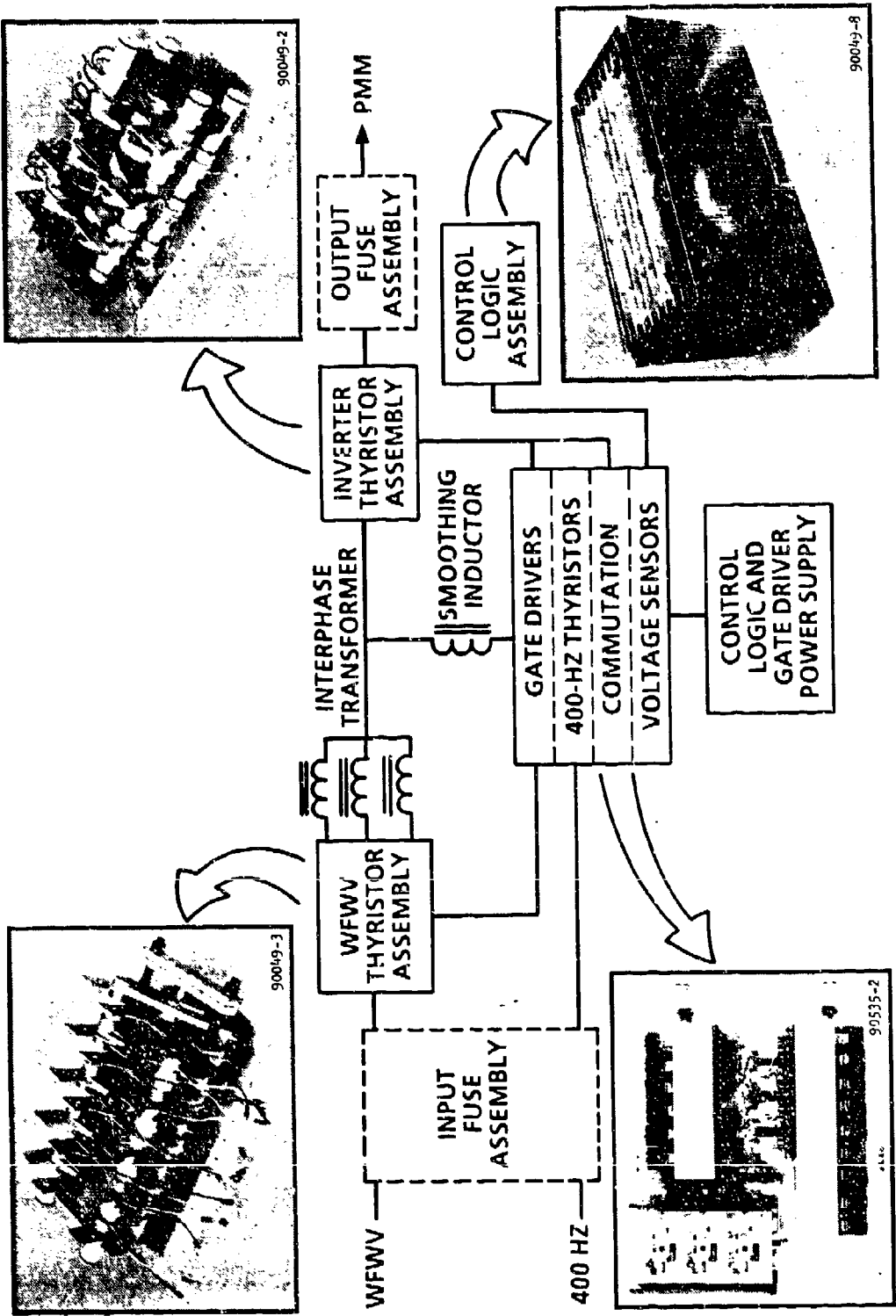


Figure 4-12. Motor Controller Modules

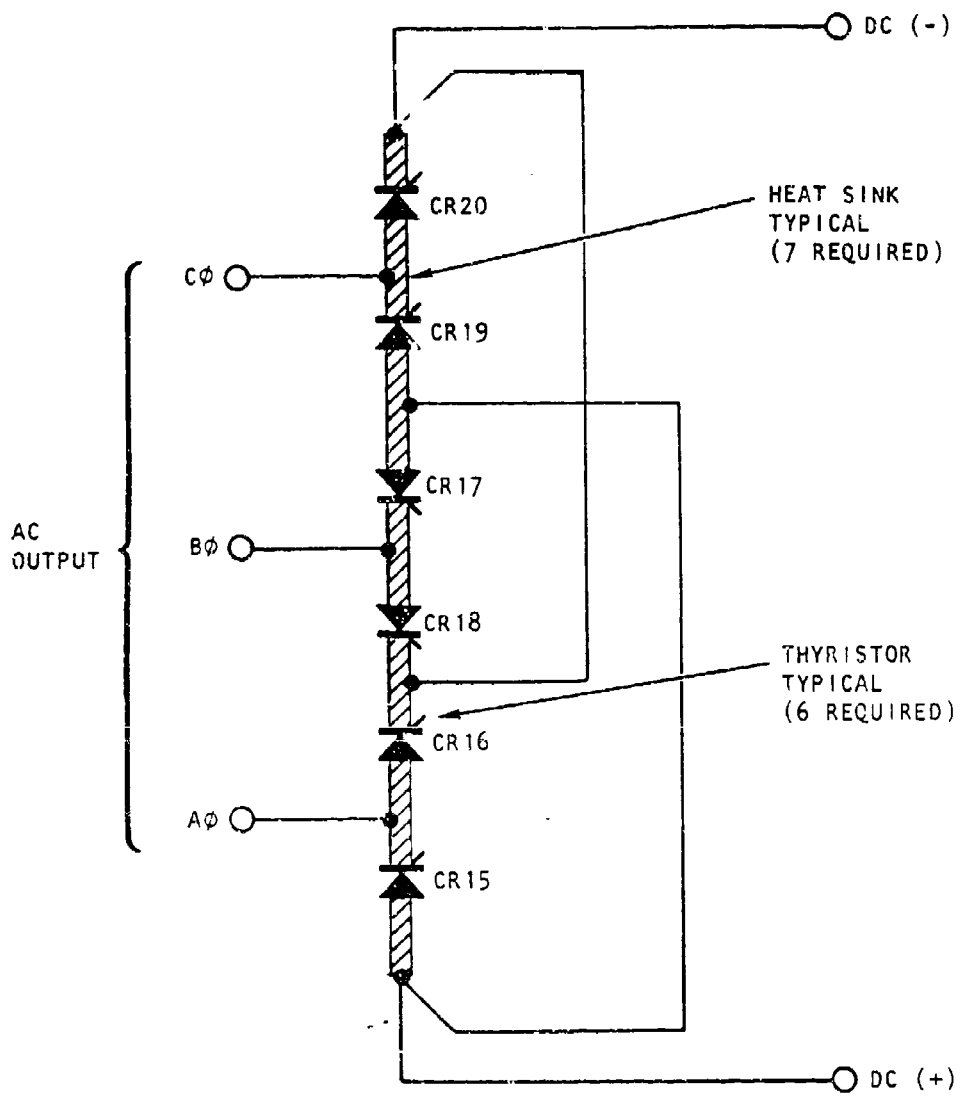


Figure 4-13. Inverter Thyristor Mechanical, Thermal, and Electrical Arrangement

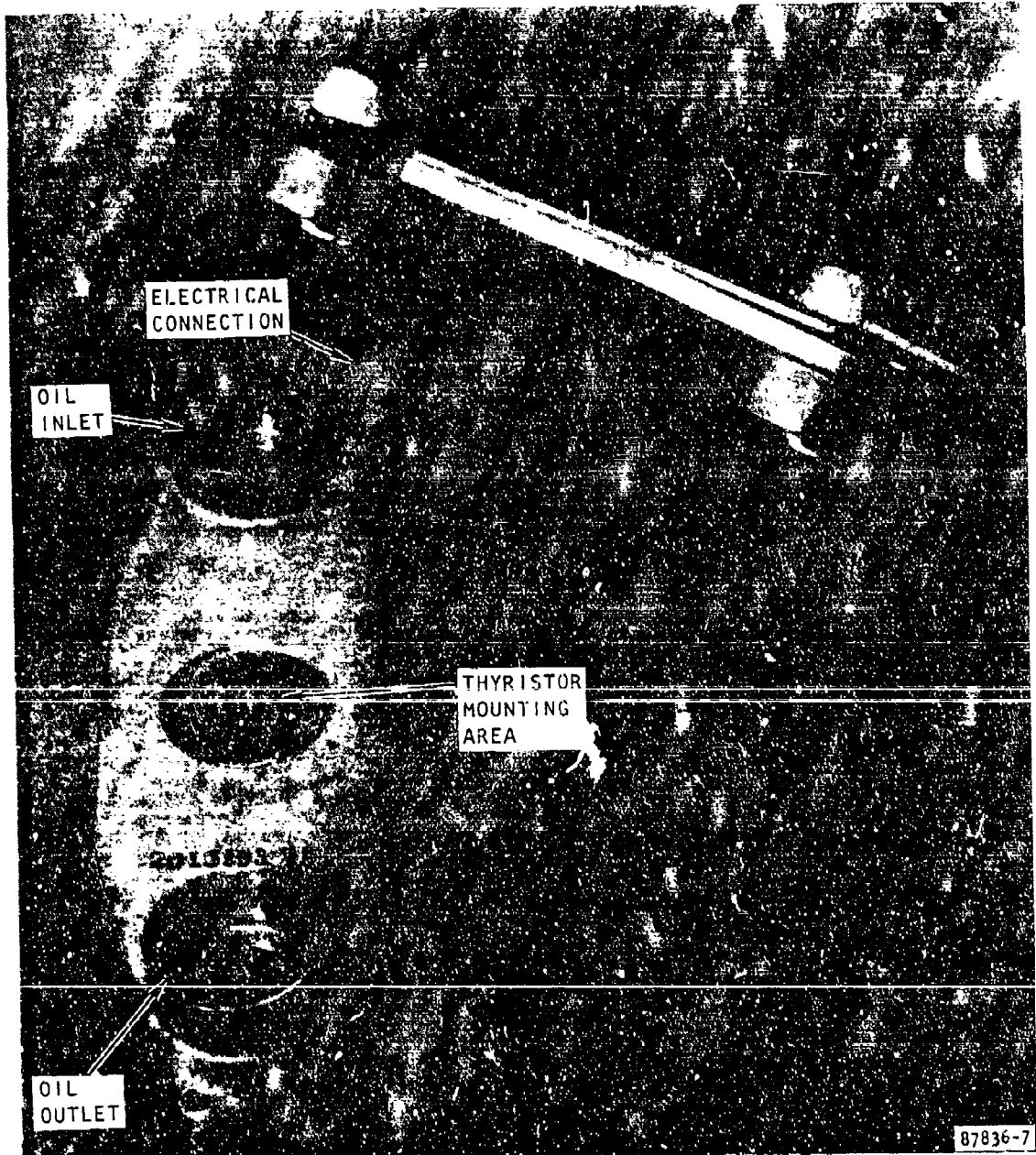


Figure 4-14. Cast Aluminum Heat Sink

- (c) Inverter commutation
- (d) WFWV thyristor firing
- (e) PMM current and speed regulator

Figure 4-12 also shows functional circuitry related to semiconductor and voltage sense transformer fire protection, WFWV thyristor interphase transformer, 400-Hz thyristor dc current smoothing inductor, and control logic and gate driver power supply.

The motor controller modules and related circuit are packaged in an integrated enclosure shown in Figure 4-15.

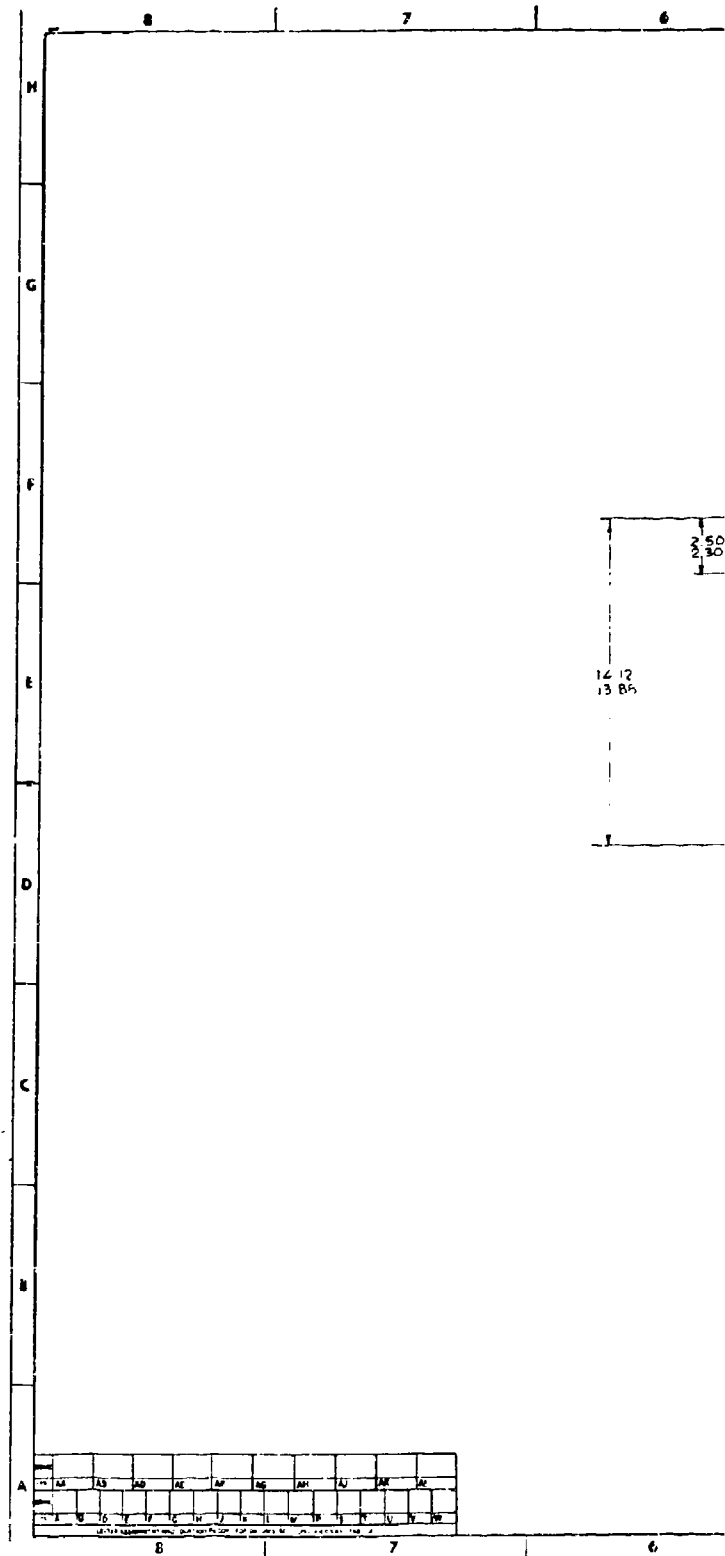
#### 4.3.1 Control Panel

To assist in the developmental testing of the motor controller, as well as provide for the necessary system level control and protection functions, a separate control panel was designed and fabricated.

The system control panel contains the following circuit elements or functions:

- (a) Start (ON/OFF) switch
- (b) Motor controller ready indicator light
- (c) Source select switch, i.e., 400-Hz or WFWV power input
- (d) Speed control potentiometer for linear speed commands
- (e) Speed control switches for step speed commands
- (f) Load select switch for 1-minute 85 hp load
- (g) Opto-isolated monitors for the 400-Hz output and permanent-magnet generator (PMG) input
- (h) Opto-isolated monitors for PMM operating frequency measurements
- (i) PMG protection circuitry for overtemperature sensing
- (j) First-event memory readout for motor-controller-induced faults and PMG overtemperature
- (k) PMG disconnect trip signal for PMG or motor controller faults
- (l) System simulator

The WFWV PMG current unbalance protection could not be used, because the current transformers (CT) associated with the PMG are ac only. The output



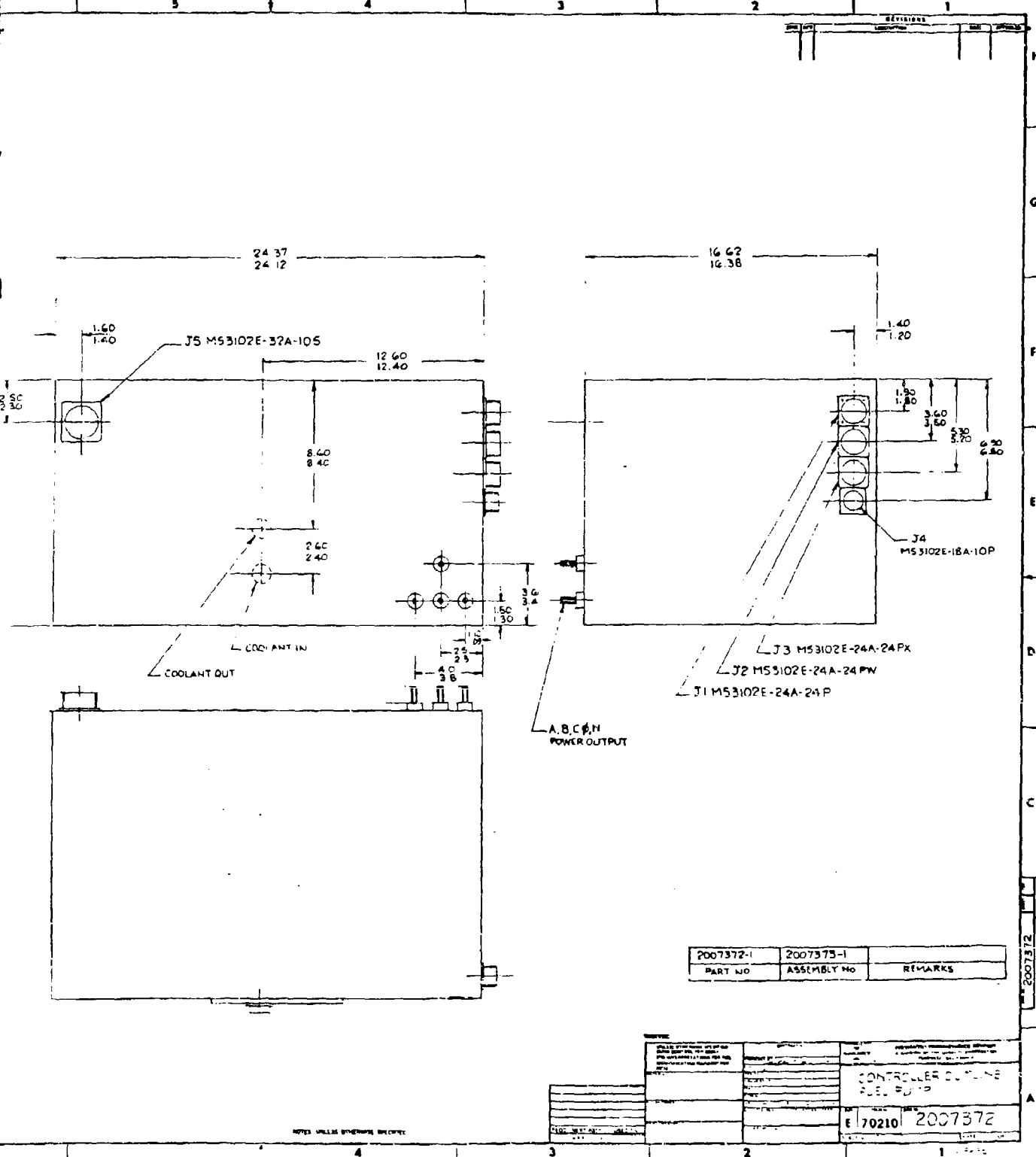


Figure 4-15. Motor Controller Outline

current wave form from the PMG is basically half-wave rectified and hence contains only positive currents of 120-degree duration. The PMG current transformers do not contain an air gap and thus saturate and do not provide a proportional (secondary) output. The General-Electric-recommended 50-ohm burden resistor was used across each CT for transient protection. PMG current limit protection was provided by current sensing within the motor controller, with backup consisting of an input fuse for each of the nine PMG phases.

A system simulator was included as an integral part of the control panel. The simulator is a very effective special test circuit which allows nearly all of the logic functions to be dynamically operated or tested without actually processing power through the motor controller. The simulator circuitry models the 400-Hz and PMG source inputs and the motor controller PMM output so as to enable "closed loop" testing of the controller logic and thyristor gate drive circuitry.

The control panel was considered as special test equipment and therefore was designed for installation into a standard 19-inch relay rack cabinet. The display functions of the panel are shown in Figure 4-16.

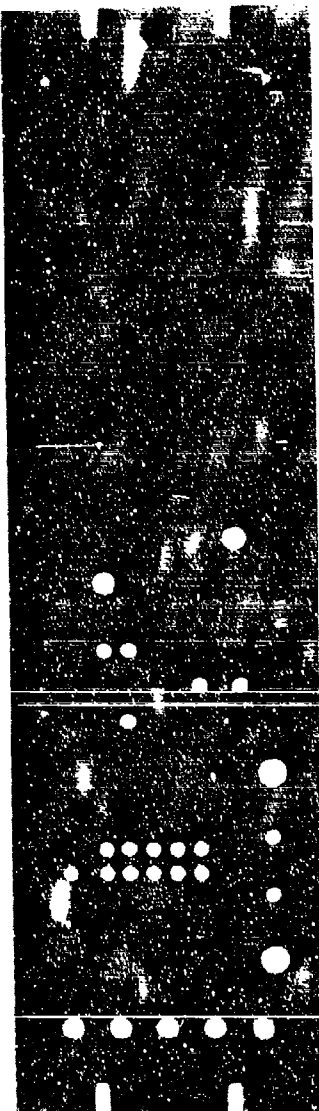
#### 4.3.2 Motor Controller Bench Testing

Before initiating system testing, the motor controller was bench-tested to demonstrate satisfactory compliance at both subassembly and final assembly levels. Bench testing included, but was not limited to, the following:

- (a) Incoming inspection of critical components, such as power semiconductors, transformers, inductors, heat sinks, and logic integrated circuits.
- (b) Printed wiring assembly (PWA) calibration and performance verification using standard PWA test fixtures and auxiliary wave form generators and power supplies.
- (c) Continuity check of control logic chassis and other motor controller module subassemblies as well as the final controller wiring.
- (d) Dielectric and insulation resistance check of the motor controller final assembly.
- (e) Current and voltage sensor calibration verification.
- (f) Logic and thyristor gate power supply functional check.
- (g) Interface with control panel command signals and annunciation.
- (h) Inverter operation from 400-Hz power sources using test setup shown in Figure 4-17. Specific operational tests included on/off control

90211-3

Figure 4-16. Control Panel Functions



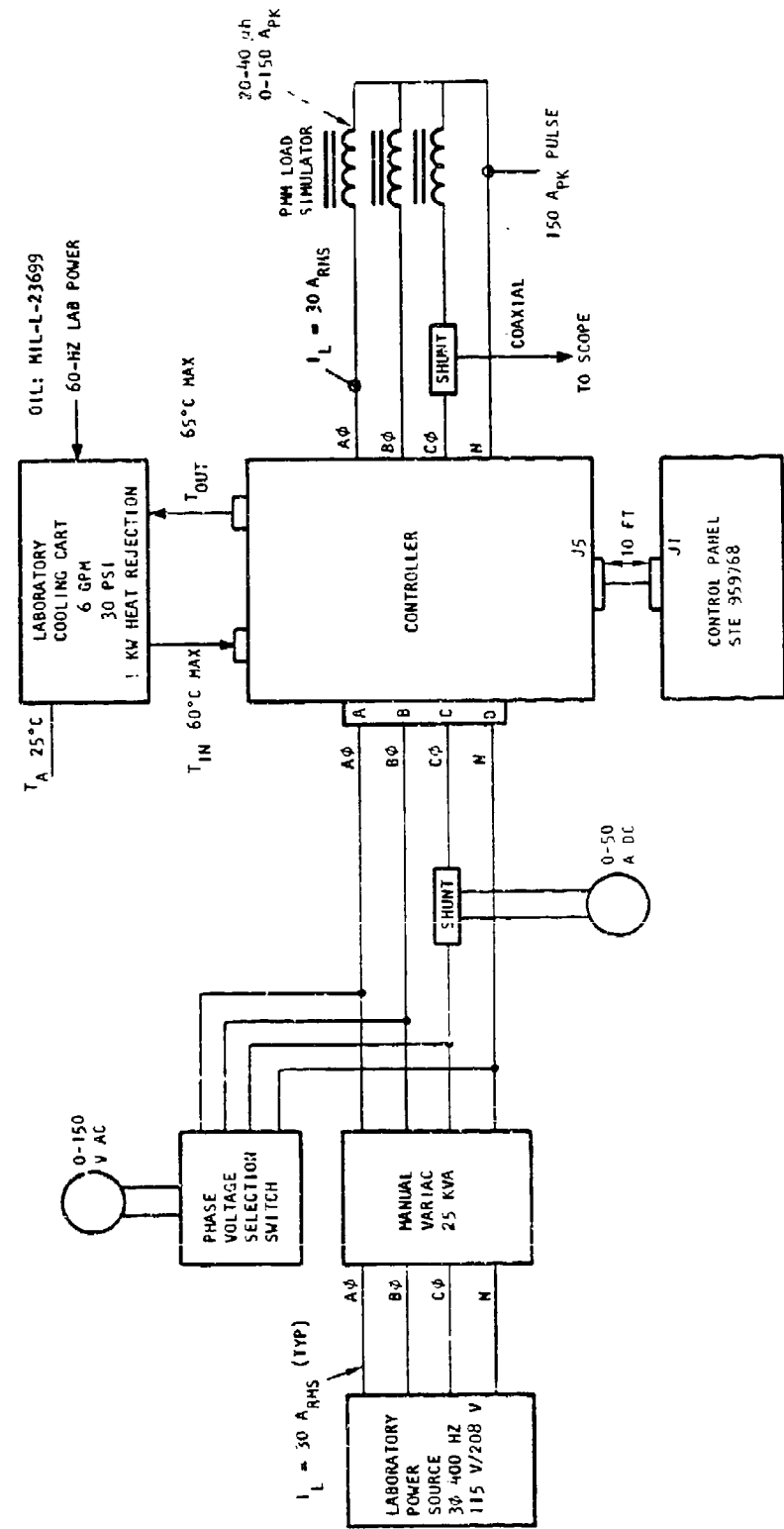


Figure 4-17. Motor Controller 400-Hz Bench Test Setup

of the 400-Hz power within the motor controller, rectification and control of the 400-Hz power, and operation of the PMM inverter to produce regulated current to the load inductors, including commutation of the inverter thyristors.

Considerable difficulty was encountered during the motor controller bench-testing phase associated with the following four areas:

- (a) Control-panel-simulator-to-controller-logic interface required modification to correct system scaling factors and operational modes within the simulator.
- (b) Motor controller power supply required redesign due to inadequate cooling when mounted within the controller.
- (c) Motor controller logic associated with PMM startup and the commutation of the PMM inverter thyristors had to be redesigned.
- (d) Dielectric breakdown between the commutation semiconductors and their associated heat sink required removal, repair, and replacement.

## 5. MOTOR TESTING

The test activity was planned to concentrate on the motor. The benefits of characterizing the motor are that the motor controller and pump performance can be ascertained in system testing if the motor performance parameters are accurately established at the component level.

During system testing, it is difficult to obtain data at the motor input due to the nonsinusoidal nature of the voltage and current wave forms. The motor output shaft power is also a problem to measure because the insertion of any instrumentation impacts the motor and pump performance. The electrical input and hydraulic output of the system can be readily measured, and if the motor characteristics are properly defined, the control and pump efficiencies can be established with reasonable accuracy.

### 5.1 MOTOR LOSS BREAKDOWN

The test concept used the "coastdown" method of loss separation. The inertia of the rotating assembly was measured, and the motor rotor was driven to slightly over rated speed and then allowed to decelerate with no driving torque. The rate of deceleration is a measure of the motor loss causing the motor to slow down. The data presented are based on the results from the 5-mil silicon-steel laminated stack configuration. Other tests were performed to try to optimize motor efficiency using the nickel-steel laminations and an unskewed stator stack. The results of these tests indicated that they would provide no significant efficiency benefits. Because these configurations all would cause some negative impact on the system, the conventional silicon-steel laminations were chosen for system testing. The basic configurations used in the motor loss analysis are listed below.

- (a) A dummy (nonmagnetic) rotor of known inertia with the same shape as the active motor rotor was used to establish windage and friction losses.
- (b) A magnetized rotor was tested in a motor with an unwound stack to measure iron and stray field losses.
- (c) The same configuration as above was tested, except that the stator was wound to provide stator copper stray and circulating current losses.
- (d) An ac resistive load was applied to verify the current-related copper losses and establish the resistance of the magnets to armature reaction demagnetizing fields.
- (e) A rectified dc load was applied in an unsuccessful attempt to ascertain the harmonic losses. The commutating inductance was measured during this test.

The windage and friction losses were measured with the bearings lubricated with oil mist. The loss was a function of the square of the rotor speed, with a value of 463 W at 45,000 rpm.

The motor losses with the magnetic rotor are given in Figure 5-1, which includes the windage and friction measurement using the nonmagnetic dummy rotor. The difference between the two curves represents the iron and stray flux field and tooth ripple rotor losses. Repeating this test with the stator winding in place provided an additional loss of 170 W at 45,000 rpm. This stator copper flux-related and circulating current loss is a function of the square of the speed.

Test data were taken at approximately 70°F and 250°F ambients to establish the effect of magnetic field reduction at the elevated temperature. The average of a number of coastdown runs was taken at each test condition to minimize any effect of data scatter. Figure 5-2 shows the results of the series of 12 runs to establish the iron and stray loss data. The maximum deviation from average was +3.5 percent to -5.9 percent. This deviation is insignificant when the power being measured is the major motor loading factor. The deviations make loss separation impractical when the loss under investigation is only a few percent of the total motor power. Attempts were made to establish loss effects with ac resistive loads and rectified dc loads to better define harmonic loss effects and separate stator and rotor losses, but data scatter made accuracy questionable.

Table 5-1 lists the main parameter measurements at 45,000 rpm and compares them with the calculated values.

## 5.2 MOTOR VOLTAGE AND INDUCTANCE

During the loss evaluation testing described above, the voltage constant and commutating inductance were measured. The agreement between the measured and calculated values is quite good. The technique used to establish the commutating inductance evaluated the commutation event at a specific load condition by measuring the driving voltage, the current change, and time period to achieve zero current. The commutating inductance is then calculated by  $L = e_{avg} (\Delta t / \Delta i)$ . Test results are included in Table 5-1.

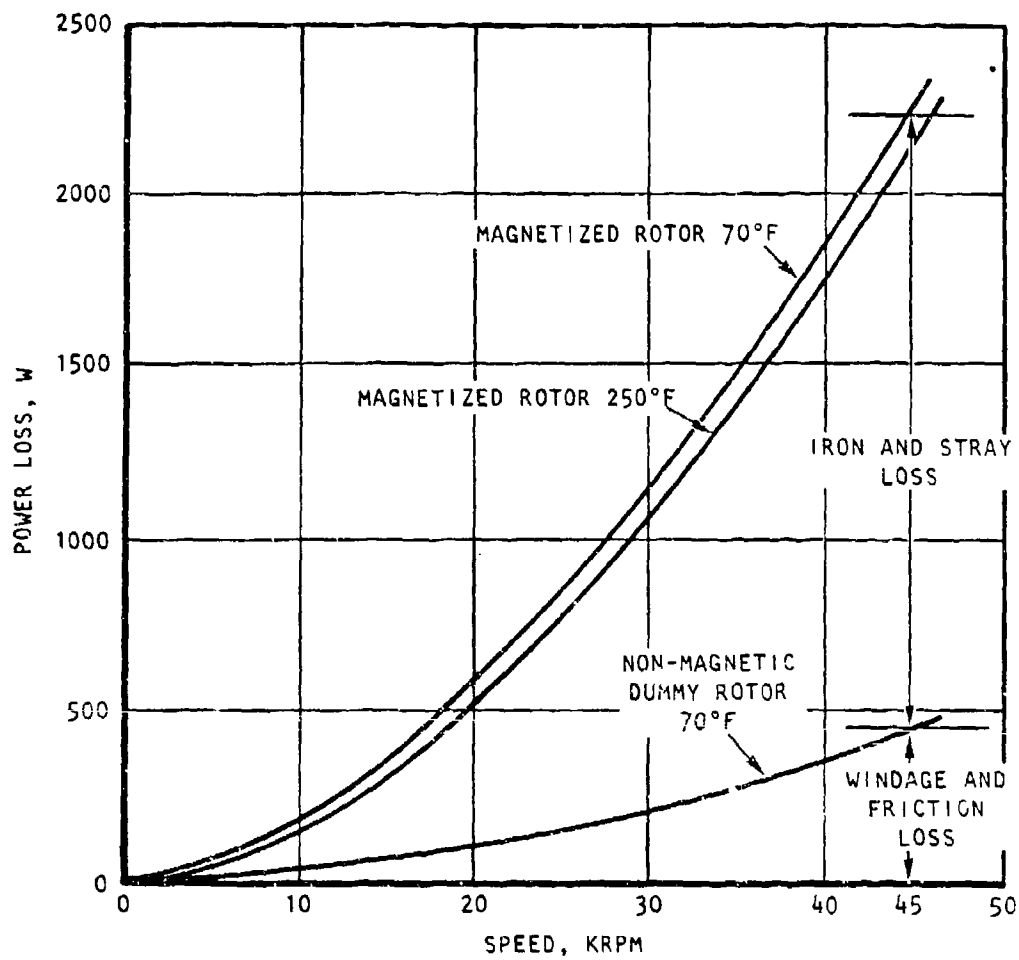


Figure 5-1. No-Load Coastdown Test Results for 0.005-in.  
Silicon-Steel Stator Laminations

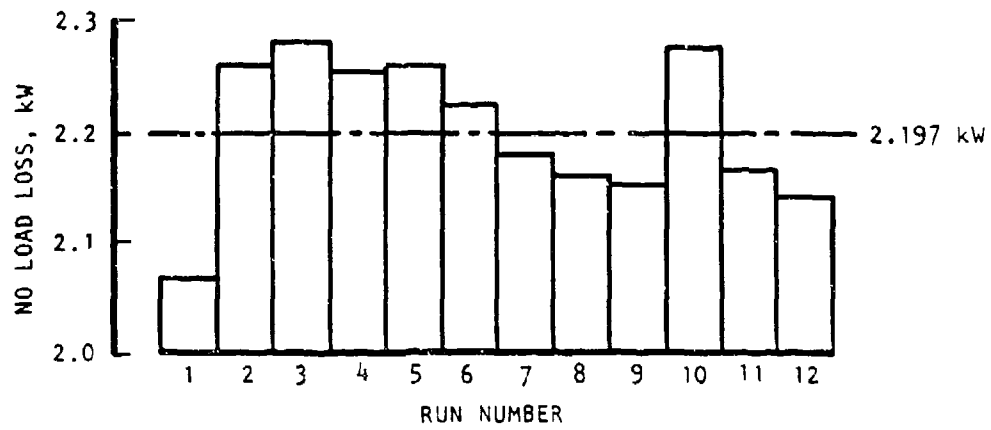


Figure 5-2. Variation of Loss Measurement at 45,000 rpm and 70°F with Magnetized Rotor and Silicon Steel Stack

TABLE 5-1. Comparison of Calculated and Measured Parameters

Parameter	Units	Calculated	Measured
Voltage L-N (at 45,000 rpm)	volts ac	184.1	190.0
Commutating inductance	$\mu$ h	24	22
Windage and friction	watts	455	463
Iron and stray field loss	watts	1335	1737
Flux-related copper loss	watts	0	170
Winding resistance line to line at 20°C (including leads)	ohms	0.0224	0.0285

## 6. SYSTEM TESTING

### 6.1 TEST CONCEPT

The purpose of the program was to prove the viability of electrical motor drives, at relatively high power levels, controlled electronically over a wide speed range. The program was set up to couple this primary demonstration with the use of a high-speed, permanent-magnet, high-frequency generator to provide motor controller input power at the high-speed end of the performance range and use 115/200-V, 400-Hz power for the low-speed startup mode. Development testing was conducted using this dual input power concept. Just prior to entering the high-power development testing, the high-frequency 9-phase generator suffered an internal seal leak which permitted oil to enter the generator air gap. This resulted in excessive heating of the generator.

The failure of this oil seal precluded the use of the 9-phase generator and the 9-phase power control and conversion sections of the motor controller. To provide the maximum performance data within the remaining program time, AiResearch offered the use of a motor controller with similar characteristics that had been developed for the Gas Research Institute (GRI) to operate from a 3-phase, 480-V, 60-Hz source. To conduct the performance tests, the GRI dual inverter was paralleled with the dual converter section of the fuel pump control comprising the 400-Hz half-wave rectifier and 3-phase full-wave inverter.

The change in approach can be seen by comparing the test setup block diagrams. Figure 6-1 shows the original plan from the approved test procedure. The agreed-upon alternate approach is shown in Figure 6-2. A simplified block diagram of the "as conceived" fuel pump drive is given in Figure 6-3, and a simplified schematic of the actual test control configuration is shown in Figure 6-4.

Startup of the motor is identical to the original plan, using the 400-Hz source coupled with the inverter. When the motor backvoltage reached a high enough value, the second inverter was paralleled with the startup inverter and the startup inverter shut down. All testing at speeds in excess of 15,000 rpm used the dual converter operating from the 3-phase, 60-Hz input.

From an electrical and mechanical standpoint, the substitute inverter is identical to the inverter as originally conceived for the pump drive. The thyristors used in the inverter and front-end converter are identical, and the oil cooling and assembly is very similar to that of the original concept. With such a replacement system available, the measurements associated with efficiency and electrical characteristics are identical to those that could have been obtained from the original concept.

The modified plan was to measure performance at the conditions noted below:

- a. Low flow valve setting at 10,000 rpm
- b. Low flow valve setting at 15,000 rpm

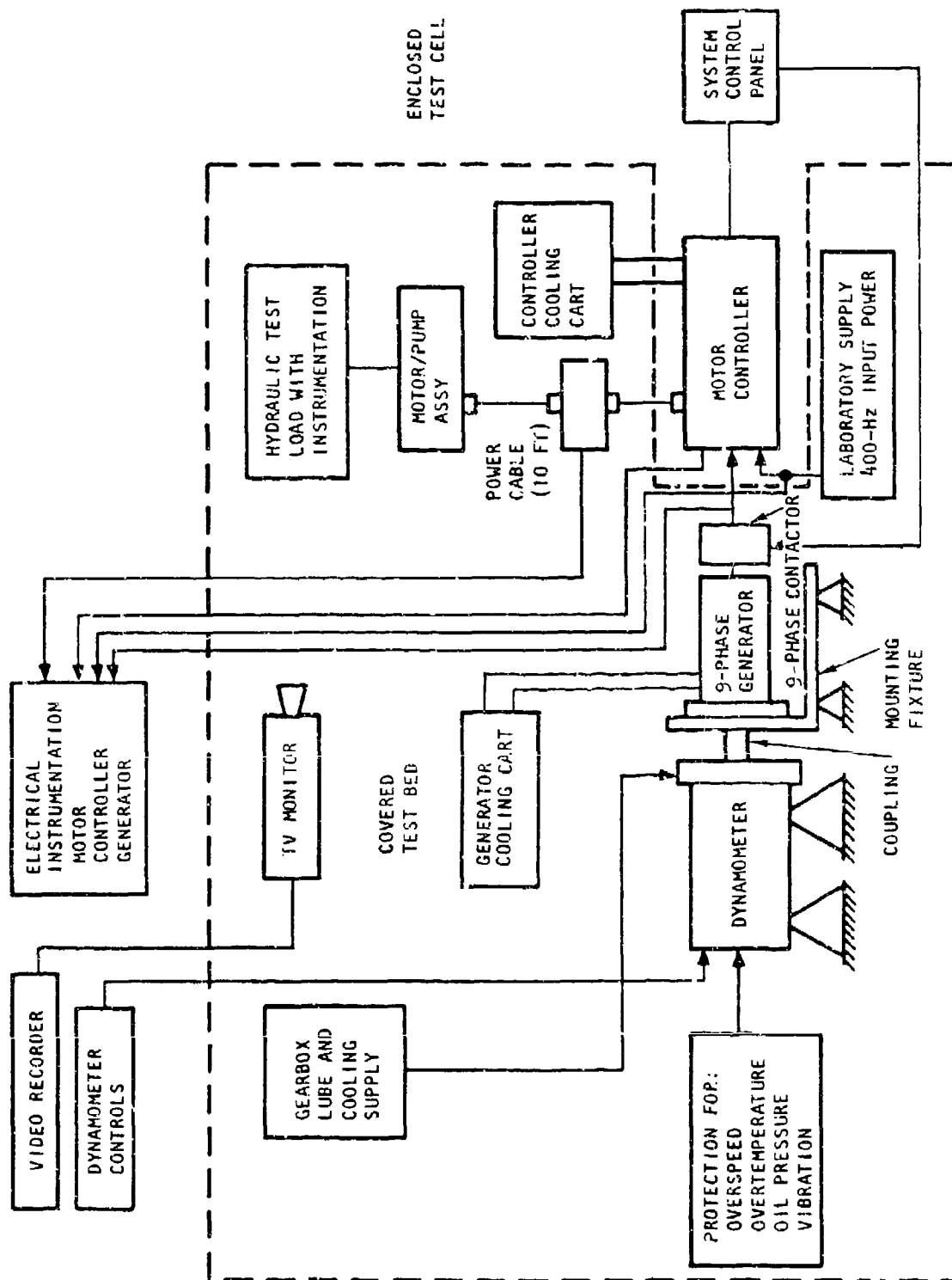


Figure 6-1. Original Plan Overall Test Setup Block Diagram

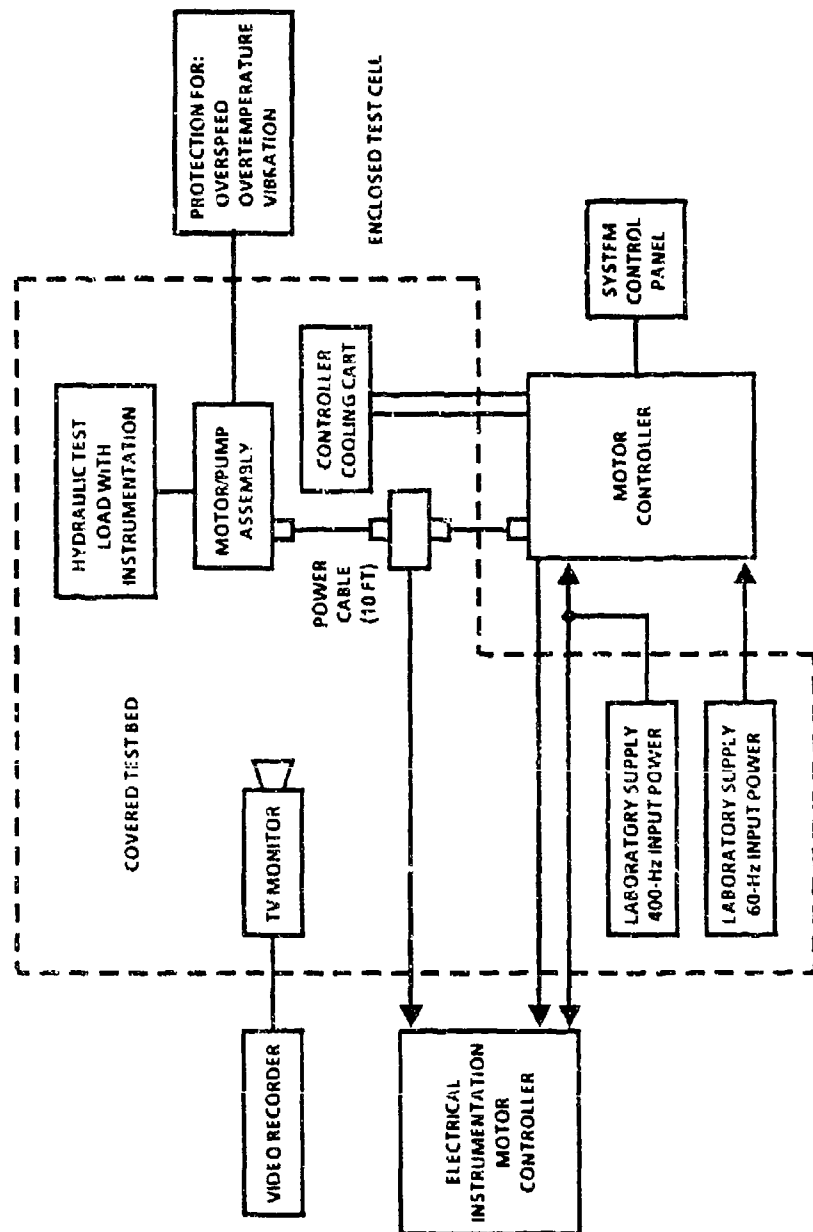


Figure 6-2. Final Overall Test Setup Block Diagram

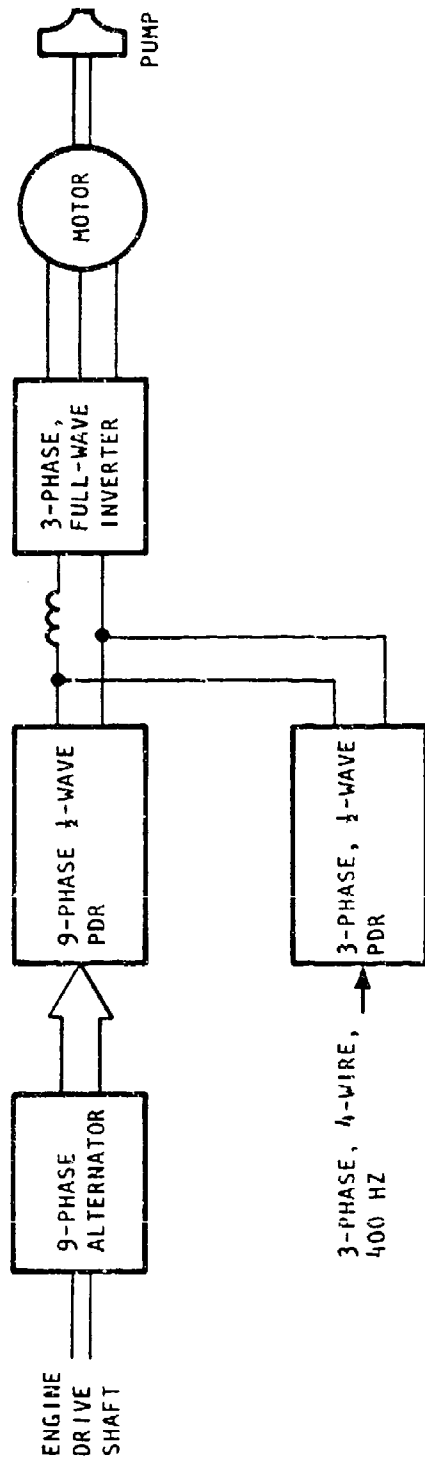


Figure 6-3. Basic Block Diagram of Fuel Pump Drive as Originally Conceived

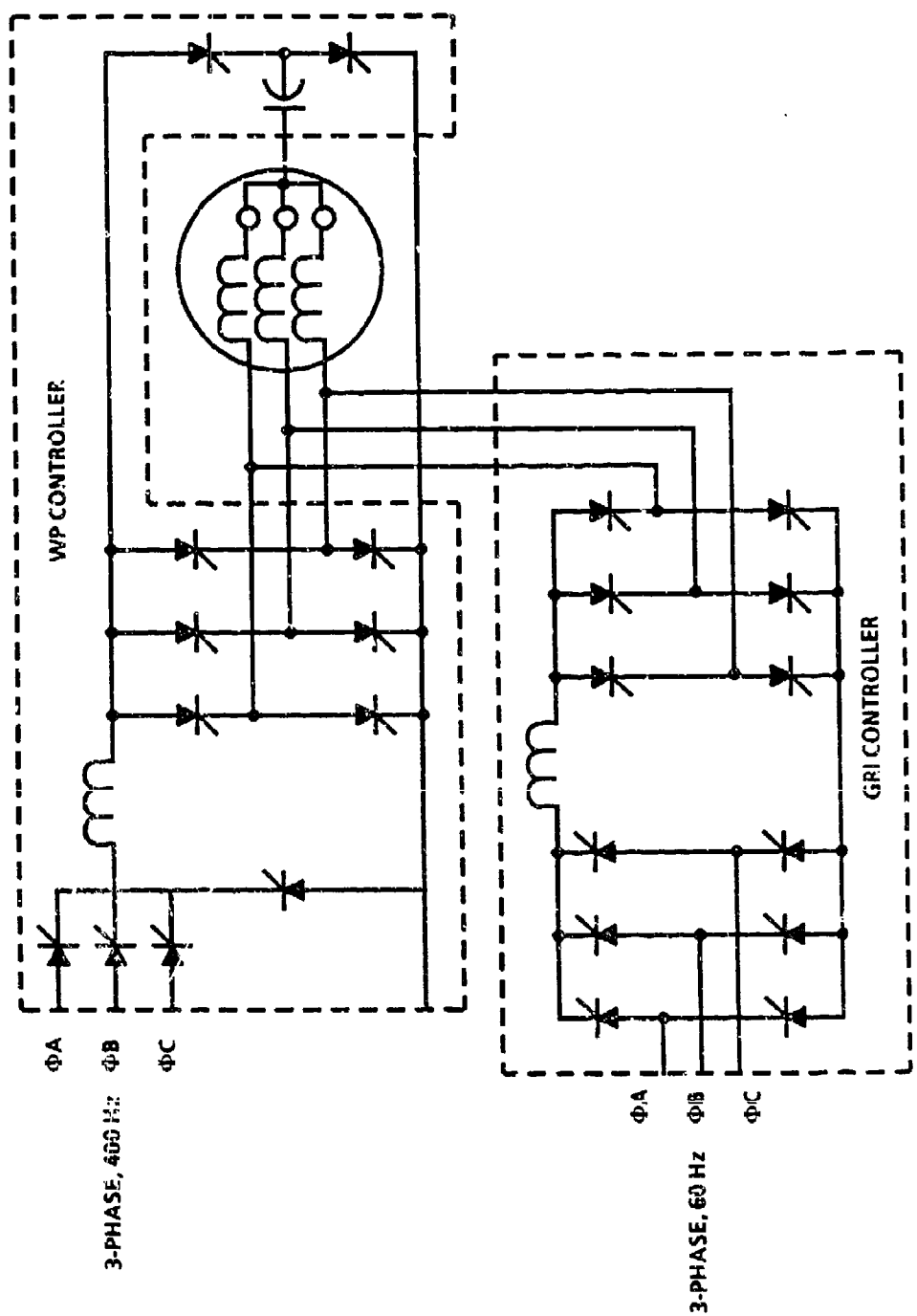


Figure 6-4. Basic Schematic for Using GRI Controller for Electric Fuel Pump Drive Demonstration

- c. Low flow valve setting at 24,000 rpm
- d. Low flow valve setting at 40,000 rpm
- e. Low flow valve setting at 45,000 rpm
- f. Low flow valve setting step command 15,000 to 24,000 rpm
- g. Low flow valve setting step command 24,000 to 15,000 rpm
- h. Low flow valve setting step command 24,000 to 40,000 rpm
- i. Low flow valve setting step command 40,000 to 24,000 rpm
- j. High flow valve setting at 45,000 rpm
- k. Low flow to high flow step command at 45,000 rpm
- l. High flow to low flow step command at 45,000 rpm

Testing was conducted with the pump impeller slightly over the diameter required to produce rated power at 45,000 rpm when operating with MIL-H-83282 oil. The 40,000-rpm test point was added to provide an equivalent rated load demonstration.

Test data was successfully recorded at test conditions (a) through (i), which represent all the low-flow operating conditions. Two problems developed that limited the planned operations at the high-flow mode.

During testing, the commutation of the inverter was continuously monitored to ensure that the inverter was not operated beyond its commutation limit. This limit precluded operating at the full design power of 85 hp. The firing angle was adjusted to attempt to achieve a higher electrical power throughput across the inverter. However, by decreasing the phase advance angle, the dc link voltage is reduced and current needed is increased, reducing the turnoff time available in the individual thyristors. With a minimum turnoff time of 20  $\mu$ sec, the maximum electrical power of 57 kW was achieved. Because the system encountered a commutation angle limit at approximately 37,000 rpm and 70 hp, data is presented for this test point and two lower-speed points at the high-flow valve load setting.

The second problem pertained to the test setup. The solenoid valve was unable to perform the required step command flow change. Rather than procure a new valve and replumb the hydraulic test setup, with a resulting delay in program completion, AiResearch felt that this test should be eliminated.

Considering the commutation limitation, the speed would have to have an initial setting below 37,000 rpm, which limits the power change significantly. Also, the transient current on step command up to the close commutation limit could result in damage to the hardware.

The fully instrumented motor and pump assembly are shown in the test setup in Figure 6-5. Figure 6-6 is a schematic of the test setup with the key instrumentation and control valve features highlighted.

## 6.2 TEST RESULTS

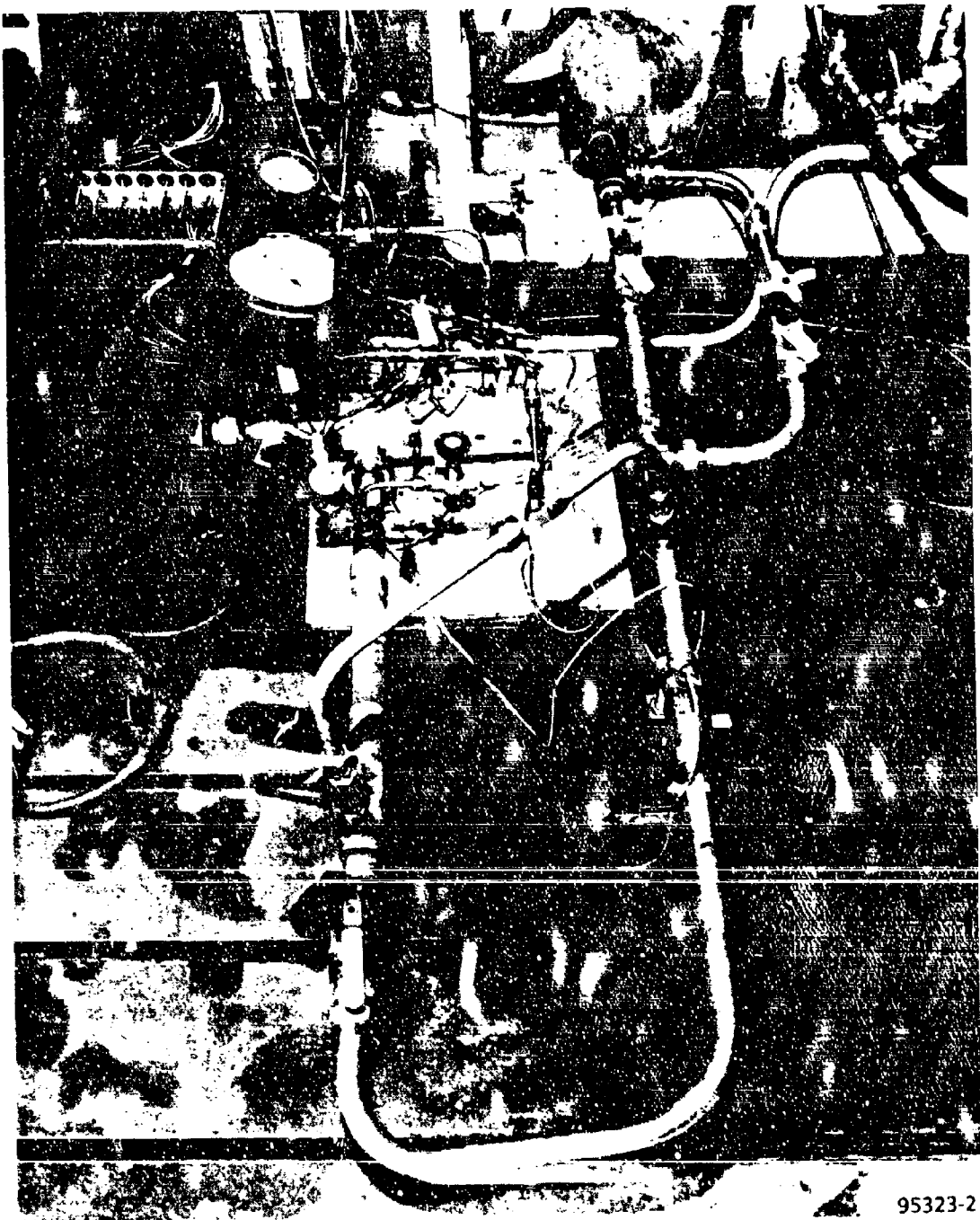
Data were taken at eight load conditions. Five were with the loading valves in the low-flow position, and three were with the valves reset to the high-flow position. Table 6-1 sets this information out and gives the motor/pump exact speed for each of the test points. All other data tables relate to these same speed and valve conditions by referencing test points 1 through 8.

TABLE 6-1. Motor Pump Test Conditions

Flow Valve Setting	Test Point	Motor Speed, rpm
Low flow	1	10,158
	2	15,009
	3	24,189
	4	40,740
	5	45,168
High flow	6	24,399
	7	35,133
	8	37,080

The electrical input power at the dc link was recorded and the hydraulic output power of the pump was recorded to define accurately the system output. Power levels at other points in the system were determined from either loss breakdown test data determined by earlier component level testing, or from calculations based on known characteristics of the parameters involved. To verify the overall accuracy of this approach, a power balance accounting was made to see if there was any significant discrepancy at any of the test points.

Table 6-2 shows the input volts, amps, and watts at the dc link. The inverter loss was calculated based on the characteristic of the thyristors. This is a constant, representing the forward voltage drop times the current. Where an empirical calculation of this type is used, the column in the table is shaded. Where a calculation uses only measured parameters to obtain the value, no shading is used. An example is the line loss column in Figure 6-2, which is a product of the measured line resistance and the measured current. The efficiency of the inverter, including the line drop between the motor controller and the motor, is then determined. Not included here are the losses associated with phase-delay rectification and filtering at the input of the motor controller. The 480-V, 60-Hz motor controller used is not directly pertinent to the program in that the switching frequency and filtering requirements differ substantially.



95323-2

Figure 6-5. Motor and Pump in Test

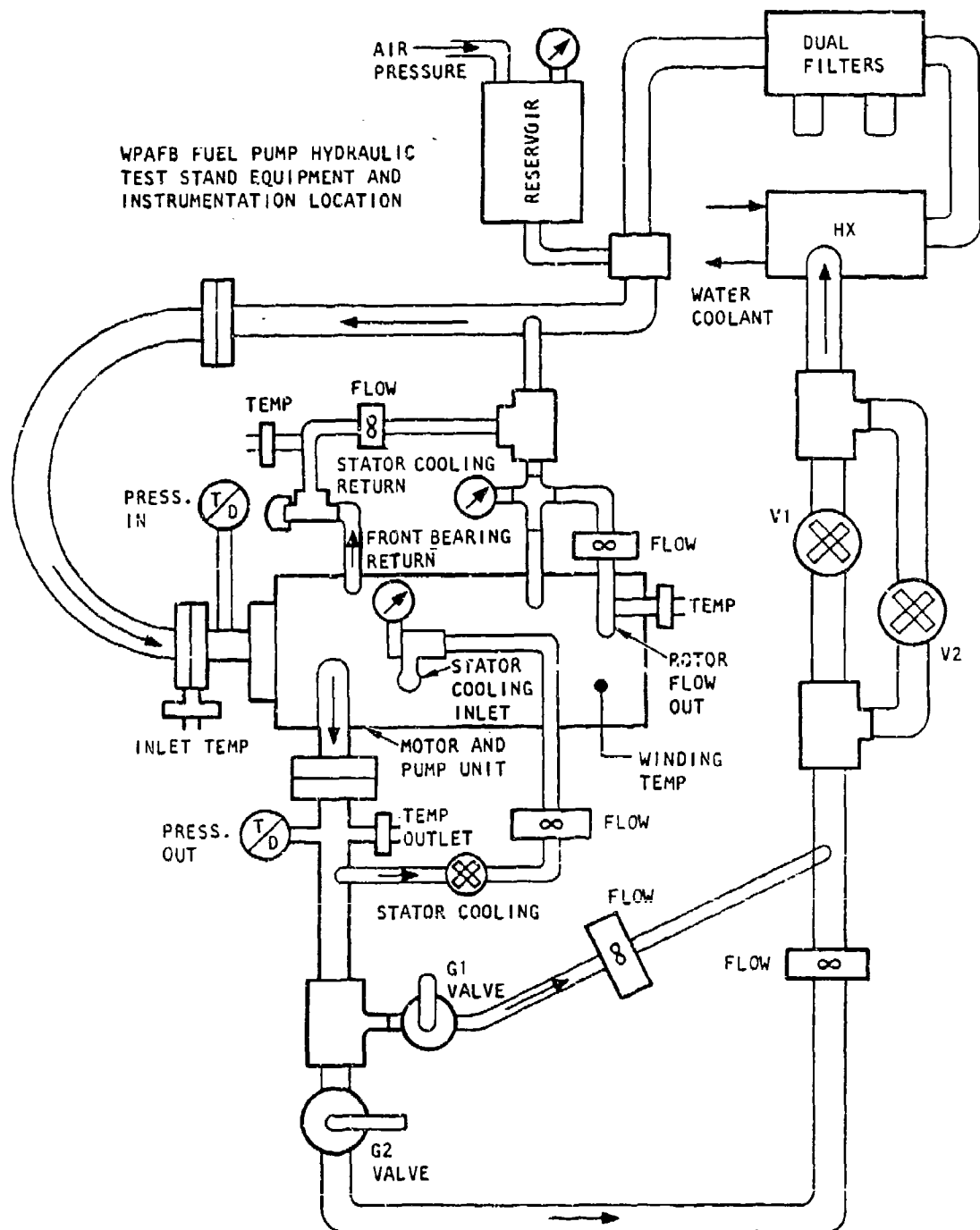


Figure 6-6. Schematic of Motor and Pump Test Setup

TABLE 6-2. Inverter Power and Efficiency

Test Point	Power Input, dc Link			Inverter Loss		Inverter Efficiency, percent
	vdc	adc	W	Inverter, W	Line, W	
1	67.6	18.0	1,217	81	3	93.1
2	117.1	28.6	3,349	129	8	95.9
3	189.6	58.8	11,148	265	35	97.3
4	331.1	120.8	39,997	544	146	98.3
5	374.9	137.0	51,361	617	188	98.4
6	177.2	99.8	17,685	449	100	96.9
7	262.3	181.7	47,660	818	330	97.6
8	284.0	200.7	56,998	900	400	97.7

Table 6-3 covers the the determination of the motor losses and efficiency. The motor power output is determined by subtracting the motor losses from the motor power input. The motor losses were established as follows. The copper losses were calculated using the measured resistance of the motor winding line-to-line, the dc link current, and the copper resistivity factor for the winding temperature at the time the data were taken. The iron loss and the windage and friction loss are the motor loss values established as a function of speed from the component motor level coastdown tests. The "stray watts" column is an empirical value. This is an extremely difficult value to determine in that it must consider stray magnetic flux fields from the permanent magnet operating in the motor armature reaction field. This problem is coupled with the harmonic loss effects in the rotor surface due to the nonsinusoidal wave form of the inverter drive. Experience from similar systems has indicated that a loss of approximately three percent

TABLE 6-3. Motor Losses and Efficiency

Test Point	Motor Input, W	Motor Losses				Motor Output, W	Motor Efficiency, percent
		I <sup>2</sup> R, W	Iron, W	W&F, W	Stray, W		
1	1,133	9	150	28	34	912	80.5
2	3,212	24	283	59	96	2,750	85.6
3	10,848	105	613	144	325	9,661	89.1
4	39,307	497	1427	384	1179	35,820	91.1
5	50,556	599	1687	466	1517	46,287	91.6
6	17,136	323	622	146	514	15,531	90.6
7	46,512	1139	1123	291	1395	42,564	91.5
8	55,698	1378	1225	327	1671	51,097	91.7

of the power input should be expected; therefore, this value was used here. The motor efficiencies determined are in the low 90-percent region at the higher loads, which is in the area calculated for this type of motor.

Table 6-4 presents the motor performance parameters in a different form. The motor output is converted to horsepower, and shaft torque is calculated for each test point. The torque constant in the units of in-lb per dc link amp is then calculated. An interesting change occurred in the torque per amp between the low-flow and high-flow test conditions. A partial explanation is that the higher armature reaction fields at the high-flow, high-current tests caused the stator winding flux linkage to decrease, thus dropping the torque per amp. Test points 3 and 6 are at the same motor speed, but the torque per amp at the high-flow load condition is 6.1 percent lower.

TABLE 6-4. Motor Performance

Test Point	Motor Shaft		Torque Constant, in-lb/amp	Motor Internal Drag, hp
	Power, hp	Torque, in-lb		
1	1.22	7.59	0.421	0.25
2	3.69	15.48	0.541	0.56
3	12.95	33.75	0.574	1.44
4	48.02	74.30	0.615	4.10
5	62.05	86.59	0.632	5.04
6	20.82	53.79	0.539	1.47
7	57.06	102.37	0.563	3.05
8	68.49	116.44	0.580	3.38

The final column in Table 6-4 defines a motor loss not previously addressed. This loss is due to two factors which are present in this motor but are not essential to proper operation. Both of these factors are caused by the flooding of the front bearing and rear bearing cavities by cooling oil. The original motor concept called for the use of journal bearings. This was changed because of safety concerns when operating with MIL-C-7024. Both bearings were changed to ABEC-5 angular-contact ball bearings. These bearings represent a significant loss at the higher-speed test points. In addition to the bearings, the position sensor disc, which has two discrete poles, also rotates in the flooded rear bearing cavity. Calculations indicated that approximately 20 percent of this motor internal oil drag loss is attributable to the position sensor. The startup concept was changed during development to a programmed ramp start; therefore, the sensor serves no useful function other than as a spacer on the shaft assembly. These calculated losses were set aside from the motor losses when calculating motor efficiency earlier, because they would be eliminated or greatly reduced on any subsequent motor redesign.

The pump input power considers the net power delivered from the motor; these internal oil drag losses are therefore subtracted before the Table 6-5 data are presented.

TABLE 6-5. Pump Performance

Test Point	Pump Input, hp	Pump Output			Pump Efficiency, percent	Power Oil $\Delta T$ , hp
		Flow, gpm	$\Delta P$ , psi	Power, hp		
1	0.97	9.90	40.0	0.23	23.7	0.16
2	3.13	16.44	98.9	0.95	30.4	1.47
3	11.51	28.08	268.7	4.40	38.2	5.46
4	44.21	45.47	753.0	19.98	45.2	23.43
5	57.01	48.87	897.8	25.60	44.9	29.15
6	19.35	83.63	206.6	10.08	52.1	9.51
7	54.01	117.40	437.1	29.94	55.4	23.93
8	65.11	127.90	479.1	35.75	54.9	29.22

Table 6-5 presents the pump performance. The pump output horsepower is calculated from the measured oil flow and pressure rise. In addition, the pump efficiency is calculated. The power going into heating of the oil is calculated and presented in the final column of the table. The sum of the pump power output and the power going into heating of the oil should approximate the pump input power. This sum will generally fall slightly below the input value because heat is lost from the oil into the surrounding structure, and the thermocouples sensing the oil temperatures are sheathed, thus giving some additional separation from the oil itself. The consideration of the unaccounted power does provide a means of verifying the overall accuracy of the performance analysis.

Table 6-6 presents the unaccounted power and compares it to the total dc link input power. The high-flow test points show an excellent balance with very little percentage deviation. The two high-power performance points in the low-flow mode of operation also show little percentage deviation. However, the low-power points in the low-flow mode do show a significant percentage of unaccounted input power. There are a number of possible reasons for this. As discussed earlier, some inaccuracies exist in the determination of the power lost to oil heating. This could be aggravated at the low-flow conditions and low-temperature-rise measurements. In addition, the accuracy of the measurements at the low volts, amps, flow, and pressure rise may also be a factor.

TABLE 6-6. Power Balance

Test Point	Dc Link, W	Unaccounted Power	
		W	percent
1	1,217	433	35.6
2	3,349	537	16.0
3	11,148	1230	11.0
4	39,997	597	1.5
5	51,361	1686	3.3
6	17,685	(179)	(1.0)
7	47,660	104	0.2
8	56,998	104	0.2

In order to assess the consistency of the hydraulic flow and pressure rise data, a flow constant and a pressure rise constant were calculated for each test point. The flow should vary in proportion to speed, and the pressure rise should vary in proportion to the square of speed. The low-flow and high-flow valve set conditions will result in different constants. Table 6-7 presents these factors. At 10,000 rpm, a part of the deviation appears to relate to the accuracy of the metering at low flow and pressure.

TABLE 6-7. Pump Performance Factors

Test Point	$\frac{\text{Flow} \times 10^4}{\text{rpm}}$	$\frac{\Delta P}{(\text{rpm})^2} \times 10^8$
1	9.75	38.77
2	10.95	43.90
3	11.61	45.92
4	11.16	45.37
5	10.82	44.01
6	34.28	34.71
7	33.42	35.41
8	34.49	34.85

The power balance does provide a sound backing for the loss calculations made during the test data reduction. The empirical values used are substantiated to a reasonable degree. Some misappropriation of power loss may possibly exist between the two main empirical areas of stray loss and motor internal oil drag, but this should be minor in the total power evaluation.

The overall measured efficiency from dc link power input to measured pump power output is given in Table 6-8, and the equations used in the various loss calculations are given in Table 6-9.

TABLE 6-8. Overall Efficiency

Test Point	Dc Link Power, W	Pump Output, W	Overall Efficiency, percent
1	1,217	172	14.1
2	3,349	709	21.2
3	11,148	3,282	29.4
4	39,997	14,905	37.3
5	51,361	19,098	37.2
6	17,685	7,520	42.5
7	47,660	22,335	46.9
8	56,998	26,670	46.8

TABLE 6-9. Loss Calculation Equations

Loss	Equation	Comment
Inverter	$(4.5)(I_{DC})$	4.5 is based on published thyristor characteristics
Line	$(0.01)(I_{DC})^2$	0.01 ohm is the line-to-line cable resistance between control and motor
Motor copper	$(0.0285)(I_{DC})^2(\text{Temp. factor})$	0.0285 ohm is the line-to-line motor resistance
Motor iron	$(1677)(\text{rpm}/45,000)^{1.62}$	1677 W at 45,000 rpm and 1.62 exponent were determined by motor tests
Motor windage and friction	$(463)(\text{rpm}/45,000)^{1.88}$	463 W at 45,000 rpm and 1.88 exponent were determined by motor tests with mist lubricated bearings
Motor stray and harmonic	$(\text{watts in})(0.03)$	Empirical constant
Motor internal pumping	$(3730)(\text{rpm}/45,000)^2$	3730 W calculated (approx.) for 45,000 rpm
Pump output	$(\text{gpm})(\Delta P)/1714$	1714 constant for hp output $\Delta P$ in psi
Pump oil heating	$(0.0236)(\Delta T)(\text{gpm})(C_p)(\rho)$	0.0236 constant for hp. $\Delta T$ in °F. $C_p$ is specific heat and $\rho$ is fluid density at operating temperature. See Figure 6-7 for properties.

Figures 6-8 through 6-30 show various wave forms and data recorded on a Tektronix digitizing oscilloscope. Dc link volts and amps and the line-to-line voltages were recorded at most of the key test points. The increase of the commutation time and its effect on the motor backvoltage sine wave can be followed as the load and speed increase. Some dc drift occurred during the recording of this data, but the oscilloscope data agree fairly closely with the digistrip and backup meter readings that were used in the data reduction presented in Tables 6-1 through 6-9. The dc link data also depicts the ripple level seen due to the difficulty in dealing with the low 60-Hz input instead of the 2125 Hz that would have been available from the 9-phase generator.

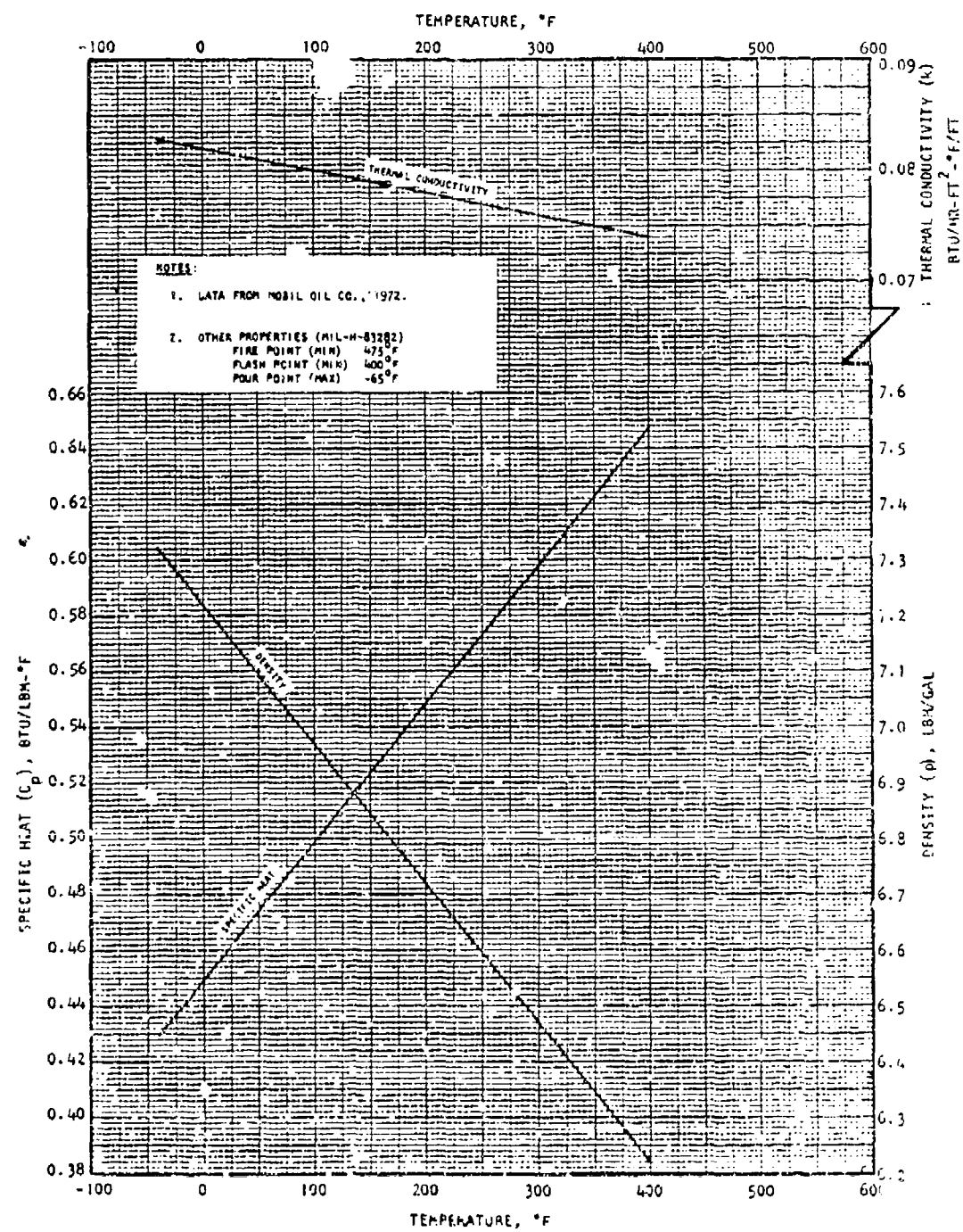


Figure 6-7. Typical Properties of MIL-H-83282 Fire-Resistant Hydraulic Fluid

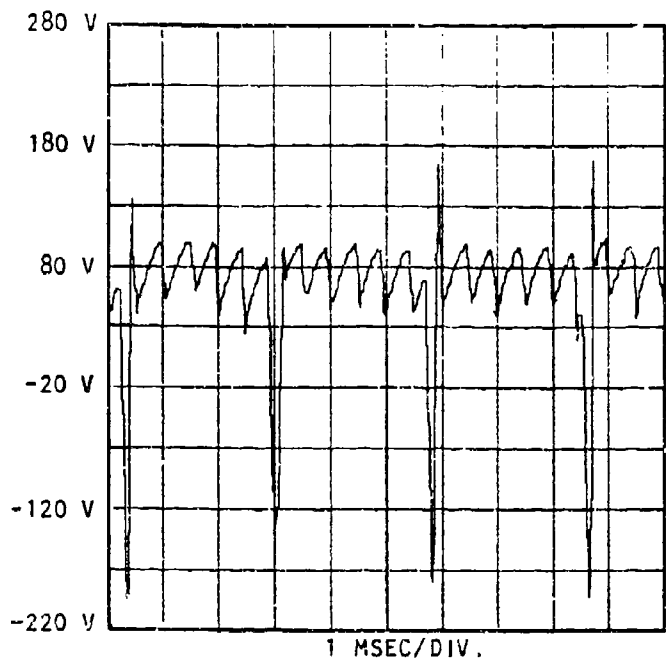


Figure 6-8. Dc Link Voltage, 1.22 hp, 10,158 rpm

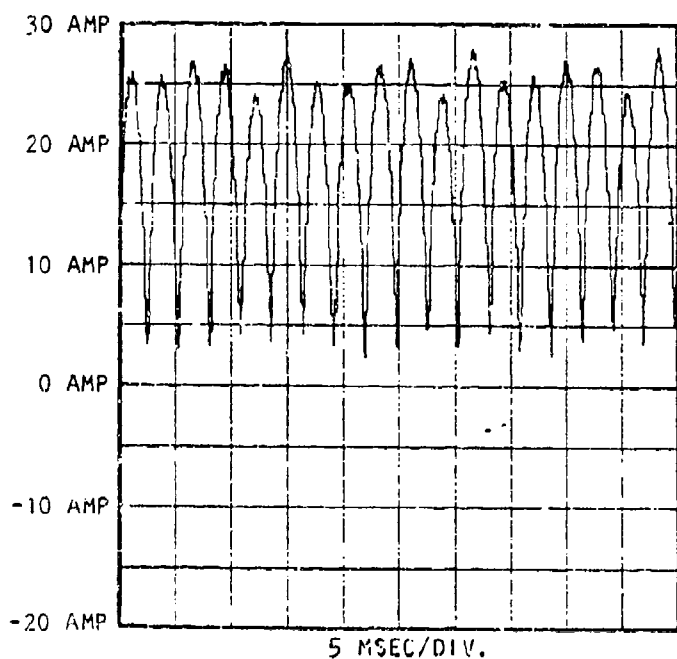


Figure 6-9. Dc Link Current, 1.22 hp, 10,158 rpm

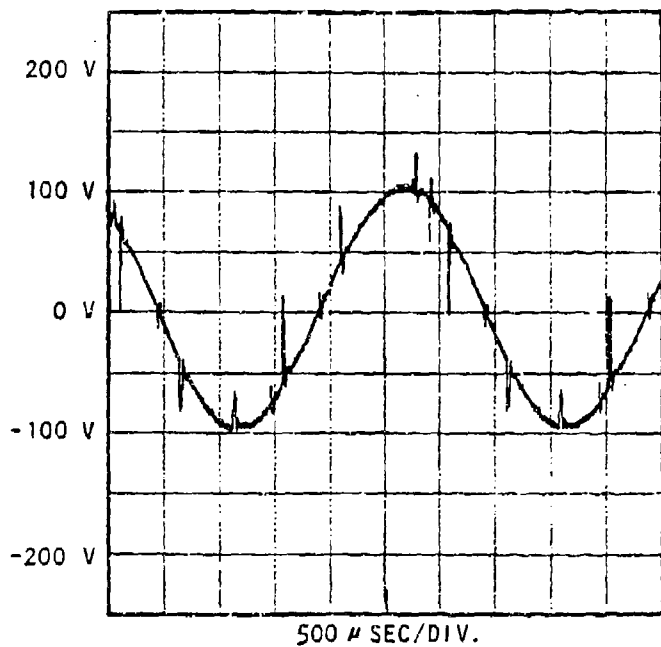


Figure 6-10. Line-to-Line Motor Voltage, 1.22 hp, 10,158 rpm

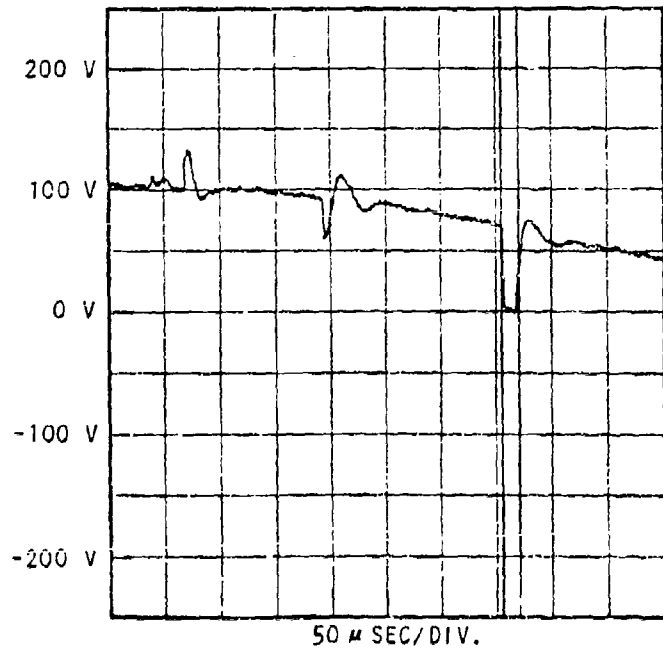


Figure 6-11. Line-to-Line Motor Voltage, 1.22 hp, 10,158 rpm--  
Expanded Time Scale

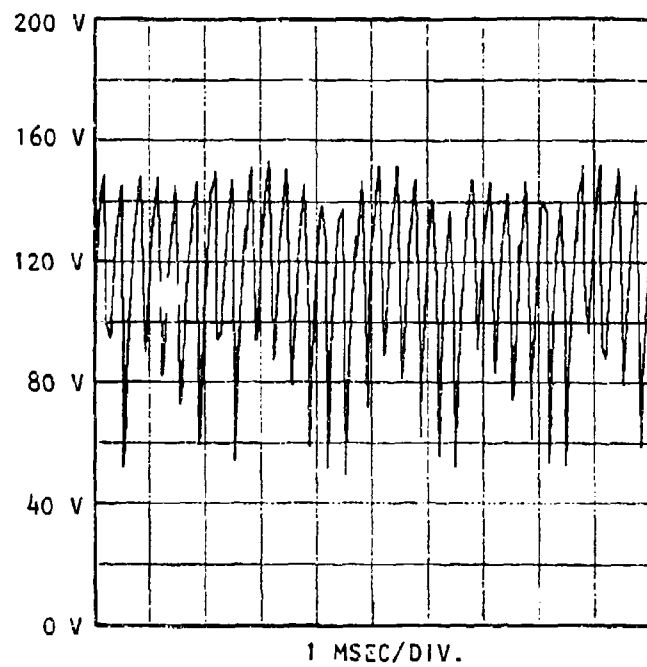


Figure 6-12. Dc Link Voltage, 3.69 hp, 15,009 rpm

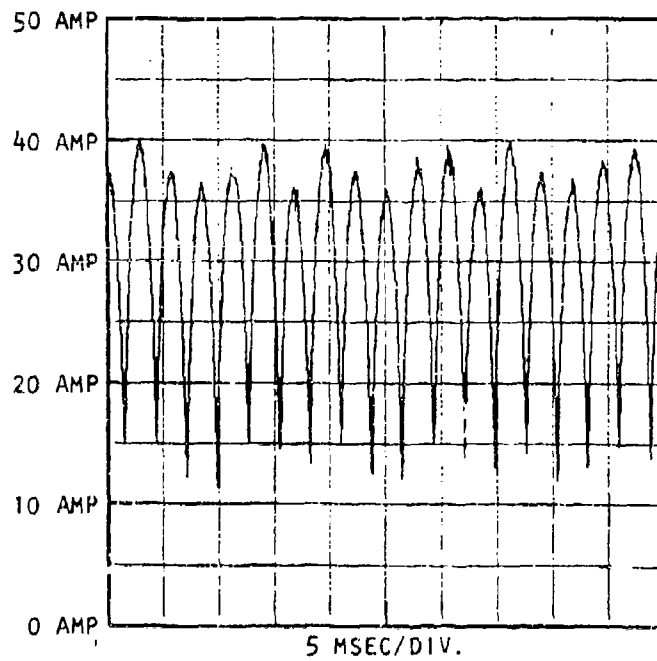


Figure 6-13. Dc Link Current, 3.69 hp, 15,009 rpm

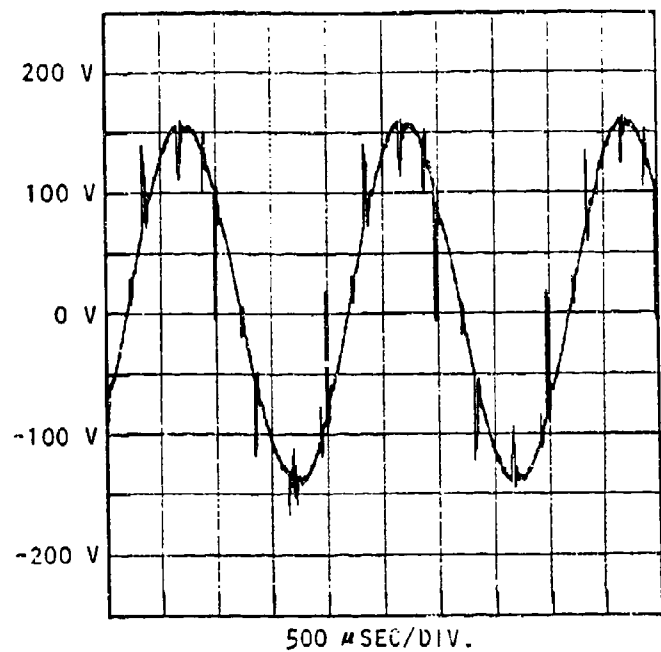


Figure 6-14. Line-to-Line Motor Voltage, 3.69 hp, 15,009 rpm

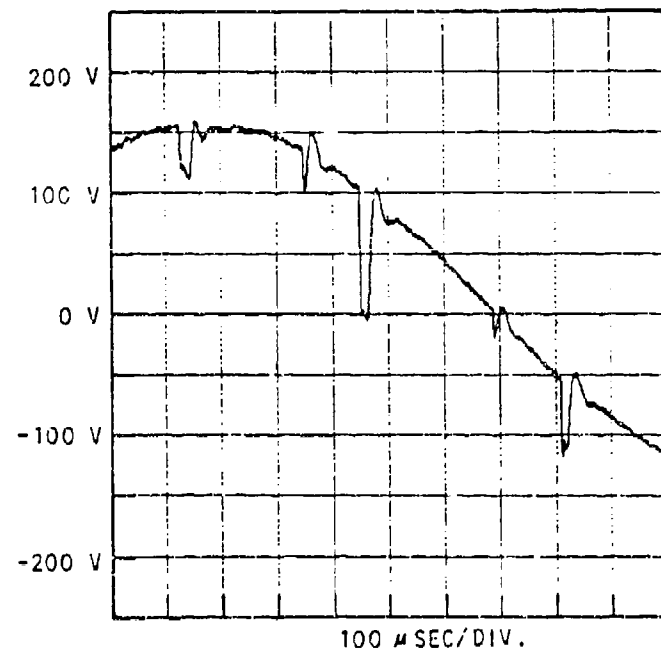


Figure 6-15. Line-to-Line Motor Voltage, 3.69 hp, 15,009 rpm --  
Expanded Time Scale

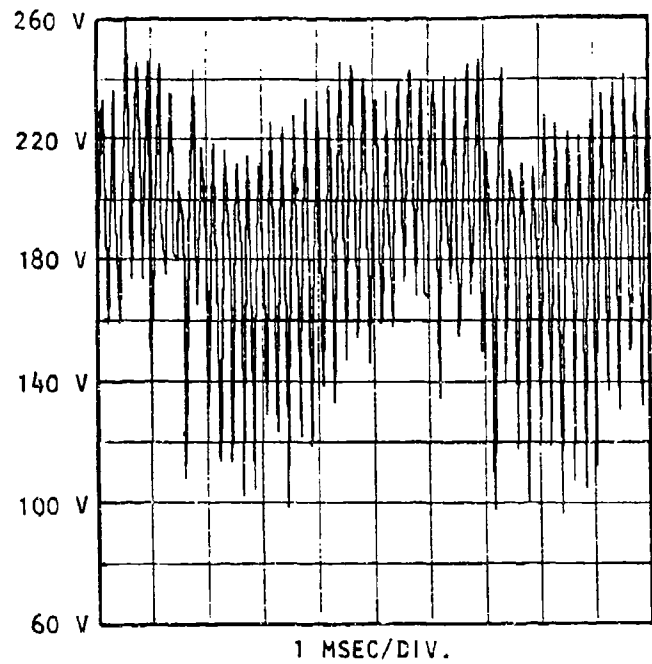


Figure 6-16. Dc Link Voltage, 12.95 hp, 24,189 rpm

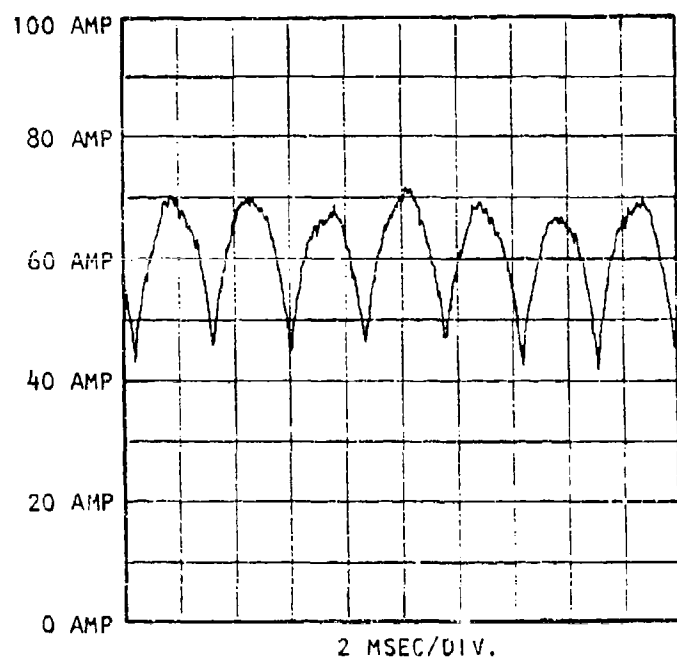


Figure 6-17. Dc Link Current, 12.95 hp, 24,189 rpm

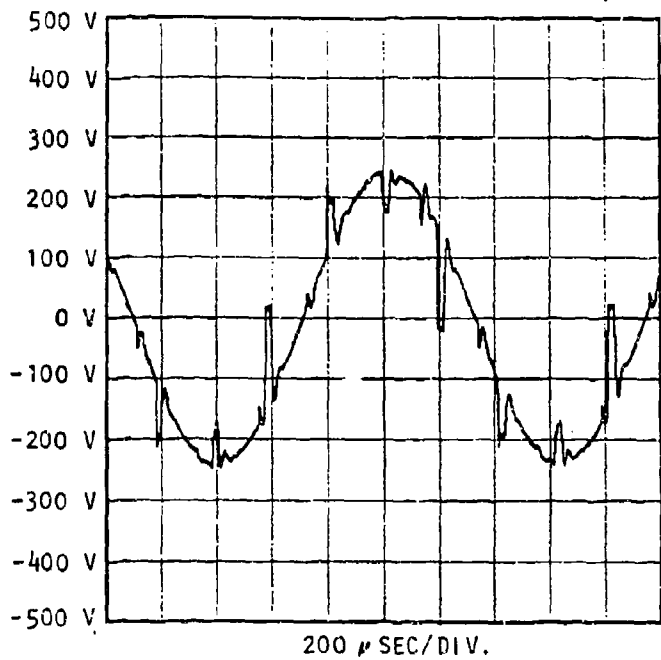


Figure 6-18. Line-to-Line Motor Voltage, 12.95 hp, 24,189 rpm

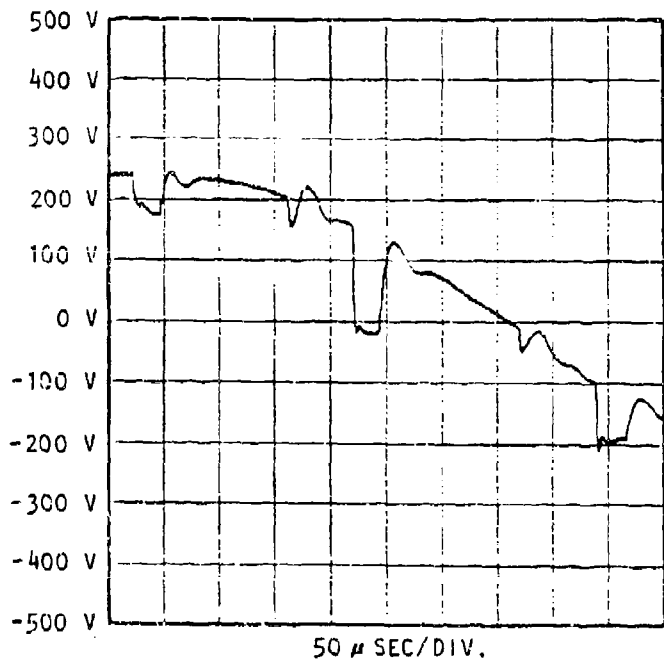


Figure 6-19. Motor Line-to-Line Voltage, 12.95 hp, 24,189 rpm -- Expanded Time Scale

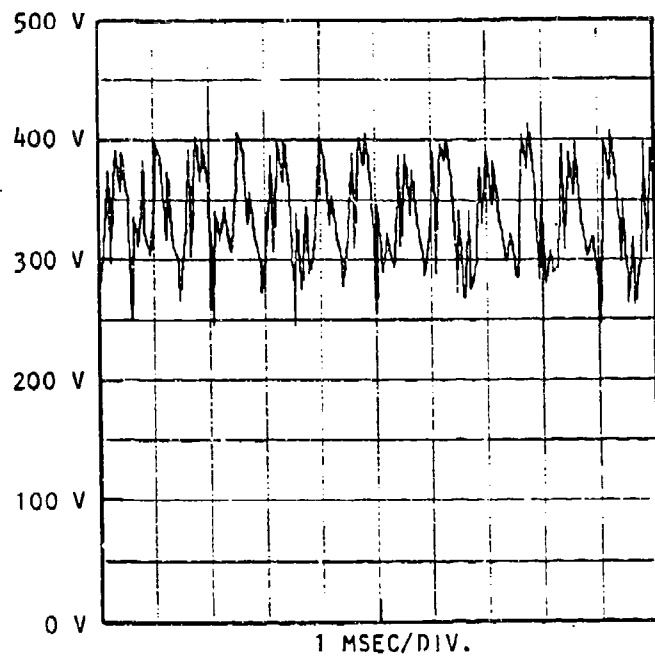


Figure 6-20. Dc Link Voltage, 48.02 hp, 40,740 rpm

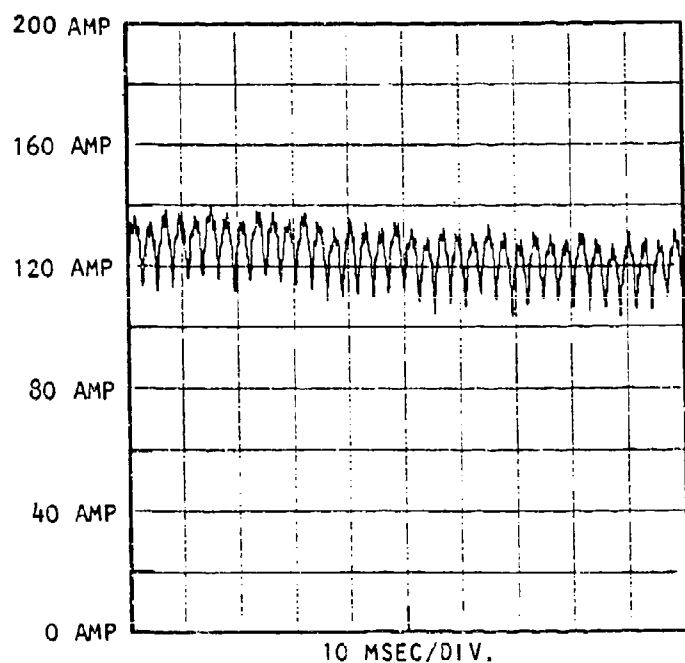


Figure 6-21. Dc Link Current, 48.02 hp, 40,740 rpm

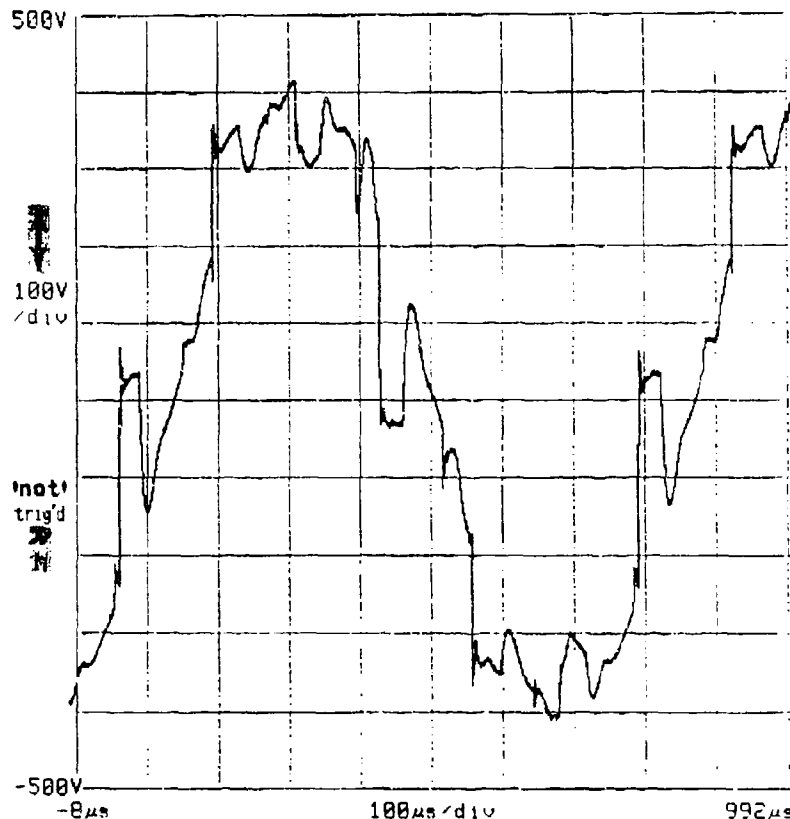
11401 DIGITIZING OSCILLOSCOPE  
date: 9-DEC-87 times: 100000000

(curr1.10,digi1.40,dsy1.10)

Tek

Cursors

DefWfm



ACQUISITION MODE		Acquire	TIME SCALE	
Start	Stop	Desc	100μs/div	2x
Intp(STCS)	Stored	Stopped	Linear	0pts
High Prec	010240 pts			
IMPEDANCE	COUPLING	DISPLACEMENT	SCALING	MOVE
			to	Wfm 1
			H1 Wtms	Intp:5T05
			Status	Zoom

Example of full digitizing oscilloscope printout

Figure 6-22. Line-to-Line Motor Voltage, 48.02 hp, 40,740 rpm

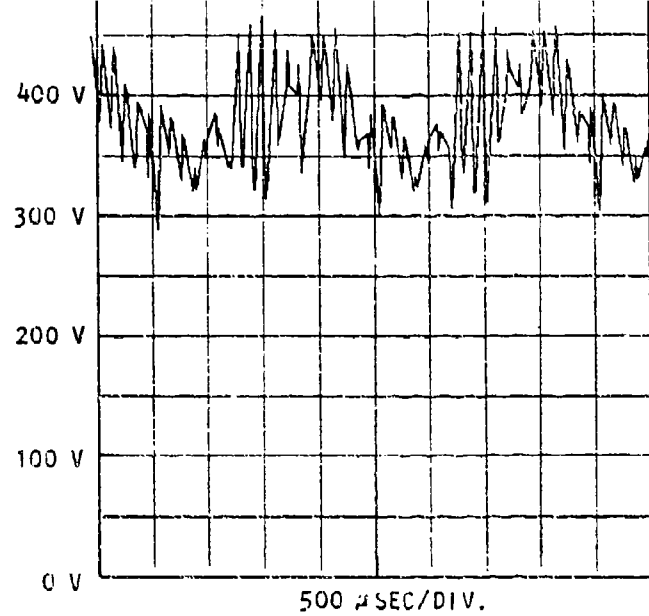


Figure 6-23. Dc Link Voltage, 62.05 hp, 45,168 rpm

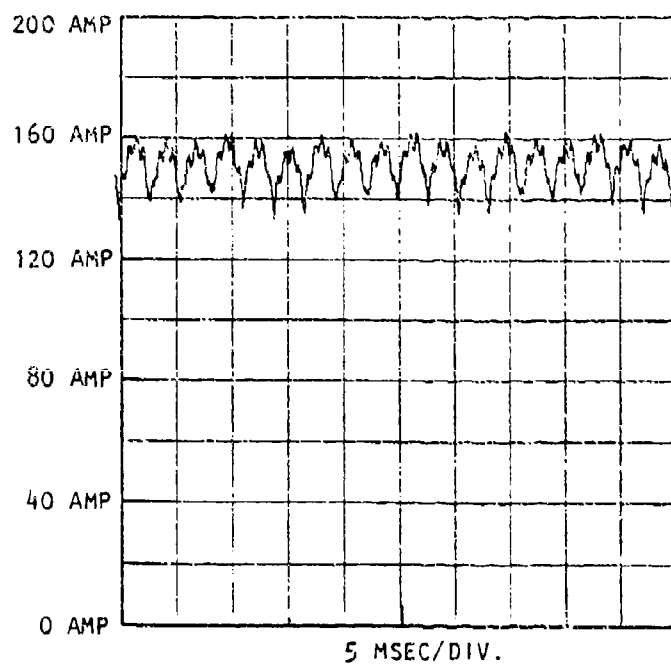


Figure 6-24. Dc Link Current, 62.05 hp, 45,168 rpm

13401 DIGITIZING OSCILLOSCOPE  
data1 TO DLT-3 time 11.111 ms

(exp1.10,dig1.40,dsy1.10)

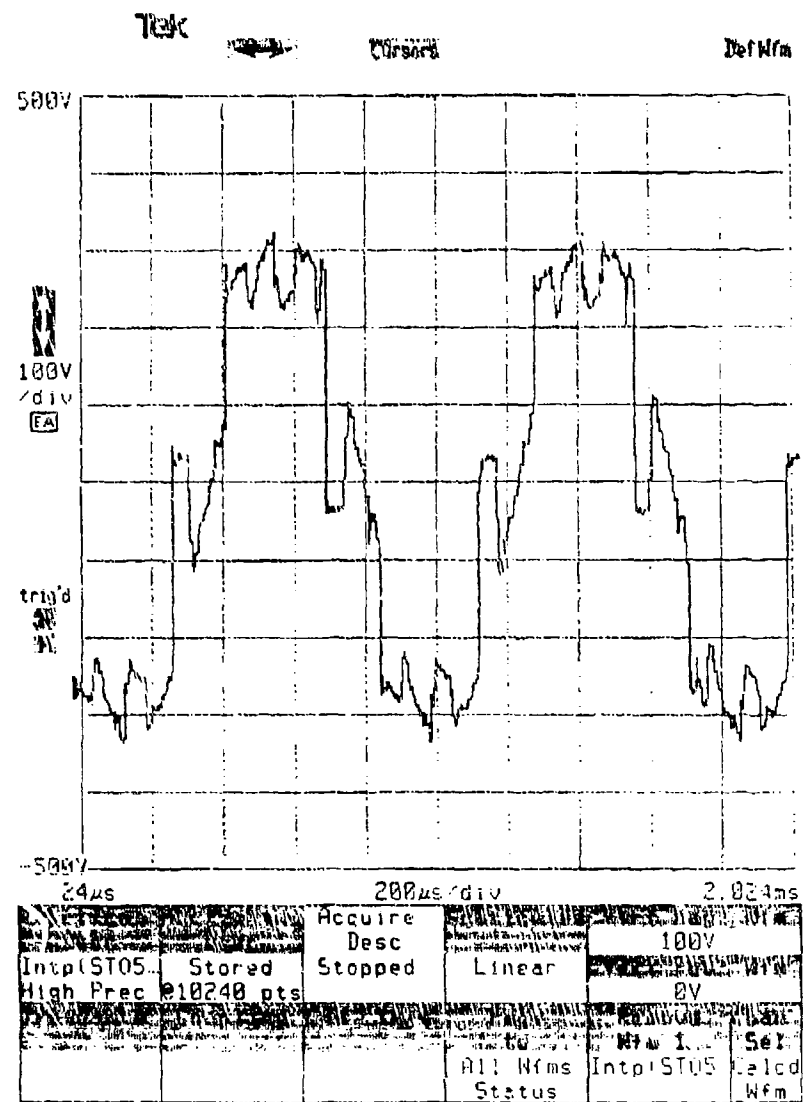


Figure 6-25. Line-to-Line Motor Voltage, 57.06 hp, 35,133 rpm

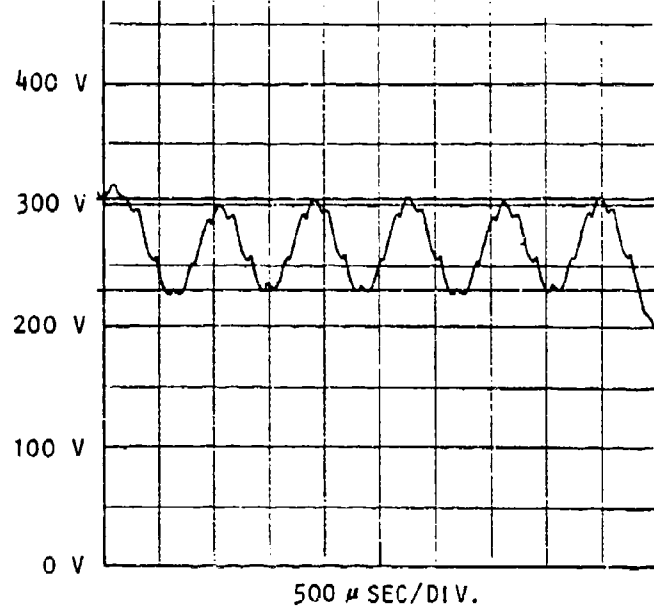


Figure 6-26. Dc Link Voltage, 57.06 hp, 35,133 rpm

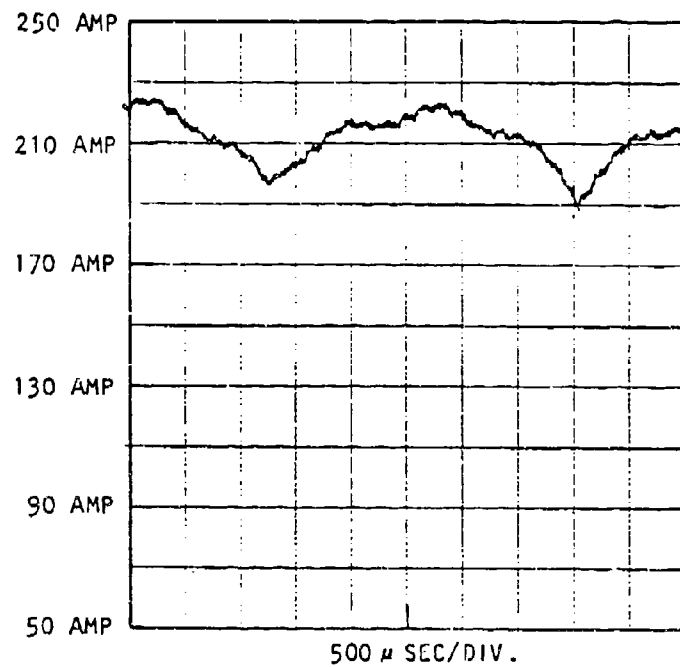


Figure 6-27. Dc Link Current, 57.06 hp, 35,133 rpm

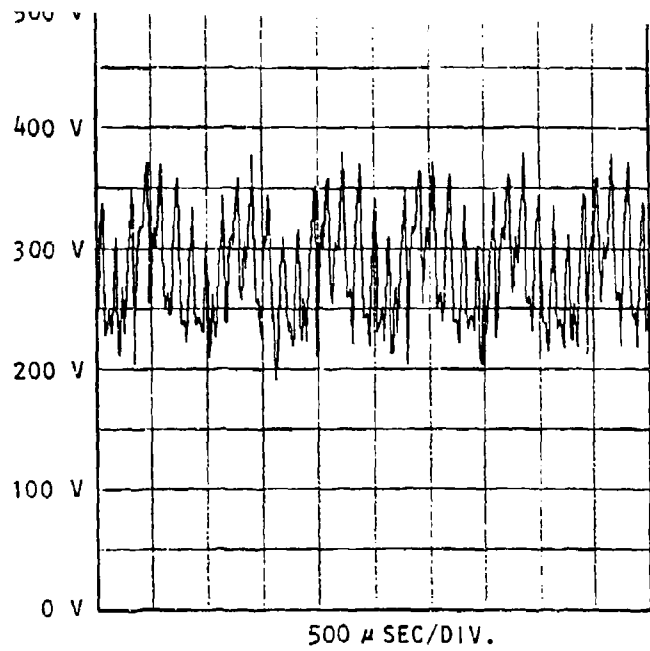


Figure 6-28. Dc Link Voltage, 68.5 hp, 37,080 rpm

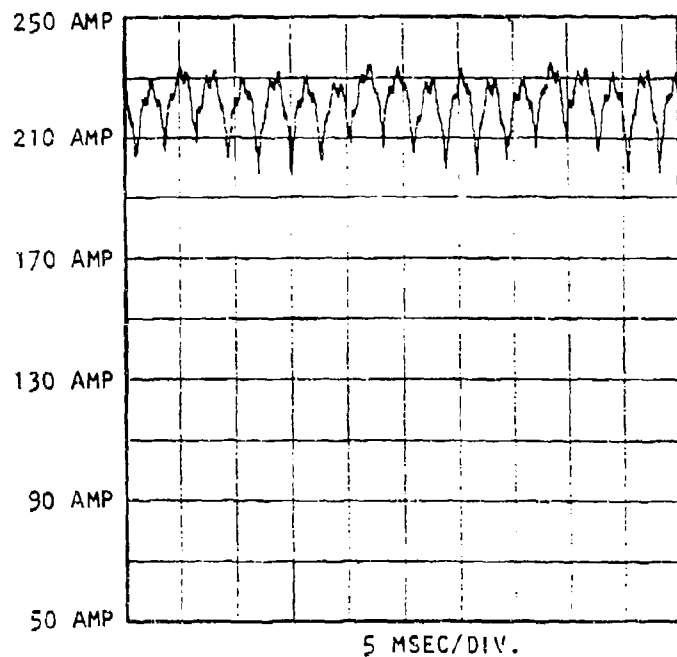
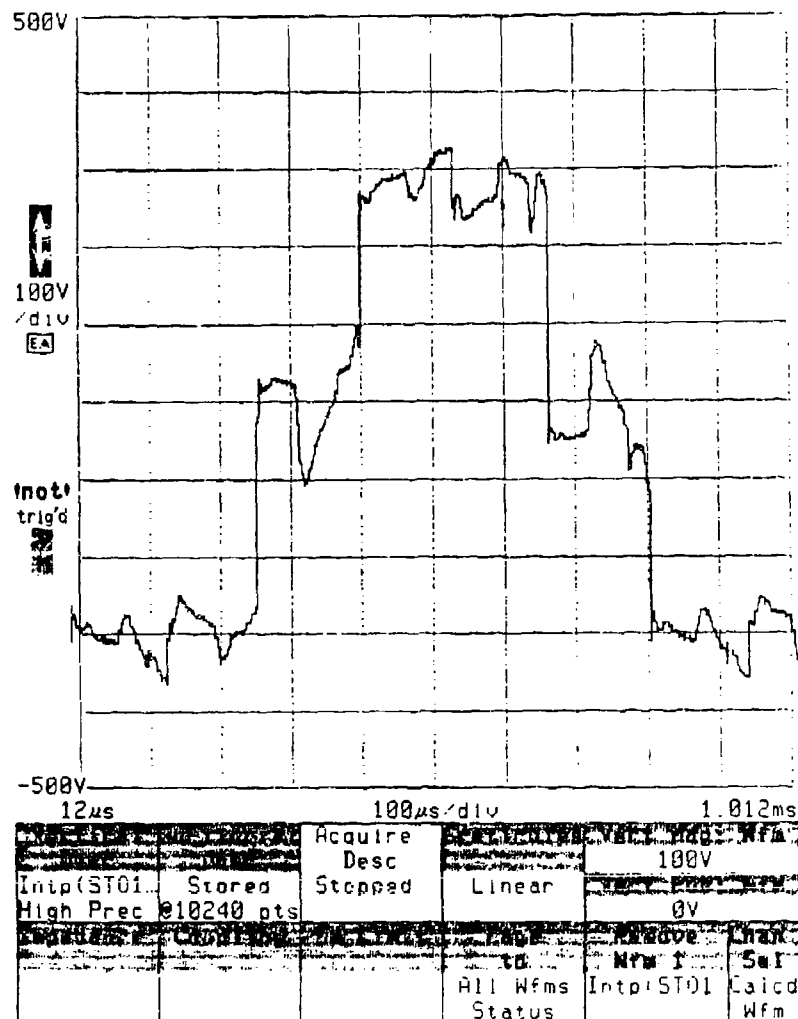


Figure 6-29. Dc Link Current, 68.5 hp, 37,080 rpm

Tek

Cursors

Definitions

Figure 6-30. Line-to-Line Motor Voltage, 68.5 hp, 37,080 rpm

Predicted pump performance on MIL-C-7024 at 45,000 rpm is shown on Figure 6-31. Correcting the high-flow test data to 45,000 rpm (flow  $\propto$  rpm,  $\Delta P \propto$  rpm<sup>2</sup>) and comparing this with the calculated performance shows that at low flow the  $\Delta P$  is about 10 percent higher than predicted, and at high flow the  $\Delta P$  is about 4 percent higher than predicted. The density of MIL-H-83282, the actual test fluid, is 11 percent higher than MIL-C-7024, which was the baseline fluid. Therefore, the actual pressure rise should also be 11 percent higher. At low flow, the agreement between the actual and predicted  $\Delta P$  is within 1 percent. At high flow, the effect of fluid viscosity must also be taken into account. The viscosity has a very small effect at low flow. At 90°F, MIL-H-83282 has a viscosity of 26 centistokes compared to less than 1 centistoke for MIL-C-7024. An empirical correction of 3 percent should be applied to the actual  $\Delta P$  at the high flow condition. At high flow, after allowing for the effect of density and viscosity, the test data is within 4 percent of predicted.

Figure 6-31 also shows the calculated efficiency plotted as a function of flow at 45,000 rpm. This calculated efficiency has to be reduced to allow for the effect of fluid viscosity. An empirical correction indicates that the efficiency should be 90 percent of predicted at high flow and 98 percent of predicted at low flow. Near perfect agreement is seen at the 48-gpm, 45,000-rpm test point. No high-flow test points could be made at 45,000 rpm; however, the calculated efficiency at that speed is compared to the 37,000-rpm high-flow data. The measured efficiency at that condition is less than expected from the calculated performance.

The response of the motor and pump to step commands was determined. The change to the substitute motor controller also required the use of a modified step command circuit. The only significance of this is that the step ramp was somewhat slower, requiring up to 100 msec in transition to the new speed command level. The set point at the low-speed condition was 13,800 rpm instead of the desired 15,000 rpm; so a slight penalty on the system also applied here. The step command to rated power was set to 40,000 rpm because the power at that speed closely approximated the 45-hp load point.

Figure 6-32 shows the time to accelerate from 13,800 rpm to 24,000 rpm, and Figure 6-33 shows the time to decelerate between those same speeds. The latter test is the only condition where the time to stable operation at the new commanded speed exceeded the specification goal. The commanded 13,800 rpm was reached in 1.75 seconds instead of 1.5 seconds. Figures 6-34 and 6-35 give the data on step command transient performance between the 24,000- and 40,000-rpm operating points. Significant margin was demonstrated above the specification limits. The speed change required to reach full power was 16,000 rpm instead of 21,000 rpm, which represented an easier requirement for the system. However, the increase in shaft load was the required 35 hp.

In general, despite the use of the substitute motor controller, the test program provided most of the performance data required of the system. The motor and pump performance were stable throughout the testing, with no appreciable vibration sensed at any of the test conditions. The motor temperatures were stable and the cooling technique verified. During the final phases of system development, the unit operated in excess of 100 hours and demonstrated full-speed operation and a power capability of nearly 70 hp at the motor shaft.

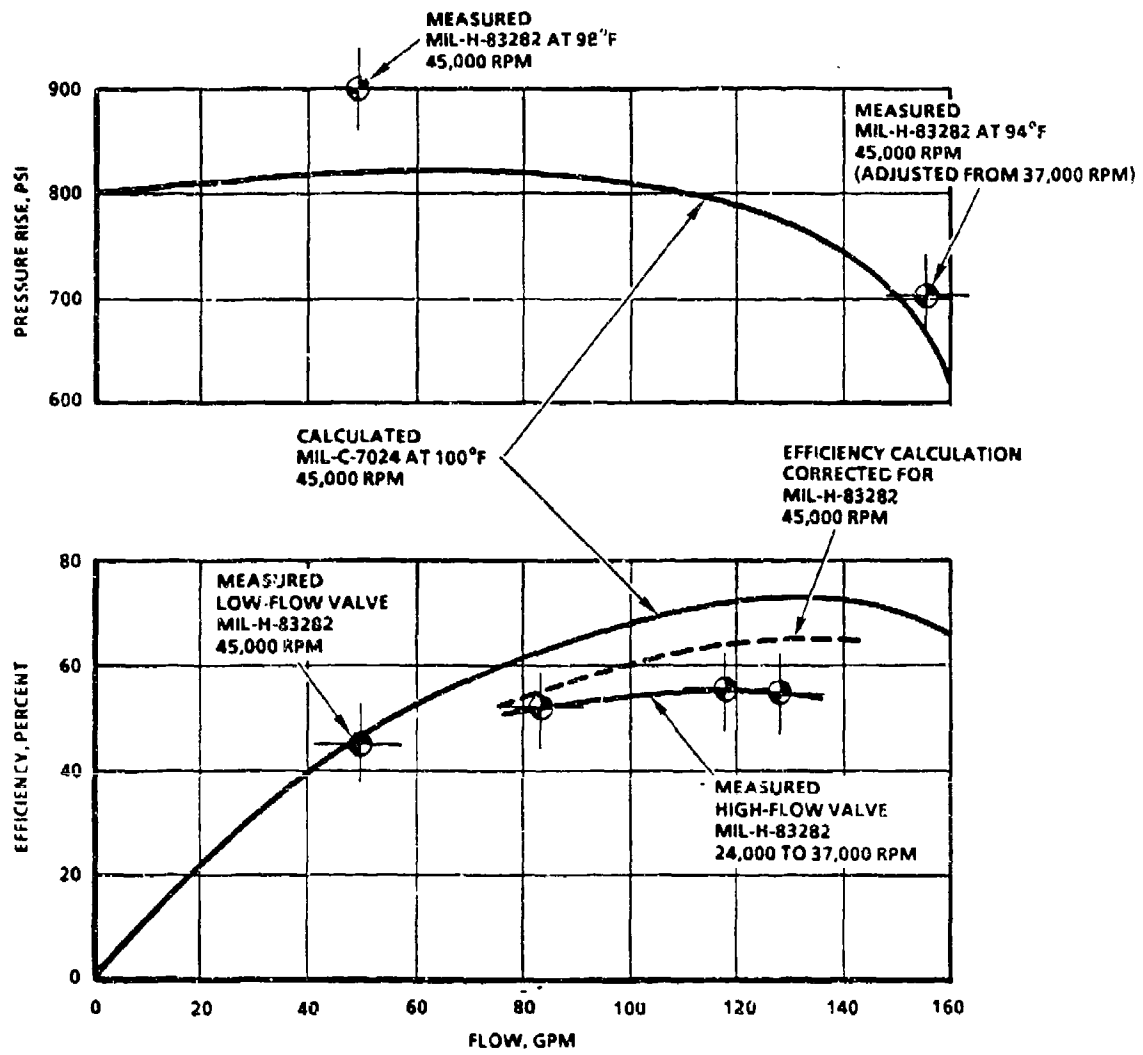


Figure 6-31. Comparison of Calculated and Measured Pump Performance

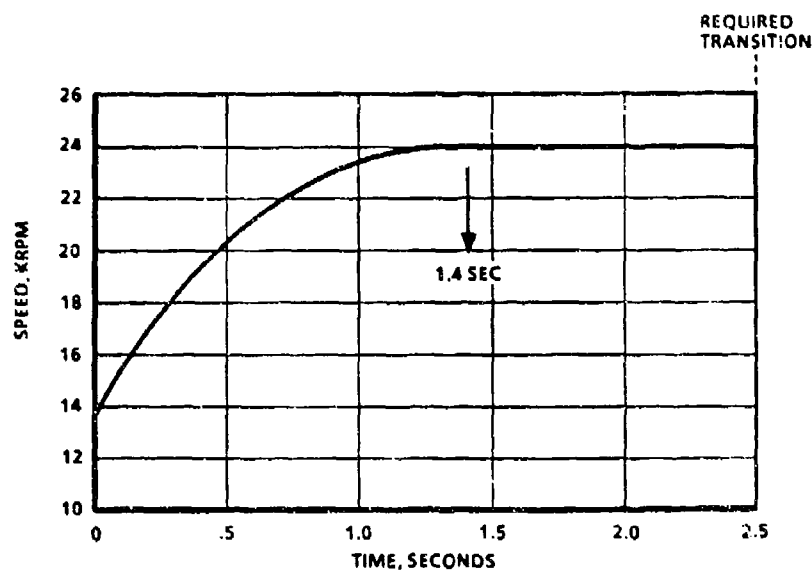


Figure 6-32. Transient Response, 13,800 to 24,000 rpm

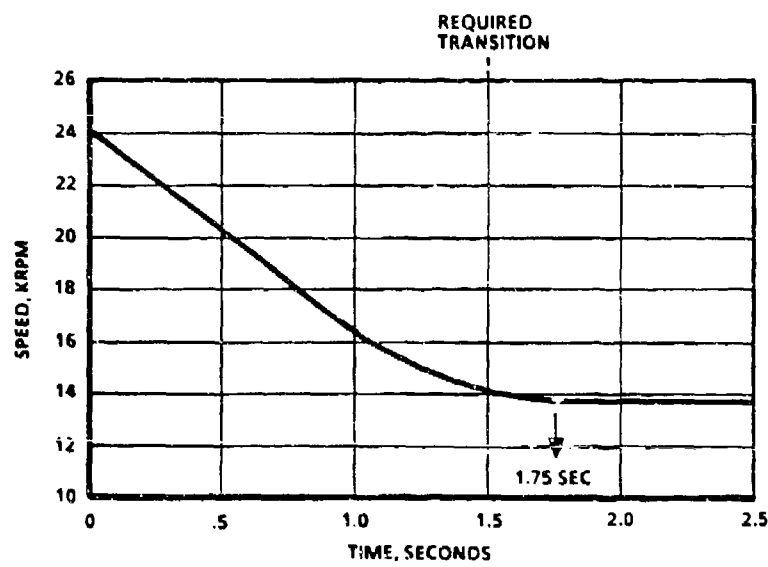


Figure 6-33. Transient Response, 24,000 to 13,800 rpm

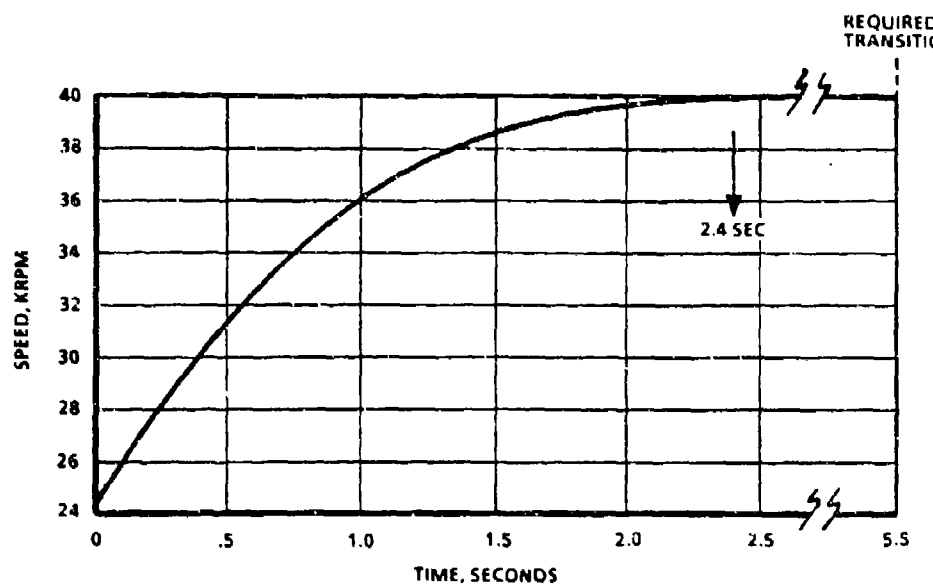


Figure 6-34. Transient Response, 24,000 to 40,000 rpm

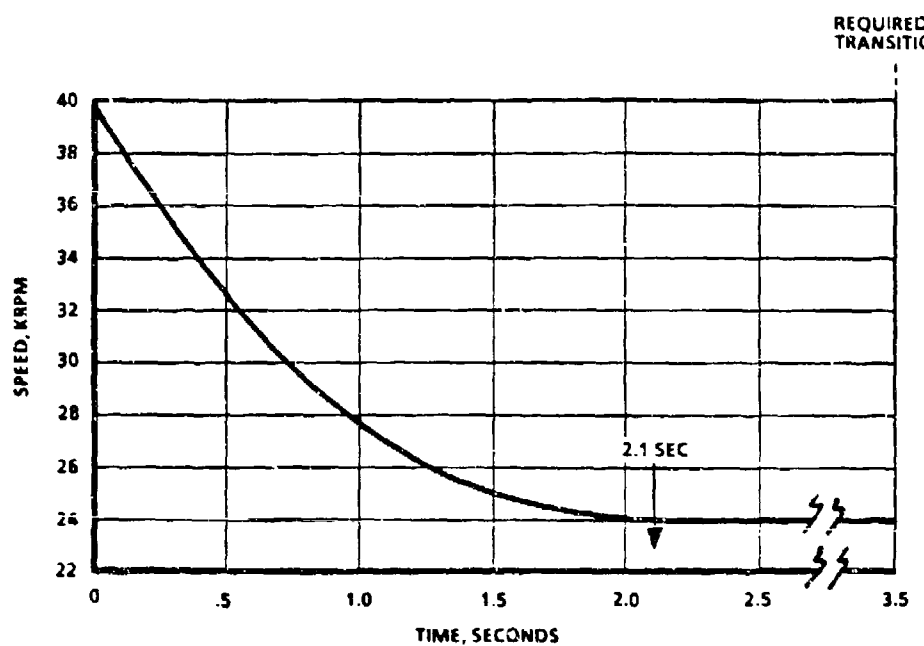


Figure 6-35. Transient Response, 40,000 to 24,000 rpm

## 7. CONCLUSIONS AND RECOMMENDATIONS

### 7.1 SYSTEM

The program demonstrated the capability of stable and precise speed control over a wide load and speed range for an electronically controlled permanent-magnet dc motor. Motor performance over a load range of 1.2 to 68.5 hp and a speed range of 10,000 to 45,000 rpm proves the basic feasibility of this electrical drive system.

The design and development activities did establish that some additional work is required to optimize the system. There are three areas which are of particular significance.

The first area of improvement considered is the motor power output, which was short of the program goal of 85 hp. The limitation was caused by a lack of commutation margin. This problem appears to be easily corrected. During the course of this program, significant increases have been made in the energy level attainable in permanent magnets. This has led AiResearch to develop a newer concept motor which has only 68 percent of the commutating reactance and half the fundamental frequency of the program motor in the same package size. This machine would permit full power output at a slightly higher efficiency.

The second area needing design improvement is the motor bearing lubrication concept. The flooded bearing approach results in significant parasitic losses. This design was satisfactory with the original sleeve-bearing configuration; however, a redesign to a mist-lubricated ball bearing motor is needed to fully optimize the pump output.

Third, the motor controller weight could not be brought down to the specification goal of 50 pounds. Although the development nature of the program required a tightly packaged brassboard controller configuration, with some resultant penalty in size and weight, analysis indicates that a 70-pound controller would be the best achievable even with optimum production packaging. The other factor which had an impact on weight was the need for two input phase-delay rectifiers, one operating with the 400-Hz input and the other working from the 9-phase wild-voltage, wild-frequency input.

Power transistors operating reliably at voltages up to 1000 Vdc and beyond are now available. The design of modern drive electronics must carefully consider the use of these transistors in place of thyristors. This, coupled with an optimized system, including generator and motor, would enable a compact power electronics unit to be built. It is important to realize, however, that imposing one "as-designed" component in such a system may severely impact the total system. All components of such a system must be optimized to ensure that the result is optimized from a weight, size, and performance standpoint.

The utilization of a transistor inverter has a direct benefit for the motor in that the operating power factor can be effectively held close to

unity. This would have provided a torque-per-amp improvement of approximately 15 percent for the motor.

The technology demonstrated in the program, with the design improvements discussed above, would provide for a high-efficiency, high-speed drive capability for a number of possible applications up to the 100-hp range. While a fuel pump concept was used here for demonstration, other pump applications as well as compressor drives could be improved in performance and power density with the application of the technology developed under this program.

## 7.2 MOTOR CONTROLLER

Improvements relating to the motor controller can be grouped into two basic areas: (1) power circuit topology and (2) power semiconductor availability. Both of these areas had an adverse impact on the motor controller design and subsequent bench- and system-level testing. The cause of this impact and recommendations for future designs are discussed herein.

### 7.2.1 Topology

The use of a 3-phase, 400-Hz startup source and a 3-phase, engine-driven generator power source can simplify overall converter design and operation.

Figure 7-1 shows the basic topology and power semiconductors diagram for the existing program motor controller.

The 400-Hz power is rectified, controlled, and used by the inverter to start up and accelerate the PMM, thus providing "fuel" for engine starting. Engine starting provides output voltage from the engine PMG, which is rectified, controlled, and used by the inverter to operate the PMM at the higher speed and power required for increased engine "fuel" demand.

The transfer from 400-Hz to wild-frequency, wild-voltage (WFWV) power needs to be done without causing a large step in rectified voltage to the inverter. To accomplish this and to satisfy the requirement of common neutrals, half-wave 400-Hz and WFWV phase-delay rectification were needed. Figure 7-2 shows the ac and dc voltage potentials in this process.

The adverse impacts were (1) the use of a total of 12 thyristors or phase-delay rectifiers (PDR) and associated circuitry instead of 6 for the 3-phase source and engine generator configuration, and (2) the restriction of two-quadrant operation from 9 half-wave PDR's instead of four-quadrant operation from 6 full-wave PDR's. Two-quadrant operation allows only for active increase in the current, whereas four-quadrant operation allows for active increase and decrease in the current delivered to the PMM inverter. Four-quadrant operation would have provided improved control of the current to the inverter during the initial startup commutation of the inverter thyristors, as well as improved performance during transient or dynamic changes in pump loading.

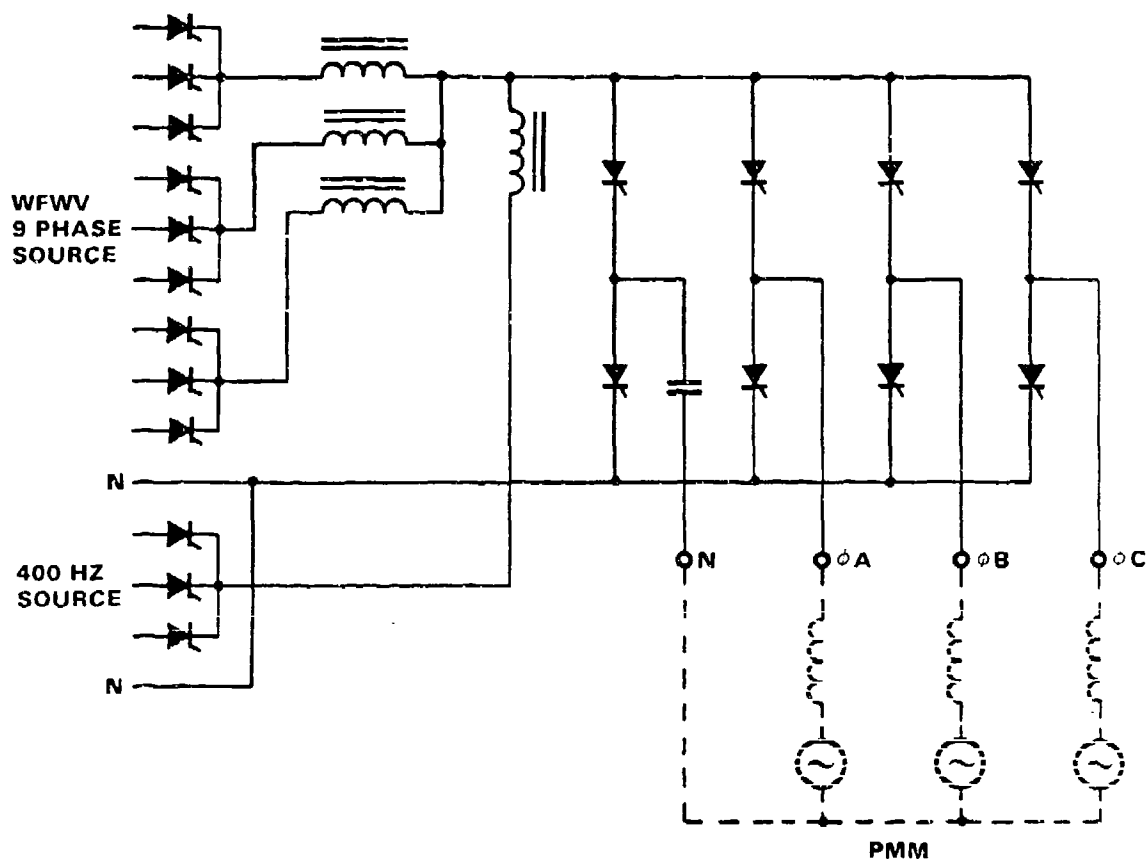


Figure 7-1. Basic Motor Controller Diagram

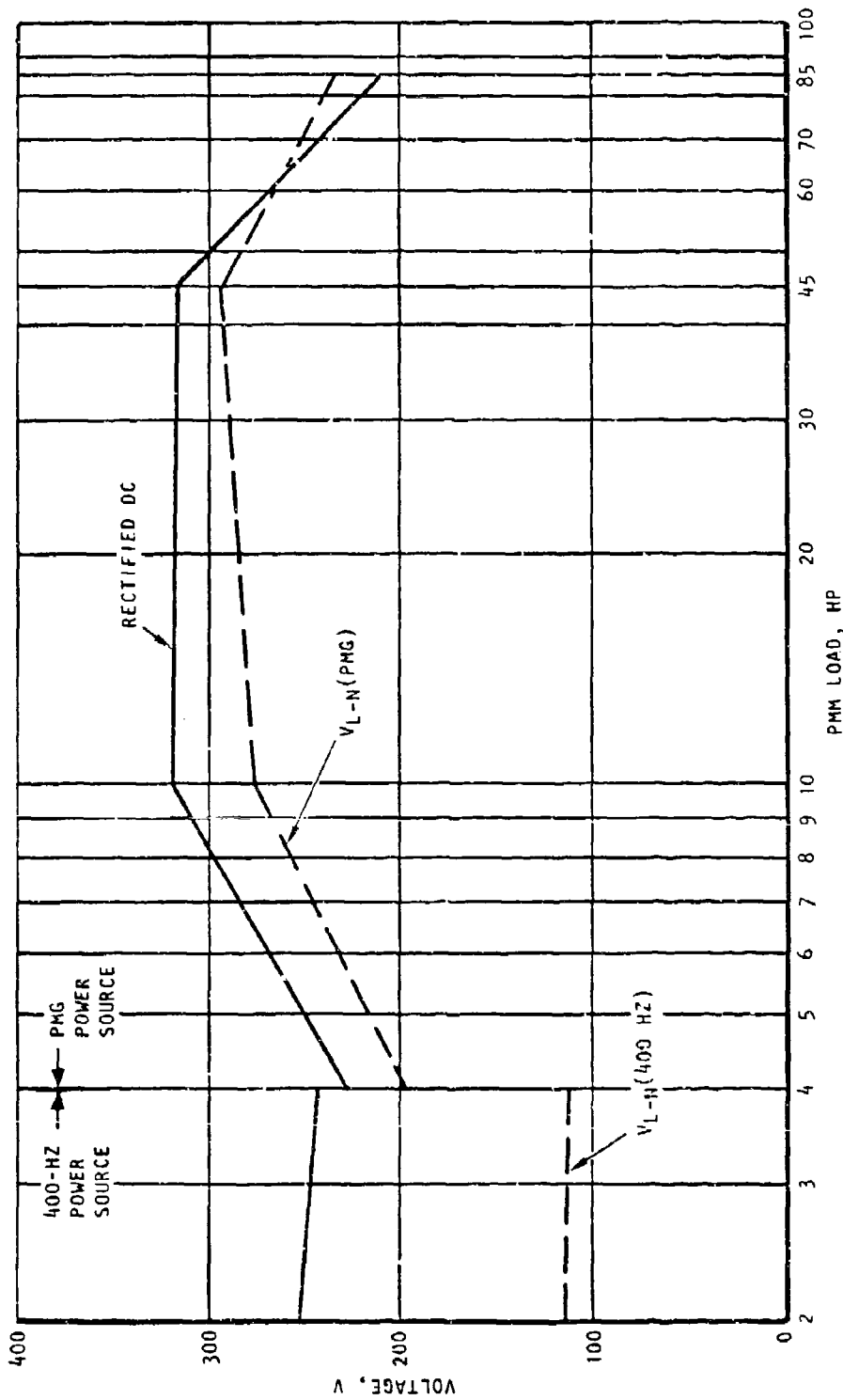


Figure 7-2. Input Voltage Characteristics

### 7.2.2 Power Semiconductors

Currently available power semiconductors include power transistors as well as various gate-turnoff thyristors. Use of these devices would have eliminated the need for auxiliary commutation circuitry associated with the PMM inverter thyristors and allowed for an improved power factor between the inverter and the PMM.

The use of conventional thyristors mandated some form of external commutation, i.e., turnoff method. With a PMM, the method of choice was load commutation, wherein the reactive power of the PMM is used. To accomplish this, the "phase" of the inverter current is advanced compared to the PMM voltage, which enables the PMM voltage to (1) reduce the "conducting" thyristor current to zero ( $\mu^0$ ) and (2) reverse-bias the thyristor for the required turnoff time ( $\gamma^0$ ). Figure 7-3 shows this process which, as noted, causes an overall lower system power factor. This means higher system kVA ratings, which results in a larger controller and PMM size and weight.

### 7.2.3 Improved Source/Controller/PMM System

An improved system configuration is shown in Figure 7-4, wherein two 3-phase sources, gate-turnoff thyristors for synchronous four-quadrant rectification, and power transistors or gate-turnoff thyristors for inversion are used. This would overcome the aforementioned limitations and result in a viable airborne system.

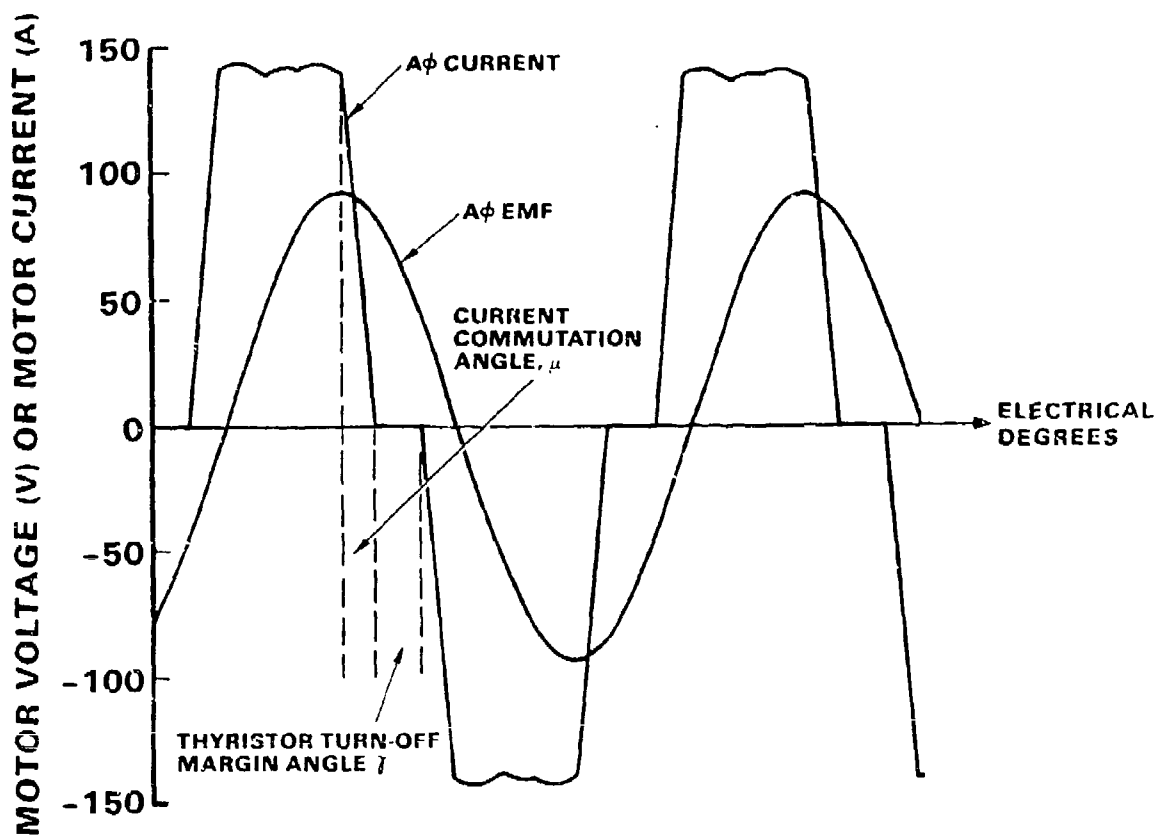


Figure 7-3. Current Source Typical Wave Forms

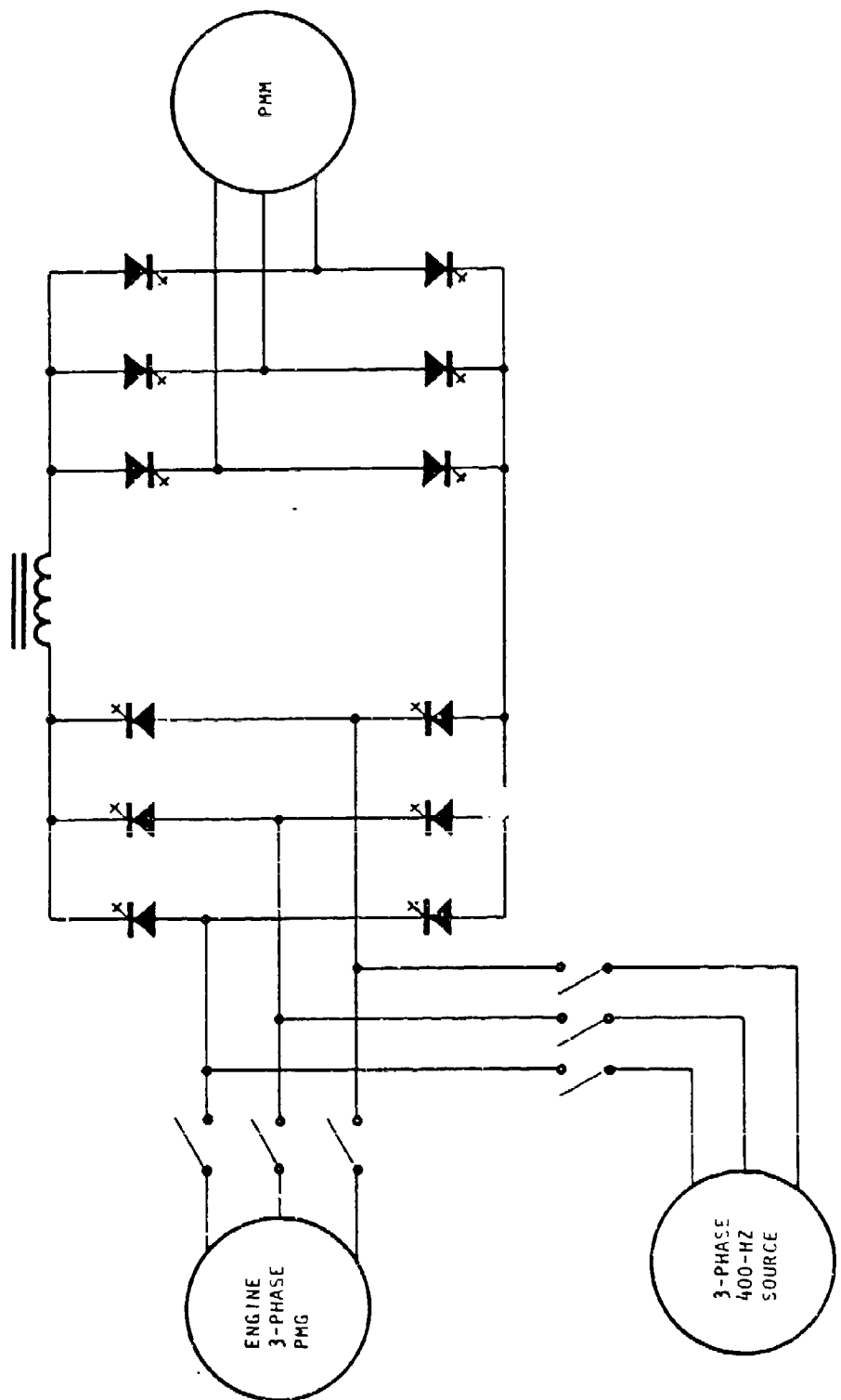


Figure 7-4. Improved Source/Controller/PWM System-Simplified Diagram